

**THE CONSTRUCTION AND IMPLEMENTATION
OF A DEDICATED BEAM LINE FACILITY
FOR ION BEAM BIOIMAGING**

CHEN XIAO

(B. Sc, SHANDONG UNIV)

**A THESIS SUBMITTED
FOR THE DEGREE OF DOCTOR OF
PHILOSOPHY**

**DEPARTMENT OF PHYSICS
NATIONAL UNIVERSITY OF SINGAPORE
(2012)**

Abstract

The past thirty years has witnessed a gradual development of MeV ion focusing systems such that sub 100nm spot sizes can now be achieved. As the resolution of microbeam system using MeV protons and helium ions surpasses that of conventional optical system, microscopy using these particles exhibits unique advantages in imaging.

Observation of the interior structure of cells and sub-cellular organelles at high spatial resolutions are necessary for determining the functioning mechanisms of biological cells. Conventional optical microscopy has limited resolution due to the unavoidable diffraction limits of light, and electron microscopy is only useful when imaging very thin sections due to excessive electron/electron scattering. However, microscopy using MeV ions can play a major role in the imaging of whole cells primarily due to the ability of fast ions to penetrate whole cells while maintaining spatial resolution.

This thesis describes the progress made in building up a dedicated high resolution MeV ion beam microscopy facility and applying different ion imaging techniques to whole biological cells. The new cell imaging facility has now been commissioned, and preliminary resolutions of 25 nm have been achieved for MeV proton and alpha particle beams. The facility has been designed to utilize a variety of techniques, including Scanning Transmission Ion Microscopy (STIM) and Proton Induced Fluorescence (PIF) imaging. The details on the designs and implementations of the new facility are covered in the thesis, followed by pioneering studies using STIM and PIF based on this beam line.

Acknowledgement

Many people helped me a lot in the past four years, which time to time come to mind when I was sitting down and trying to write this thesis.

First and foremost I offer my sincerest gratitude to my supervisor Prof. Frank Watt. Without him, this thesis would never have been possible. He is a passionate scientist and great leader. He has taught me so many things not only in physics but also about attitude, duty, and a lot of high qualities which could guide me all through my life. I am feeling so lucky that I meet him in my younger age. His strong passion, motivation, determination and devotion to research and to whatever he believes in will always remind me in the future. I would also like to offer my sincere gratitude to my supervisor Assistant Prof Andrew Bettoli. He is an expert in optics and offered me lots of advice in my projects. He is always full of amazing ideas, one of which resulted in this project. Besides, his humour and optimistic way of living has made great effect on my value of life.

This project would never achieve so many positive results without the constant support of Assistant Prof Jeroen Van Kan. I take this opportunity to express my strong appreciation to him, especially for his detailed guidance on the beam line construction.

I am also grateful to Dr Chammika Udalagama. He taught me quite a lot of knowledge hidden inside those machines so patiently. He is an expert on software and programming. He is so nice both as a friend and as a senior colleague.

Dr. Ce-Belle Chen, as a cell biologist, gave me great support in sample preparation and in instilling lots of biological terms. Without her help, I could not imagine how I manage these bio-related stuffs.

Dr Ren Minqin also supported me quite a lot. She is quite experienced in tissue study using nuclear microscopy. In addition, she also offered me lots of help in life.

I am also grateful to Associate Prof Thomas Osipowicz and Prof Mark Breese for their valuable discussions and suggestions on the project. I also want to thank to Mr Armin Baysic De Vera, who helped me a lot in hardware problems. Thanks to Mr Choo for teaching me a lot on CIBA accelerator system. Thanks to Dr Isaac Ow Yueh Sheng for assisting me a lot in my beginning of PhD study and sharing with me a lot of valuable ideas on both research and life. Thanks to Dr Hoi Siew Kit for teaching me many basic experimental skills. Thanks to Dr. Yan Yunjun for helping me in quite a lot detailed things, including modules, qualifying exams and thesis writing. Thanks to Reshma, Sook Fun, Susan, Anna for their valuable discussions.

I also want to extend my thanks to all CIBA members who made the whole experience enriching and eventful. Especially to Zhaohong, with whom I had the honor of sharing what I know and had quite often engaged in meaningful discussions from which I learnt a lot myself. Thanks to all the other students in CIBA. CIBA is like a family and I am proud to be a part of it.

Lastly, I would like to thank my parents. They have been always supporting me to their best. Wherever I was, they are always in my heart just as I am in their hearts. Without them, I would not be where I am.

Table of Contents

Abstract	i
Acknowledgement	iii
List of Abbreviations	xii
List of Tables	xiii
List of Figures	xv
Chapter 1 Introduction	1
1.1 Motivation.....	1
1.2 Objective	1
1.3 Outline of the whole thesis	2
Chapter 2 Review of biological imaging techniques	3
2.1 Conventional Optical Microscopy	3
2.2 Super resolution optical microscopy.....	4
2.2.1 Near-field scanning optical microscope (NSOM)	5
2.2.2 Far-field super resolution microscopy	6
2.2.3 Comparison of typical super resolution techniques	11
2.3 Electron microscopy (EM).....	12
2.3.1 Basics of electron microscopy	12
2.3.2 Current status of EM imaging techniques.....	13
2.3.3 Limitations of electron microscopy	17
2.4 X-ray microscopy.....	18

2.4.1 Principle and benefits of X-ray microscopy	18
2.4.2 Current status of X-ray microscopy.....	19
2.4.3 Limitations of X-ray Microscopy	21
2.5 Ion Microscopy	21
2.5.1 Focused Ion Beam Imaging	22
2.5.2 Low Energy Helium Ion Microscopy	23
2.5.3 Nuclear Microscopy-MeV proton and helium ions imaging	25
2.6 Summary	33
Chapter 3 The Design, Implementation and Commissioning of the Cell Imaging Facility	35
3.1 MeV ion Beam Focusing	35
3.1.1 Quadruple Lens.....	35
3.1.2 Basic Theory of Ion Optics	37
3.1.3 Quadruple Probe-forming Systems and Analysis	44
3.2 Design of Cell Imaging Facility.....	54
3.2.1 Justification for a new cell and tissue imaging beam line	54
3.2.2 General design of the new beam line.....	55
3.2.3 End Station Target Chamber Housing	60
3.2.4 Scanning Controller Analysis and Design	62
3.2.5 Scanning clipping analysis.....	66
3.3 Alignment of the Whole Beam Line Facility.....	70
3.3.1 Mechanical alignment during beam line assembly	70

3.3.2 Optical alignment of the microscope	71
3.3.3 Alignment using the beam as an alignment tool.....	73
3.4 Brief description of IONDAQ data acquisition system	75
3.5 Beam Test, Performance Analysis and Discussions	79
3.5.1 Resolution Standard.....	79
3.5.2 Beam spot size analysis	84
3.5.3 Discussions on several challenges and future improvements for improving the beam spot size.	86
3.6 Summary	90
Chapter 4 High Resolution Scanning Transmission Ion Microscopy and its Applications	93
4.1 Basic Principles, Experimental Setup and Analysis of STIM	94
4.1.1 A description of ion beam biological imaging techniques.....	94
4.1.2 Basic Principles of STIM.....	95
4.1.3 Basic principle of FSTIM	96
4.1.4 Pixel Normalization	97
4.1.5 Comparison of proton STIM and helium ions STIM.....	99
4.1.6 Helium Ion Microscope and Helium Ion STIM.....	103
4.2 Three dimensional visualization and quantification of gold nanoparticles in a whole cell	109
4.2.1 Nanoparticles and conventional microscopic techniques for nanoparticles imaging	109

4.2.2 Visualization and quantification of gold nanoparticles (AuNPs) using helium ions	111
4.3 Discussions and future improvements	121
4.3.1 Discussions on Noise Reductions	121
4.3.2 Three Dimensional STIM Tomography.....	123
4.4 Summary	123
Chapter 5 High Resolution Proton Induced Fluorescence and its Applications	
.....	125
5.1 Basic Principles.....	125
5.1.1 Optical fluorescence.....	126
5.1.2 Electron beam induced fluorescence - Cathodoluminescence.....	127
5.1.3 Proton induced fluorescence	128
5.2 Experimental explorations of PIF using in vacuum PMT	131
5.2.1 Experimental Setup	131
5.2.2 Proton fluorescence from fluorosphere.....	133
5.2.3 A Dapi-stained cell study.....	133
5.2.4 Alexa 488 stained cell study	136
5.4 Discussions, Challenges and future studies	138
5.4.1 Challenges in sample preparation	138
5.4.2 Future work on proton fluorescence	140
5.5 Summary	145
Chapter 6 Conclusion.....	147

Bibliography	151
--------------------	-----

Appendices.....	157
-----------------	-----

Appendix A. Sample Preparation for cells internalized with 100nm AuNPs	
--	--

.....	157
-------	-----

Appendix B. Quantification procedures of NPs in a whole cell	159
--	-----

List of Abbreviations

AI	Analog Imaging
APD	Avalanche Photodiode
AuNPs	Gold Nanoparticles
CL	Cathodoluminescence
EM	Electron Microscopy
FIB	Focused Ion Beam
FSTIM	Forward Scattered Transmission Ion Microscopy
GSD	Ground State Depletion
HIM	Helium Ion Microscopy
ISE	Ion induced Secondary Electrons imaging
MeV	Megaelectron Volts
NA	Numerical Aperture
NSOM	Near Field Scanning Optical Microscopy
OM	Optical Microscopy
PALM	Photoactivated Localization Microscopy
PHA	Pulse Height Analysis
PIF	Proton Induced Fluorescence imaging
PIXE	Particle Induced X-ray Emission
PL	Photoluminescence
PMT	Photomultiplier Tube
RBS	Rutherford Backscattering Spectroscopy
RESOLFT	Reversible Saturable Optically Linear Fluorescence Transition
SEM	Scanning Electron Microscopy

SGIM	Scanning Gallium Ion Microscopy
SSIM	Saturated Structured Illumination Microscopy
STORM	Stochastic Optical Reconstruction Microscopy
STED	Stimulated Emission Depletion
STEM	Scanning Transmission Electron Microscopy
STIM	Scanning Transmission Ion Microscopy
STXM	Scanning Transmission X-ray Microscopy
TEM	Transmission Electron Microscopy
TXM	Transmission X-ray Microscopy

List of Tables

Table 2-1 Comparisons of typical super resolution techniques	11
Table 2-2 Comparison of most commonly high resolution microscopic techniques	34
Table 3-1 Main beam optics parameters for the CIBA proton beam writing line. WD is working distance as show in Figure 3.3; Simulations are using PBO based on 2 MeV protons and current CIBA accelerator beam status.	46
Table 3-2 Beam optics parameters for spaced triplet under different WD and S. Simulations are using PBO based on 2 MeV protons and current CIBA accelerator beam status.	48
Table 3-3 Beam optics parameters for spaced quadruplet under different WD and S. Simulations are using PBO based on 2 MeV protons and current CIBA accelerator beam status.	51
Table 3-4 CIBA beam parameters and beam optics parameters required for probe size calculation.....	52
Table 3-5 Scanning voltage calculation for typical beam energy and scan size. Calculation is based on single spaced triplet lenses configuration and beam optics parameter in Table 3-4.	65
Table 3-6 Beam extent and astigmatism coefficients for different scan size based on 2 MeV proton.....	68
Table 3-7 Features supported by IonDAQ. Reproduced from ref [49].....	78

List of Figures

- Figure 2.1 A representation of a typical near field imaging scheme.6
- Figure 2.2 Fluorescence nanoscopy methods: including (A) Confocal microscopy as a comparison standard; (B) 4Pi microscopy; (C) STED; (D) RESOLFT; (E) PALM/STORM. Reproduced from Ref [6].7
- Figure 2.3 Super-resolution imaging techniques. *Top*: Schematic representations of (a) NSOM; (b) STED; (c) SIM; and (d) PALM. *Middle*: Dual color images and comparative $1\text{ }\mu\text{m} \times 1\text{ }\mu\text{m}$ sub-regions, for each of the techniques shown at top; (a) Immunolabeled human T cell receptors; (b) Immunolabeled β -tubulin and syntaxin-I in rat hippocampal neurons; (c) Immunolabeled giant ankyrin and Fas L at the Drosophila neuromuscular junction; and (d) Fusion proteins paxillin and vincullin within adhesion complexes at the periphery of a human fibroblast. All scale bars = $1\text{ }\mu\text{m}$. Reproduced from ref [13].10
- Figure 2.4 3D models showing selected cellular structures from an interphase fission yeast cell, completely reconstructed by ET. (A) Architecture of the microtubule (MT) bundles (light green). The cell contour delineated by the plasma membrane is shown in transparent dark green and the nuclear envelope in pink. The red arrowheads point at splaying MTs. (B) MT splaying was found to be almost invariably associated with the presence of mitochondria (in blue), MT-associated mitochondria were consistently more reticulated and larger than those unattached (scale bar, $1\text{ }\mu\text{m}$). Reproduced from ref [16].15
- Figure 2.5 Schematic figure showing principle of liquid STEM of live eukaryotic cells (A). A cell (orange) is enclosed in a microfluidic chamber between two 50 nm thin silicon nitride membranes supported by silicon microchips, protecting the cell from the vacuum (gray) inside the STEM. Gold nanoparticles (Au-NPs) accumulate in clusters of Au-NP filled vesicles. Continuous flow of buffer (blue) keeps the cell alive until scanning with the electron beam (black) is started. STEM of live cells in a microfluidic chamber, 24 hr after incubation with Au-NPs (B). Reproduced from ref[23].16
- Figure 2.6 Computer-generated sections through the tomographic reconstruction of an early budding yeast. Structures have been assigned different colors, which indicate degree of X-ray absorption. Dense lipid droplets appear white and other cell structures are colored shades of blue, green, and orange with decreasing density. Yeast cell, $5\text{ }\mu\text{m}$ diameter. Reproduced from ref[29].20
- Figure 2.7 Reconstructed data of the yeast shown in Figure 2.3 using different volume analysis algorithms. (A) Opaque surface extraction; (B) transparent surface analysis showing internal vesicles; (C) volume rendered thick-slice section with different colors indicating degree of X-ray absorption; dense lipid droplets are white, less dense vacuoles appear gray, structures of varying densities appear green, orange, and red. Yeast cell, $5\text{ }\mu\text{m}$ diameter. Reproduced from ref[29].21
- Figure 2.8 Comparison of interaction volumes for SHIM (center), SGIM (left), and SEM (right) in a Si sample. The interaction volume of SHIM is sharply

peaked at the incoming point, allowing for a significantly smaller interaction radius than SGIM or SEM. In all three cases, the beam enters at the top of the figure and is simulated with zero width and E=30 KeV. (The SEM result is not to scale because of its significantly larger interaction volume). Reproduced from [36].	24
Figure 2.9 Images of a N2A cell stained with Sytox® Green Nucleic Acid Stain: (a) Confocal microscopy, (b) Proton STIM, (c) Alpha STIM, (d) Proton induced fluorescence. Reproduced from [42].....	27
Figure 2.10 The trajectory of 2 MeV protons (1000) penetration into 5 μm human pancreas. [44]	29
Figure 2.11 Pictorial representation of the radial deposition of energy. The top images correspond to 3000, 1000, and 500 KeV protons while the bottom to 100, 25, and 10 KeV electrons. Reproduced from [45].	31
Figure 2.12 Pictorial representation of the radial deposition of energy for 2 MeV protons (a) and 100 KeV electrons (right) for a 5 μm thick layer of PMMA. Reproduced from [45].....	32
Figure 3.1 A schematic design in a quadruple lens. Also shown are the lines of field inside the lens and the forces acting on a positively charged particles travelling into the plane of the paper at various points in the quadrupole aperture (A to D). A and B lie in the converging plane, while C and D are in the diverging plane.....	36
Figure 3.2 The effect of a single quadrupole lens on a charged particle beam entering from the left of the picture.	37
Figure 3.3 Current CIBA proton beam writing probe-forming lenses configuration. Fig a shows the lenses configuration with a workgin distance (WD) of 0.07 m. Fig b show the x and y beam envelopes in the beam trajectory.	45
Figure 3.4 Spaced triplet configuration (Fig. a) and its beam envelop (Fig. b). S is the space between coupled Q1 and Q2; WD is the working distance.....	47
Figure 3.5 Spaced Quadruplet configuration (Fig. a) and its beam envelope (Fig. b). Q1 is coupled with Q4, while Q2 is coupled with Q3. S is the space between Q2 and Q3. WD is the working distance from Q4 to the image plane.	50
Figure 3.6 A whole view of CIBA ion beam facilities. The left figure shows the previous setup, while the right one includes the newly built two beamlines---next generation proton beam writing facility (in the 20 °position), cell and tissue imaging beam line (in the 30 °position).	55
Figure 3.7 Schematic design of the endstation chamber in the new cell and tissue imaging beam line facility.	57
Figure 3.8 Layout of the cell and tissue imaging facility, showing from right to left: the electrostatic scan module, the 4 OM 52 quadrupole lenses, and the target chamber (with the side mounted XYZ stage and the top mounted microscope).....	58

Figure 3.9 Layout of the inside of the target chamber, showing the XYZ target stage, the detector array (which includes a 5X and 15 X objective), and the mirror which transfers the target image into the top mounted microscope.	59
Figure 3.10 Three dimensional views of designed vacuum chamber. In the figure, (1) beam entrance in the front chamber wall; (2) 3D nano stage support, under which there is pumping port; (3) view port feedthrough on the top plate connecting to optical microscope; (4) 6 inch feedthrough for holding the XYZ manual manipulator on the side wall.	61
Figure 3.11 The vacuum chamber drawings. The top left is a three dimensional view. The middle drawing is front view of the front chamber wall, on the left, right, top and bottom of the front view are left view, right view, top view and bottom view of the chamber, while the back view is on the top. Unit is in mm.	62
Figure 3.12 Scanning plates and the effect caused on the beam going through the plates.	63
Figure 3.13 Figure for beam scanning analysis. M1 to M8 are Markers put in PBO program for beam extent monitor.	67
Figure 3.14 Final beam plots for different scan sizes based on parameters shown in Table 3-4. (a) 20 μm , (b) 80 μm , (c) 120 μm , (d) 160 μm , (e) 200 μm , (f) 240 μm	69
Figure 3.15 Alignment laser for optical mirror alignment. The laser can sit in the eyepiece or the microscope camera port.	72
Figure 3.16 Oxford Microbeams quadrupole lenses. Micrometers for controlling vertical and horizontal alignment are shown in the figure as the top two, the other two are in other side. The bottom micrometer is to control the rotational alignment.	74
Figure 3.17 (a) Schematic showing IonDAQ system. (b) Schematic diagram of the functionality of the CORE component of IonDAQ. Reproduced from ref [49].	76
Figure 3.18 Nickel grid resolution standard. Figure a shows the optical micrograph of the grid; Figure b and figure c is the electron micrograph of the small grid area in figure a.	79
Figure 3.19 Grid image for beam performance test using 1.7 MeV helium ions. Figure a shows SEM image of a grid area; Figure b shows direct on axis STIM image of the same area; Figure c and d show 10 μm direct STIM image of the area selected in the yellow square in figure b. In figure d, edge profile data are extracted from the two rectangular areas for beam spot size analysis in horizontal and vertical directions.	83
Figure 3.20 Shape of the line scan in scanning a Gaussian profile over a sharp edge. The above shape is obtained with signals such as RBS, PIXE and STIM.	85
Figure 3.21 Beam spot fitting results for the experimental data in Figure 3.19 d. Figure a is for horizontal direction, while figure b is for vertical direction. FWHM of fit is 19.5 nm and 25 nm in the two directions.	86

Figure 3.22 6 um image of nickel grid cross. The beam is scanned faster in X direction and going down gradually in Y direction. Red box is the image when the cooling fan is temporarily switched off.	87
Figure 3.23 A simple improved cooling way. The current applied to L1 is the highest. The white pipe extends its blowing exit toward L1 to blow air in.	88
Figure 3.24 1.7 MeV alpha STIM image of grid after improvement on lens cooling.....	88
Figure 4.1 MeV ion beam interactions with biological sample. Each ion induced signal can be detected and developed as an imaging technique labeled in the bracket.....	94
Figure 4.2 Direct Helium ion STIM images of a human fetal liver cell. Image taken with pixel normalization is showed in figure a; while image of the same cell taken without pixel normalization is showed in Figure b. Beam current is fluctuating in 20% around 10 KHz. Beam: 1.2 MeV helium ions. Color map: Jet.....	98
Figure 4.3 Energy loss curve of helium ions and protons penetration into biological material (human pancreas tissue).....	99
Figure 4.4 On axis STIM images of a Hela cell from the same energy (1.5 MeV) protons and helium ions. Figure a is for proton STIM and Figure b is for helium ions STIM. The beam currents are 10 KHz for both of them. The beam spot size is around 50 nm.....	101
Figure 4.5 Paths of fast (eg ~MeV) and slow (eg ~50keV) helium ions through a cell of nominal thickness 1 micron. The ions initially travel in straight lines losing energy via multiple electron collisions. Towards the end of range nuclear collisions, and therefore large angle scattering, becomes predominant.	104
Figure 4.6 Fast helium ions paths ((a) 1 MeV, (b) 1.5 MeV, and (c) 2 MeV) through 1 μm of biological material calculated using the Monte Carlo simulation code DEEP [45].	105
Figure 4.7 (a) Slow helium ion paths through biological material calculated using the simulation package [56]. In this case, the range for 50 KeV helium ions through 1 μm biological material is ~600 nm, which is insufficient to pass through a cell of nominal thickness 1 μm . (b) As a comparison, simulated paths of 50 KeV electrons through 1 μm of biological material is also simulated using [45].....	106
Figure 4.8 (a) HIM secondary electron image of a human liver cell, showing surface features. Helium ion energy = 45 KeV. (b) Helium ion (STIM) transmission energy loss images of the same cell, showing structural features common to the surface as well as structural features from within the cell. Helium ion energy = 1.2 MeV. Filamentary structures within the cell, as well as the nucleus, can be observed. (c) Mass image showing a 3D plot of the mass distribution (in units ag/nm ²): [1 ag = 10^{-18} gm]. Helium ion energy = 1.2 MeV. The arrows in a–b correspond to a surface feature that has high contrast in the surface image but exhibits a low-contrast circular structure in the transmission image, implying a hollow structure. (d–f) Higher-magnification images from the region of the cell containing the nucleus. The	

arrows in <i>e</i> and <i>f</i> correspond to a surface feature that has high contrast in the surface image but has a ring-like structure in the transmission image, once again implying a hollow structure.....	109
Figure 4.9 Schematic diagram of the experimental setup for cell imaging using fast ions.....	114
Figure 4.10 Scanning electron micrographs of a) HeLa cell (control), b) HeLa cell cultured in an environment of Au NPs.....	114
Figure 4.11 Scanning transmission ion microscopy (STIM) images of a) HeLa cell control, b) Hela cell cultured in an environment of Au NPs. 1.6 MeV helium ions.....	115
Figure 4.12 Higher magnification scanning transmission ion microscopy (STIM) images of a) HeLa cell control, b) HeLa cell cultured in an environment of Au N/Ps. 1.6 MeV helium ions.....	115
Figure 4.13 Forward scanning transmission ion microscopy (FSTIM) images of a) HeLa cell control, b) Hela cell cultured in an environment of Au NPs. 1.6 MeV helium ions.....	116
Figure 4.14 RBS energy spectrum from the NP cell showing C and O counts from the cell, Si and N counts from the Silicon Nitride Window, and Au counts from the NPs. 1.6 MeV helium ions.....	117
Figure 4.15 a) FSTIM image of HeLa cell cultured in an environment of Au NPs; b) Total RBS Au image of HeLa cell cultured in an environment of Au NPs; c) Surface RBS Au image of HeLa cell cultured in an environment of Au NPs. d) Subsurface RBS Au image of HeLa cell cultured in an environment of Au NPs	117
Figure 4.16 FSTIM image of the NP cell, using RBS depth information to colour code the depth of the NPs and NP clusters within the cell. 0-150nm represents the surface NPs.....	119
Figure 4.17 Noise Vs external capacitance for a typical ORTEC charge sensitive preamplifier. Reproduced from [77].....	122
Figure 5.1 Fluorescence mechanism based on Jablonski energy diagram. Reproduced from ref [83].	127
Figure 5.2 Schematic diagram of the possible energy transitions occurring from the excitation of a fluorophore by MeV protons. S-singlet states; VR-vibrational relaxations; IC-internal conversion;	130
Figure 5.3 Simulation of δ -rays generated when 1000, 2 MeV protons impinge on 10 μm thick PMMA. Reproduced from ref [43].....	131
Figure 5.4 Schematic setup for R7400P used in a counting mode for proton fluorescence experiment.	132
Figure 5.5 Proton induced fluorescence images of 1 μm fluorospheres. 2 MeV protons at a current of 30 K protons/s.....	133
Figure 5.6 STIM and proton fluorescence images of the same cell stained with DAPI. a) 1.5 MeV direct helium ions STIM; b) 1.5 MeV proton fluorescence.	134

Figure 5.7 a) and d) are optical fluorescence images; b) and e) are proton induced fluorescence images; c) and f) are helium ions STIM images. Cells are from A549 lung carcinoma cell line, stained with endosomal markers, labeled with Alexa 488.	137
Figure 5.8 a) Schematic principle of reflective objective lens; b) Schematic setup for the fluorescence detection using external PMT and reflective objective.	141
Figure 5.9 Possible setup for curve mirror based proton fluorescence detection system.	143

Chapter 1 Introduction

1.1 Motivation

The ability to visualize an intact cell at nanometre resolution is important for biologists to unravel the mysteries of organelle structures, functions and intracellular interactions. For many years, bio-imaging has relied either on optical microscopy or electron microscopy. However, widefield optical microscopy has limited resolution at around 200 nm due to the diffraction of light. Electron microscopy can achieve a higher resolution, but has a limitation on sample thickness of less than 200 nm thick because of the scattering of the electron beam inside the sample. As a result, the high resolution images obtained from electron microscopy are mostly from thin slices of a whole cell, which leads to problems with sample preparation and also difficulties in retaining the initial structure of the cell during the sectioning process.

Similar to electron beams, MeV proton and helium ions have a greatly reduced De Broglie wavelength compared with optical wavelengths and therefore can be focused to a small spot size without diffraction effects. Unlike electron beams however, protons and helium ions can maintain a straight path and hence spatial resolution as they traverse thick samples. This is due to their heavier mass and higher momentum. As a result, it is anticipated that MeV protons and helium ions can potentially replace electrons for microscopy since at present there is no well developed microscopic technique that can investigate the tiny structures buried inside a whole cell.

1.2 Objective

Theoretical analysis and preliminary results have already demonstrated the potential of high resolution microscopy using MeV protons and helium ions.

The main objective of this thesis is describe the design, construction and implementation of a new dedicated beam line facility for high resolution bio-imaging using MeV protons and helium ions. Furthermore, this thesis describes the development of several possible high resolution ion imaging techniques and their potential applications to current biomedical research.

1.3 Outline of the whole thesis

This thesis is divided into five parts. The first part is chapter 1, which briefly describes the motivations and objectives of the whole thesis. Chapter 2 reviews the most commonly used bio-imaging techniques, such as optical microscopy, electron microscopy and X ray microscopy etc, and then describes the history, background and current status of microscopy using protons and helium ions. The third part of the thesis, discusses the details of both the hardware and software of the new dedicated cell imaging system, including the design, construction specifications, alignment procedures, beam focusing performance and some discussion on further optimizations. Chapter 4 and chapter 5, as the fourth part of the thesis, discusses two high resolution ion imaging techniques: Scanning Transmission Ion Microscopy (STIM) and Proton Induced Fluorescence (PIF) together with some examples of their usefulness in structural imaging of whole cells. Finally, the fifth part, chapter 6, concludes the thesis and discusses some future directions based on the results from this thesis.

Chapter 2 Review of biological imaging techniques

This Chapter reviews and compares various cell imaging techniques, including optical microscopy, super resolution optical fluorescence microscopy, electron microscopy, X-ray microscopy and ion microscopy. It gives the advantages and limitations of each technique. Finally, it provides relevant background information on MeV proton and helium ion microscopy that is essential for understanding the experimental results that will be discussed in later chapters.

2.1 Conventional Optical Microscopy

Wide field optical microscopy utilizing either transmitted light, reflected light or fluorescence is the most widely used imaging technique for biological specimens. Fluorescence microscopy in particular has been successfully utilized in all areas of biomedical sciences due to its simplicity in implementation, its high specificity and sensitivity.

Confocal microscopy is an extension of conventional wide field fluorescence microscopy that utilizes a laser for excitation and scanning for imaging. In confocal microscopy, a pinhole is placed before the detector to eliminate out of focus light in specimens that emanate from outside the focal volume. Since confocal microscopy detects signals from a sharp focal volume, it offers several advantages over conventional optical microscopy, including shallow depth of field, elimination of out-of-focus glare, and the ability to collect serial optical sections from thick specimens.

Conventional optical microscopy (including confocal microscopy) does not have the spatial resolution necessary for imaging sub-cellular structure. At very high magnifications, point objects are not seen as focused points but Airy

disks due to the diffraction effect. Since these diffraction patterns ultimately limit the ability to resolve fine details, the resolving power of a microscope is defined as the ability to distinguish between two closely spaced Airy disks. The size of Airy disks is affected by both the wavelength of light (λ), the refractive index of the materials used to manufacture the objective lens and the numerical aperture (NA) of the objective lens. Therefore, there is a finite limit for resolving separate points at a certain wavelength of light, known as diffraction limit. Assuming that optical aberrations in the whole optical set-up are negligible, the resolution d , is given by:

$$d = \frac{0.61\lambda}{NA} \quad (2.1)$$

If air is the external medium, the highest practical NA is 0.95. This can be increased to 1.5 by using immersion oil. Equation 2.1 shows that the resolution is approximately half the wavelength. In practice the lowest value of d obtainable with conventional objective lenses is about 200 nm using a green light source.

2.2 Super resolution optical microscopy

Several techniques have been developed in the past few years for achieving resolutions better than diffraction limit described above. These techniques are named “super-resolution” microscopy techniques. They fall into two broad categories, “true” super-resolution techniques, which capture information contained in evanescent waves, and “functional” super-resolution techniques, which use clever experimental techniques to reconstruct a super-resolution image. True sub-wavelength imaging techniques include those that utilize

Pendry's superlens, near field scanning optical microscopy (NSOM), 4Pi microscopy and structured illumination microscopy technology (SIM). However, the majority of techniques of importance in biological imaging fall into the functional super-resolution technique category. There are two major groups of methods utilized for functional super-resolution microscopy. The first group is deterministic super-resolution, which enhances the resolution by exploiting the fluorophores' nonlinear response to excitation. These methods include Stimulated Emission Depletion (STED), Ground State Depletion (GSD), and Spatially Structured Illumination Microscopy (SSIM). The Second group is stochastical super-resolution. The chemical properties of many molecular light sources give them a complex temporal behavior. This can be used to make several fluorophores that are close to each other emit light at different times, thereby making them resolvable in time. These methods include Super-resolution Optical Fluctuation Imaging (SOFI) and all single-molecule localization methods such as, Photoactivated Localization Microscopy (PALM) or Stochastic Optical Reconstruction Microscopy (STORM) [1]. The next section will discuss in detail several of these super-resolution optical microscopy techniques.

2.2.1 Near-field scanning optical microscope (NSOM)

Near-field imaging can be utilized to break the resolution limit of conventional optical microscopy since diffraction is a far-field effect. NSOM is a near-field imaging technique by exploiting the properties of evanescent waves. A representation of the typical NSOM imaging scheme is presented in Figure 2.1. A small tip is positioned close to the sample surface. When the aperture size of the tip and the tip-sample distance are both much smaller than optical

wavelength, the resolution is limited by tip aperture size instead of diffraction. By controlling the tip size, high resolution beyond optical diffraction limit can be achieved. An image is formed by raster scanning either the tip or the sample. Lateral resolution of 20 nm and vertical resolution of 2-5 nm have been demonstrated [2-5]. A superior advantage of NSOM may rest in its unique instrumental capability of combining Atomic Force Microscopy (AFM). The combination allows a surface inspection with both topographical data set and a variety of corresponding optical data at high resolutions. However, NSOM have several obvious limitations including its practically zero working distance, an extremely small depth of field, only surface imaging, long scan times and very low transmissivity of illumination tip apertures, etc.

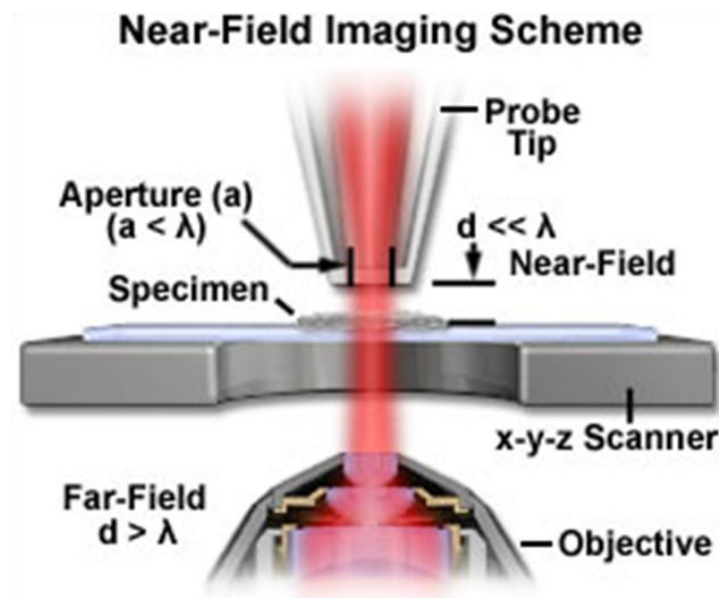


Figure 2.1 A representation of a typical near field imaging scheme.

2.2.2 Far-field super resolution microscopy

Apart from NSOM, there are several far-field techniques that can also break the diffraction limit [6, 7]. A schematic diagram showing the principles behind

these nanoimaging schemes is shown in Figure 2.2. Confocal microscopy is also shown in Figure 2.2a for comparison. For confocal microscopy, the illumination source is a focused 3D diffraction limited spot. By using a pinhole, the detector is able to detect fluorescence predominately from the maximum intensity (shown in green), thus providing a slightly improved resolution over regular fluorescence microscopy. Nevertheless, as discussed previously, the resolution is limited by diffraction to >200 nm in the xy plane and to >450 nm in the axial plane.

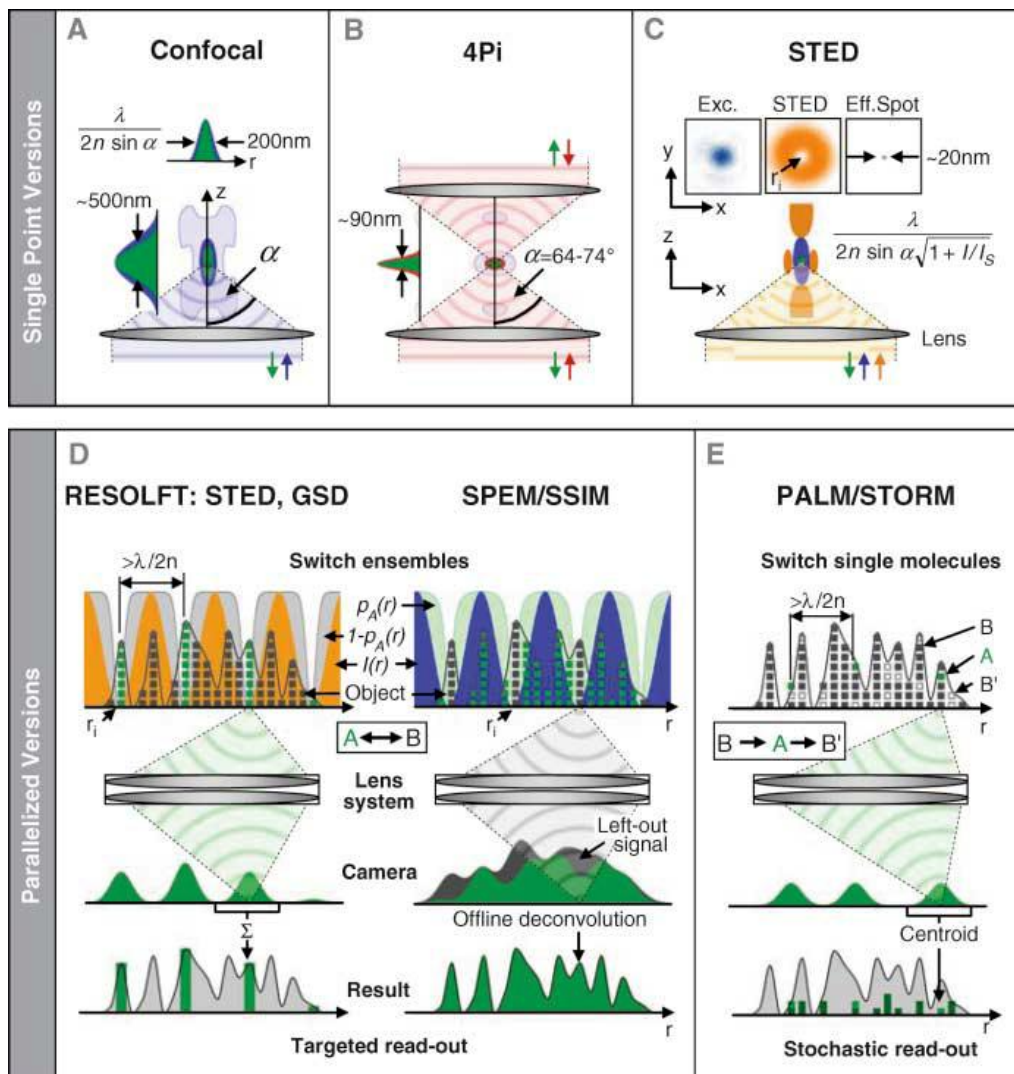


Figure 2.2 Fluorescence nanoscopy methods: including (A) Confocal microscopy as a comparison standard; (B) 4Pi microscopy; (C) STED; (D) RESOLFT; (E) PALM/STORM. Reproduced from Ref [6].

4Pi microscopy

The principle behind 4Pi microscopy is shown in Figure 2.2b. Using two opposing objective lenses that are focused on to the same geometrical volume with the same optical path length, molecules residing in the common focal area of both objectives can be illuminated coherently. The counter propagating spherical wavefronts of the focused excitation light are coherently summed at the focal point and the spherical waverfronts of emitted light can also be summed at the detector. Therefore, 4Pi microscopy produces a narrower spot in the axial direction (z-axis) and hence an improved resolution of 80 to 150 nm.

STED

STED is a new non-diffraction-limited form of scanning far-field fluorescence microscopy. STED utilizes two focused laser pulses (excitation pulse and STED pulse). The excitation pulse is used to excite the fluorophores to their fluorescent state; while the STED pulse is used to narrow down the emission area through the simultaneous de-excitation of fluorophores that are around the focal point. By means of stimulated emission, the de-excitation (STED) beam is capable of confining molecules to the ground state, thus, effectively switching off the fluorophores. In practice, the STED pulse is modified in such a way that it features a zero-intensity spot, which is aligned to coincide with the excitation focal spot. Because no de-excitation occurs at the central zero, the fluorescence emission can occur only in the region close to the zero. Due to the nonlinear dependence of the stimulated emission rate on the intensity of STED pulse, the de-excitation spot size can be controlled by the intensity of

the STED pulse. As a result, the achievable resolution can be reduced to much below the diffraction limit by the intensity of de-excitation STED beam.

SSIM

Wide field techniques like Structured Illumination Microscopy (SIM) and Saturated Structured Illumination Microscopy (SSIM) are also able to break the diffraction limit of light [8, 9]. In SIM, patterned light is used to illuminate the specimen. The resolution is improved by measuring the fringes of the Moiré pattern from the interference of the illumination pattern and the sample. SIM is only able to enhance the resolution by a factor of 2. To further improve the resolution, nonlinearities are needed. SSIM utilizes the nonlinear dependence of the emission rate of fluorophores with intensity of the excitation source [9]. Structured illumination relies on a sinusoidal pattern generated through standing wave interference. By applying the sinusoidal illumination pattern with a peak intensity close to that required in order to saturate the fluorophores to their fluorescent state, one is able to measure moiré fringes that contain high order spatial information that may be reconstructed by computational techniques. Once the information is extracted a super-resolution image is retrieved.

RESOLFT

RESOFT is an acronym for the technique of reversible saturable/switchable optically linear fluorescence transition. In fact, the previously discussed techniques like STED and SSIM are all based on the RESOLFT concept where optical methods to target the coordinates of the sample in order to actively define the areas where the fluorophores must be on or off.

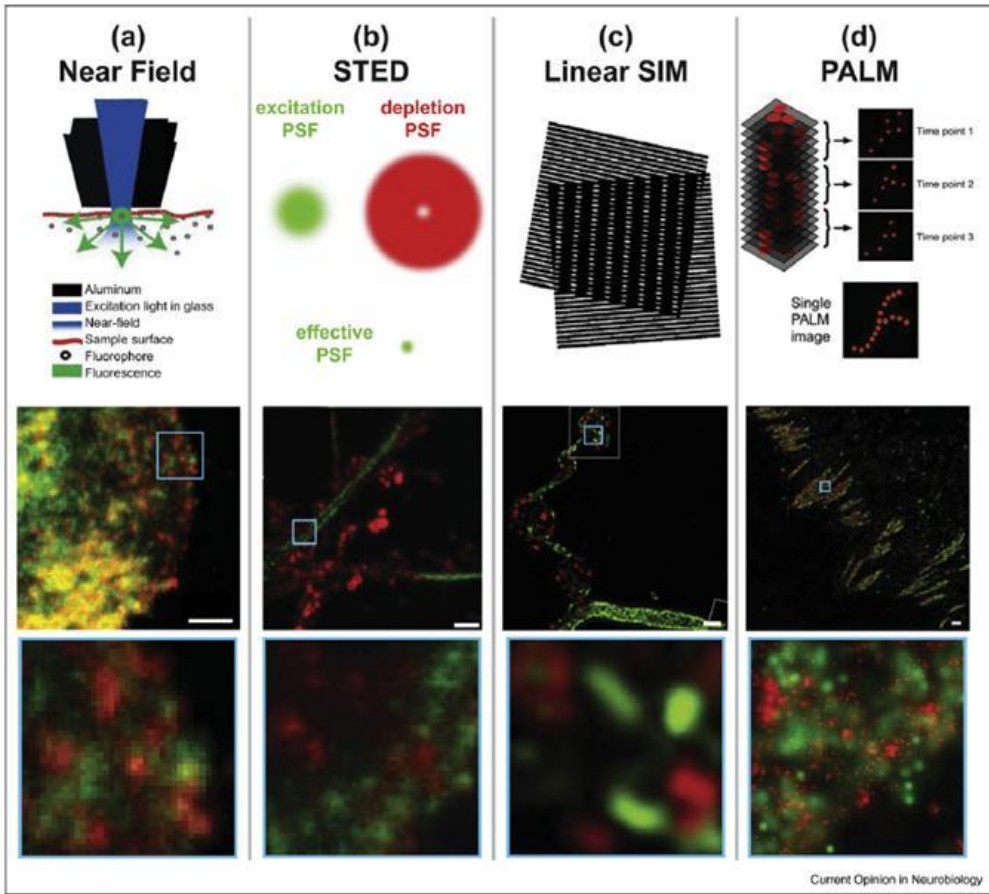


Figure 2.3 Super-resolution imaging techniques. *Top:* Schematic representations of (a) NSOM; (b) STED; (c) SIM; and (d) PALM. *Middle:* Dual color images and comparative 1 $\mu\text{m} \times 1\mu\text{m}$ sub-regions, for each of the techniques shown at top; (a) Immunolabeled human T cell receptors; (b) Immunolabeled β -tubulin and syntaxin-I in rat hippocampal neurons; (c) Immunolabeled giant ankyrin and Fas II at the Drosophila neuromuscular junction; and (d) Fusion proteins paxillin and vinculin within adhesion complexes at the periphery of a human fibroblast. All scale bars =1 μm . Reproduced from ref [13].

STORM or PALM

Instead of the targeted switching of fluorophores based on RESOLFT, individual molecules inside a diffraction limited region can also be switched on at different times so that they can be individually localized and subsequently de-activated. A super resolved image consisting of individual molecule positions can then be formed by calculating the centroid of the diffraction blob produced by each molecule and registering its coordinates. Both STORM and PALM are based on this concept. The two techniques were independently developed by different groups [10-12].

2.2.3 Comparison of typical super resolution techniques

Figure 2.3 compares the four typical techniques: NSOM, STED, SIM and PALM. The top part is a schematic representation of each technique, while the bottom part shows representative cell images from each technique. For certain samples where aberrations and scattering are negligible, all of the listed super-resolution methods have been demonstrated to achieve a resolution well beyond the conventional diffraction limit (~200 nm).

Table 2-1 Comparisons of typical super resolution techniques

Techniques	Positive aspects	Negative aspects	Resolution
NSOM	Versatile contrast, High resolution, topography information, no need for fluorescence	Short working distance, Surface study only, fragile tips, weak signals,	Lateral: 20 nm Axial: 2 to 5 nm
SIM	Unlimited resolution is theoretically possible, Rapid (over large regions), No label restrictions, Low intensities, Relatively inexpensive experimental setup	Assumes continuum labeling, Sample must be motionless, Image reconstruction required.	Lateral: 50 nm Axial: 150 to 300 nm
STED	Adjustable resolution, 3D in whole cells,	long image accumulation times, technically complex, specialized dyes, high intensities, photo-bleaching	Lateral: 50 nm Axial: 150nm
PALM/ STORM	Relatively simple experimental set-up , Measures molecular density, Macromolecular resolution	Photoactivatable labels, Long acquisition times.	Lateral: 20nm Axial: 50 nm

Each sub diffraction limit imaging technique has its own unique advantages and disadvantages, which are shown in Table 2-1. NSOM is a near field technique, which is only applicable to surface imaging so has limited applications. Apart from NSOM, all the other techniques are far field techniques that are mainly based on fluorescence labeling and have stringent requirements on fluorescent dyes. All the previously mentioned super-resolution optical microscopy techniques have successfully broken the optical diffraction limit and produced images at a resolution lower than 50 nm. However, most of them are still under development and have quite stringent requirements that greatly limit their applications. When it comes to high resolution biological imaging, electron microscopy is still the most widely used tool with the highest resolution of better than the 1 nm level [6, 7, 13].

2.3 Electron microscopy (EM)

2.3.1 Basics of electron microscopy

The electron microscope utilizes high energy electron beams instead of light to examine specimens on a very fine scale. Electron microscopes exhibit much better resolution than an optical microscope, because high energy electrons have a much shorter wavelength than visible light (photons). As shown in the Equation 2.2, the wavelength of 100 keV electrons is 0.0037 nm, which is much smaller than the wavelength of visible light (400-700 nm).

$$\lambda = \frac{h}{p} = \frac{h}{mv} \sqrt{1 - \frac{v^2}{c^2}} \quad (2.2)$$

where, λ is the de Broglie wavelength of electrons, h is Planck constant, c is the speed of light in vacuum, m and v are electron mass and velocity respectively.

Current biological electron microscopes can be divided into three categories: transmission electron microscope (TEM), scanning electron microscope (SEM) and scanning transmission electron microscope (STEM).

SEM images a sample by scanning it with a high energy beam of electrons in a raster scan pattern. The electrons interact with the atoms that make up the sample producing signals that contain information about the sample's surface topography, composition, and other properties. Transmission electron microscopy (TEM) is a technique where electrons transmitted through an ultra thin specimen are detected. An image is formed by the interaction of the electrons transmitted through the specimen. The image is magnified and focused onto an imaging device, such as a fluorescent screen, or a sensor such as a CCD camera. STEM is also a type of transmission electron microscopy. In STEM the electron beam is focused and raster scanned across the specimen. Transmitted electrons that are scattered are then detected to form an image.

2.3.2 Current status of EM imaging techniques

Currently, Electron microscopy (EM) is able to produce the highest-resolution images of cells. When combined with molecular detection methods, EM is almost the only technique with sufficient resolution to localize proteins to small membrane sub-domains in the context of the cell. Recent procedural and technical developments have improved the power of EM as a cell-biological tool.

Cryo-Electron Microscopy (CryoEM)

In conventional EM, staining is required most of the time in sample preparation in order to increase contrast. High Z materials are used in staining since they will readily interact with the electron beam and produce high contrast. However, staining not only can introduce artefacts, but also limits the resolution to approximately several nanometers due to the size of staining particles used. An alternative way to prepare sample is cryofixation, which stabilizes the sample by rapid freezing typically in liquid ethane to form vitreous ice. These frozen samples can be viewed directly in the electron microscopy. This method is referred to CryoEM, a technique pioneered by Dubochet and colleagues [14]. CryoEM allows the sample to be observed in its native state without any staining. The sample structures can be kept unchanged and the inner structures of molecules are accessible. However, the thickness of the ice layer should be as small as possible (50-200 nm). The resolution achieved for thin sample is around 0.5 to 2 nm.

Electron Tomography (ET)

Two dimensional EM images are not enough to display the complexity of cellular architecture, especially for large organelles. Conventional 3D models of organelles are constructed from the series of their two dimensional (2D) image of thin slices. However, the z-axis resolution of this approach is limited by the section thickness. Instead, Electron Tomography (ET) can generate 3D images at high resolution in both directions through advanced three dimensional reconstruction techniques. By rotating the sample around the center of the target at incremental degrees, two dimensional TEM images at each position can be collected. With constant incremental angle, then 3D model of the sample can be reconstructed from these 2D image projections.

Although TEM has already achieved angstrom resolution, current resolution of ET is still limited at 1 to 10 nm due to several practical factors. The probability of multiple scattering and inelastic scattering arises as the specimen thickness increases, thereby reducing the resolution and image quality [15, 16]. Energy filter can be used to remove the inelastically scattered electron. But the image may become noisy in this case since the remaining fraction of electrons may be quite small. High resolution 3D images can only be achieved for thin samples, but 3D images of thick sample can be regenerated by applying ET to series sections. An example is the study of the microtubule cytoskeleton in fission yeast [16, 17]. To fully track the microtubules, reconstruction image of large cellular volumes is needed. Meanwhile, high resolution was crucial to reveal the details of certain structures, such as the architecture of the microtubule ends.

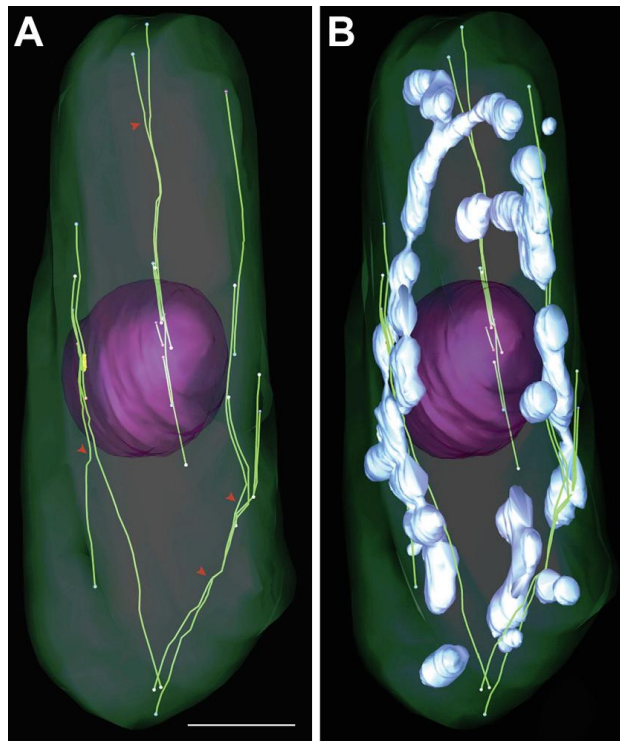


Figure 2.4 3D models showing selected cellular structures from an interphase fission yeast cell, completely reconstructed by ET. (A) Architecture of the microtubule (MT) bundles (light green). The cell contour delineated by the plasma membrane is shown in transparent dark green and the nuclear envelope in pink. The red arrowheads point at splaying MTs. (B) MT splaying was found to be almost

invariably associated with the presence of mitochondria (in blue), MT-associated mitochondria were consistently more reticulated and larger than those unattached (scale bar, 1 μ m). Reproduced from ref [16].

Cryo-ET

Cryo-electron tomography (Cryo-ET) is the combination of the above-mentioned two techniques. Cryofixation helps to preserve the molecules, complexes, and supramolecular assemblies in their native state without any staining and chemical fixation artifacts. ET provides a detailed view of the internal structures of these structures. As mentioned above, ET has the best resolution when the sample is thin (<200nm). Therefore, Cryo-ET is quite suitable for imaging the intact macromolecular components [18], small organelle-like structures such as carboxysomes[19, 20], small isolated organelles and cellular structures such as mitochondria [21, 22] and mitochondrial fragments[22]).

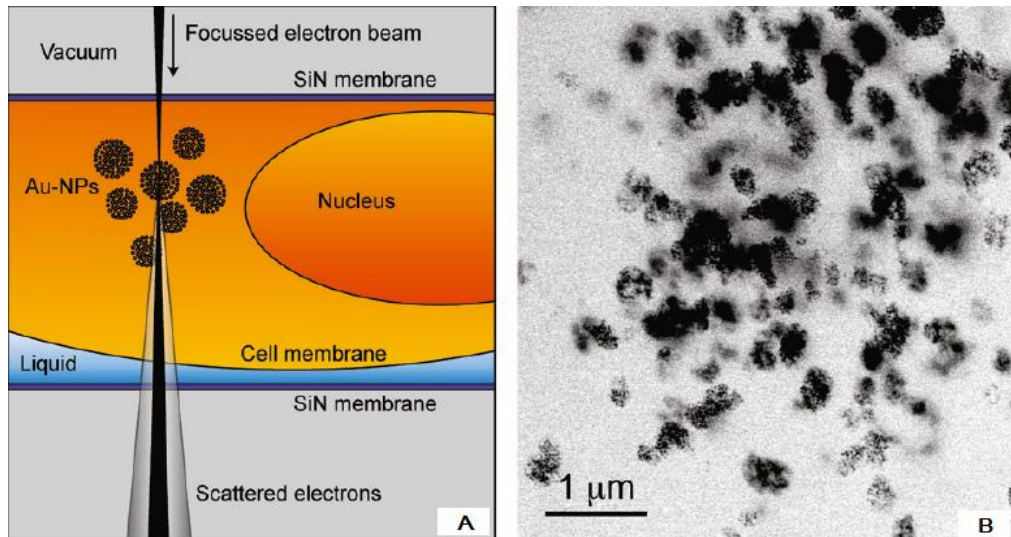


Figure 2.5 Schematic figure showing principle of liquid STEM of live eukaryotic cells (A). A cell (orange) is enclosed in a microfluidic chamber between two 50 nm thin silicon nitride membranes supported by silicon microchips, protecting the cell from the vacuum (gray) inside the STEM. Gold nanoparticles (Au-NPs) accumulate in clusters of Au-NP filled vesicles. Continuous flow of buffer (blue) keeps the cell alive until scanning with the electron beam (black) is started. STEM of live cells in a microfluidic chamber, 24 hr after incubation with Au-NPs (B). Reproduced from ref[23].

STEM

As discussed above, Scanning Transmission Electron Microscopy (STEM) is different from Conventional TEM by utilizing a focused electron beam to scan the sample. It is a direct technique reportedly for imaging whole cells by electron beam which offers nanometre spatial resolution and a high imaging speed. The principles and experimental implementations have been reported in several papers [24, 25]. Figure 2.5 shows one example, where STEM is used to visualize gold nanoparticles uptake in live cells [23]. A cell (orange) is enclosed in a microfluidic chamber between two 50 nm thin silicon nitride membranes supported by silicon microchips, protecting the cell from the vacuum (gray) inside the STEM. The annular dark field detector in the STEM is sensitive to scattered electrons, which are generated in proportion to the atomic number (Z) of the atoms in the specimen, so-called Z contrast, where the contrast varies with Z^2 . It is thus possible to image specific high Z atoms, such as gold, inside a relatively thick (several micrometer) layer of low Z materials, such as water, protein. Figure 2.5b shows the images of intracellular Au-NP aggregations in two different cells, illustrating that Au-NPs had concentrated in three dimensional clusters of vesicles densely filled with Au-NPs.

2.3.3 Limitations of electron microscopy

Firstly, Electron microscopy has the highest resolution at present; however, the high resolution is only applicable to surface imaging (SEM) or ultrathin slices of material (TEM). As the sample thickness increases so does the probability of multiple scattering and inelastic scattering, which reduces the image quality. Inelastically scattered electrons can be removed by an energy

filter but, eventually, the remaining fraction of electrons is so small that the images become too noisy. The advent of electron energy-filtering as a practical tool extended the usable thickness for specimens being studied by electron microscopy up to thicknesses of several hundred nanometers, which however is still not enough for most cells. It is still impossible for TEM to directly image most of the whole cell at a high resolution. Biological specimens have to be prepared in various ways to stabilize them, reduce their thickness (ultrathin sectioning) and increase their electron optical contrast (staining). These processes are complicated and may result in artifacts. Many materials require extensive sample preparation to produce a sample thin enough to be electron transparent, which makes TEM analysis a relatively time consuming process with a low throughput of samples. Secondly, liquid STEM has been reported to be able to image whole cell directly. However, due to the small depth of focus, STEM can only have high resolution in one particular plane; while outside of this plane, the beam resolution is seriously reduced.

2.4 X-ray microscopy

2.4.1 Principle and benefits of X-ray microscopy

Instead of an electron beam or visible light, X-rays can also be used for microscopy. The wavelength of soft X-rays can be as small as 2 nm, which is well below optical diffraction limit. X-ray microscopy is inferior to electron microscopy in spatial resolution. However, it is superior to EM in several ways: (1) If the observations are performed between 2.4 nm (absorption edge of oxygen) and 4.5 nm (absorption edge of carbon), absorption coefficients are greatly different between biomolecules and water (so called “water window”).

Thus, biological specimens can be seen in a wet state. (2) Compared to electron beams, absorption coefficients of soft X-ray shows sharper dependency on atomic number, which implies that images with higher contrast can be achieved even without staining. (3) Absorptivity of soft X-ray is most suitable for the specimen of several microns thickness. Thus it is superior for imaging un-sectioned cells, as the typical thickness of the cells is about several micrometers. With X-ray microscopy, insides of the specimens can be monitored, whereas with electron microscopy, usually only surface or ultrathin slices can be observed, and with optical microscopy, insides can be monitored only in limited cases, because of its transparency or large reflection at the surface. In combining these three characteristics, soft X-ray is much more suitable for unstained, wet cells of several micrometer in thicknesses [26].

2.4.2 Current status of X-ray microscopy

The instruments of cellular X-ray imaging fall into two clear categories: microscopes that require optics such as zone plates and microscopes that do not require any focusing optical elements. In terms of the former, there are two main types of zone plate based microscopes: full field transmission X-ray microscopes (TXMs) and scanning transmission X-ray microscopes (STXMs). Microscopes that don't require focusing optics are classified as lensless projection imaging microscopes (PIMs) or X-ray diffraction imaging microscopes (XDMs)[27]. The best developed two types among all these are transmission X-ray microscopes and X-ray diffraction imaging microscopes, both of which have been reported to image cells in a resolution around 60 nm [28-30].

Center for X-ray Optics, Berkeley National Laboratory, California, examined the yeast, *Saccharomyces cerevisiae*, using X-rays demonstrating unique views of the internal structural organization of these cells at 60 nm resolution. Figure 2.6 shows computer-generated sections through the tomographic reconstruction of an early budding yeast. The images were collected using a transmission X-ray microscope. For tomography, 45 images were collected at 4° through 180° of rotation. The projection series was then aligned to a common axis of rotation and a three dimensional volume reconstruction was performed using weighted, filtered back projection. Figure 2.7 shows the reconstructed data of the yeast cell using different volume analysis algorithms.

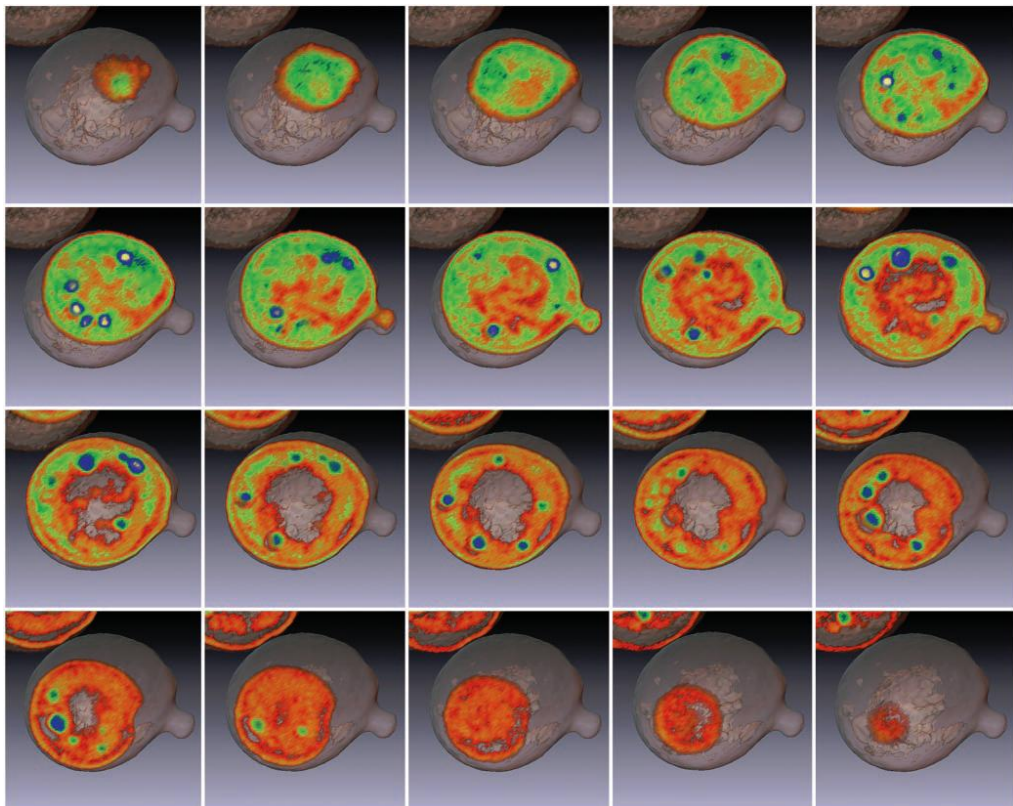


Figure 2.6 Computer-generated sections through the tomographic reconstruction of an early budding yeast. Structures have been assigned different colors, which indicate degree of X-ray absorption. Dense lipid droplets appear white and other cell structures are colored shades of blue, green, and orange with decreasing density. Yeast cell, 5 μm diameter. Reproduced from ref[29].

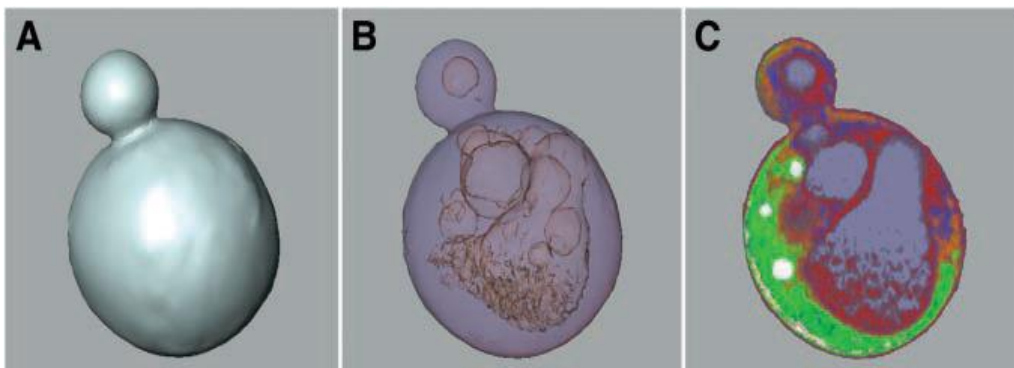


Figure 2.7 Reconstructed data of the yeast shown in Figure 2.3 using different volume analysis algorithms. (A) Opaque surface extraction; (B) transparent surface analysis showing internal vesicles; (C) volume rendered thick-slice section with different colors indicating degree of X-ray absorption; dense lipid droplets are white, less dense vacuoles appear gray, structures of varying densities appear green, orange, and red. Yeast cell, 5 μm diameter. Reproduced from ref[29].

2.4.3 Limitations of X-ray Microscopy

Transmission X-ray microscopes or projection imaging microscopes, in principle, can use laboratory sources, such as laser plasma sources. However, for the best results from all of these X-ray imaging techniques, synchrotron X-ray sources must be used. The use of synchrotron facilities greatly limits the use of X-ray microcopies to be only a few labs. Secondly, for standard transmission X-ray imaging, the contrast is produced by the differences of X-ray attenuation, which is not high enough to obtain a good quality image for many low absorption structures without the help of contrast agents. Experiments have showed that better density contrast can be achieved by using a proton beam compared to X-ray [31].

2.5 Ion Microscopy

If the reason electron microscopes work so effectively is because of the electrons' small wavelength, then why not use a proton (or other ions) microscope instead? As electron microscopes have shown several critical limitations, we want to propose this question. Current ion microscopes can be

divided into microcopies using light ions (proton and helium ions) and low energy heavy ions (like Gallium ions).

2.5.1 Focused Ion Beam Imaging

Systems that use low energy heavy ions like Gallium are called Focused Ion Beam (FIB) systems. These systems have been commercially available for many years. Similar to SEMs, FIB systems use a finely focused beam of ions that can be operated at low beam currents for imaging or high beam currents for site specific sputtering or milling. At low primary beam currents, very little material is sputtered and modern FIB systems can easily achieve 5 nm imaging resolution (imaging resolution with Ga ions is limited to 5 nm by sputtering and detector efficiency). At higher primary currents, many types of materials can be removed by sputtering, allowing precision milling of the specimen down to a sub micrometer or even nanometric dimensions.

FIB imaging at a low beam current offers a comparable spatial resolution with the more familiar and widely used SEM. More importantly, the FIB's two imaging modes, using secondary electrons and secondary ions, both produced by the primary ion beam, offer many advantages over SEM. For instance, FIB secondary electron imaging has no backscattered electrons which in an SEM will cause interference, and FIB secondary ion images can reveal chemical differences, which are useful in many applications. However, since the heavy ions are much larger and nuclear stopping dominates the interaction process, the penetration depth of heavy ions is much lower than that of electrons with the same energy; therefore FIB imaging is only used for the surface. Furthermore, heavy ions will implant into the material after imaging, which will cause serious damage to the sample [32, 33].

FIB-SEM is a recently developed three dimensional imaging technique, which integrates FIB and SEM together in one microscope. FIB is used to mill the sample slice by slice precisely, and SEM is subsequently employed to image the surface of each slice. Three dimensional images of the whole sample can then be reconstructed by stacking all the slice images. This technique is quite time consuming, especially when the sample is relatively large. The milling process can also cut many internal structures, which may affect the image quality of the original structures.

2.5.2 Low Energy Helium Ion Microscopy

Currently, the only commercial microscopy using light ions is Helium Ion Microscopy (HIM). HIM utilizes a low energy (30-50KeV) helium ion beam to scan the sample and collect the ion induced secondary electrons. It is inherently less damaging to the sample than Ga ions although it will still sputter small amounts of material especially at high magnifications and long scan times. As helium ions can be focused into a small probe size and provide a much smaller sample interaction volume than high energy (>1 keV) electrons in the SEM, HIM can generate equal or higher resolution images with good material contrast and a higher depth of focus. At present, commercial instruments are capable of sub 1 nm resolution, which is based on high a brightness ALIS gas field ion source [34-36].

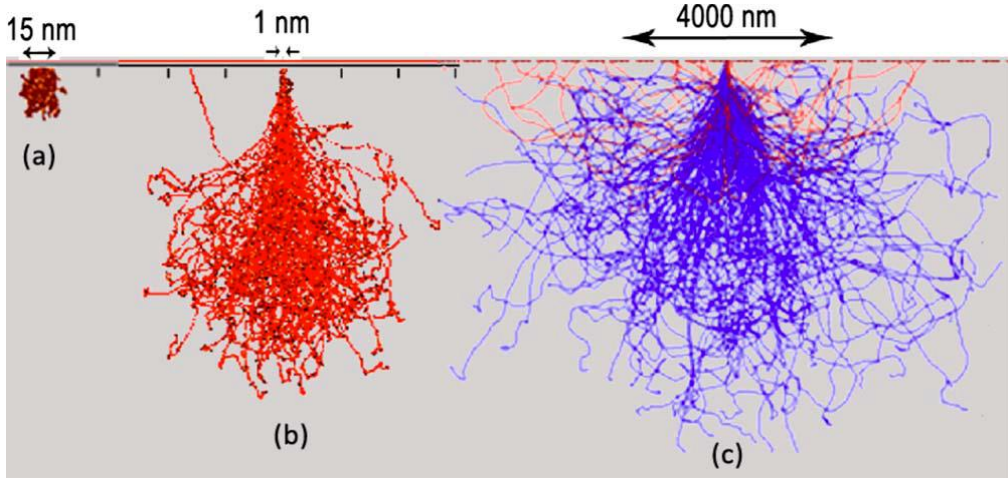


Figure 2.8 Comparison of interaction volumes for SHIM (center), SGIM (left), and SEM (right) in a Si sample. The interaction volume of SHIM is sharply peaked at the incoming point, allowing for a significantly smaller interaction radius than SGIM or SEM. In all three cases, the beam enters at the top of the figure and is simulated with zero width and E=30 KeV. (The SEM result is not to scale because of its significantly larger interaction volume). Reproduced from [36].

Figure 2.8 shows a typical cross section of a beam-sample interaction for a helium ion beam, in comparison with interactions for a gallium ion beam and an electron beam of the same beam diameter at 30 keV. The interaction volume of the HIM beam in Figure 2.8(b) is “thin” and localized for the first few dozens of nanometers before it begins to broaden due to nuclear collisions. In comparison, the Scanning Gallium Ion Microscopy (SGIM) interaction volume in Figure 2.8(a) is never truly localized; it broadens immediately upon entering the solid due to the dominant nuclear collisions in the interaction process. Furthermore for SEM at 30 keV in Figure 2.8(c), the electrons penetrate and scatter far more easily than either helium or gallium ions, and their interaction radius is therefore much larger.

Compared to an SEM, the secondary electron yield from HIM is much larger. Another advantage of the HIM is the ability to use an electron gun to neutralize beam induced charge. The HIM is superior to SEM in many aspects,

however, since the HIM is still based on secondary electron imaging and low energy helium ions, it is only applicable to surface imaging.

2.5.3 Nuclear Microscopy-MeV proton and helium ions imaging

The visualization of the interior cellular structures at nano-scale resolution is the dream of cell biologists. However, after a review of almost all biological imaging techniques, there is no well developed imaging technique that can truly realize this dream at present. Theoretical analysis and experiments in our group have shown that MeV protons and helium ions can be used for high resolution whole cell imaging and fulfill this dream.

Development of Nuclear Microscopy

Nuclear microscopy, mainly using focused MeV protons and helium ions as an illuminating source to scan the sample and collect different beam induced signals, dates back to the 1970s, when particles or proton induced X-ray emission (PIXE) was proposed and developed. PIXE analysis detects X-rays generated in the sample by MeV ions. This is the most widely used nuclear microprobe technique and has been applied to trace element analysis in the biomedical field [37]. Compared to using an electron probe, Microbeam PIXE has two main advantages: higher sensitivity and larger analytical depth. However, the best spatial resolution used for PIXE is still several hundred nanometers since it requires a beam current of at least 50-100 pA to be used for analysis.

The other two imaging and analytical techniques commonly used in nuclear microscopy are Rutherford Backscattered Spectroscopy (RBS) and Scanning Transmission Ion Microscopy (STIM). For a long time, RBS has been mainly used for broad beam analysis to determine sample stoichiometry and elemental

depth distributions. In scanning microbeam applications, RBS can be used as an important technique to determine the matrix composition (C, N, O) for light element analysis, which cannot be done with PIXE [37]. Both PIXE and RBS can be used for elemental analysis, however, even though PIXE has a larger cross section, for an accurate measurement, normally a beam current of 50-100 pA is required, which limits the spatial resolution of these two techniques. Compared to RBS and PIXE, STIM detects the transmitted ions, which requires a much smaller beam current (typically less than 1 pA for direct STIM). STIM was developed primarily as a method for quantitative imaging of the areal density distribution of thin biological samples and identifying features of interest for subsequent PIXE analysis or backscattered spectrometry. As the beam focusing ability has been gradually improved in the past several decades, STIM is playing a more and more important role in nuclear microscopy and microanalysis. Two dimensional STIM projection images and three dimensional reconstruction tomography of the group of cancer cells were presented in ref [38] with a spatial resolution in the order of 1 μ m in 2005. The research group at the LIPSION ion beam laboratory presented STIM tomography of biological specimens (cartilage cells) at a spatial resolution of 260 nm in 2006 [39]. Although these results showed the potential and advantage of imaging non-transparent specimens using STIM, they were still only at the level of optical microscopy. As discussed previously, STIM only requires a small beam current and is the best ion microscopy technique for high resolution imaging. The resolution of STIM is limited only by how well you can focus the proton or alpha particle beam. At the Centre for Ion Beam Applications (CIBA), NUS, a proton beam writing line with the

world's best MeV ion beam focusing ability has been developed [40]. In 2007, this beam line was used for biological single cell imaging using alpha particles. A STIM image of a single cell was obtained with a spatial resolution of 80x90 nm, well below the optical diffraction limit [41].

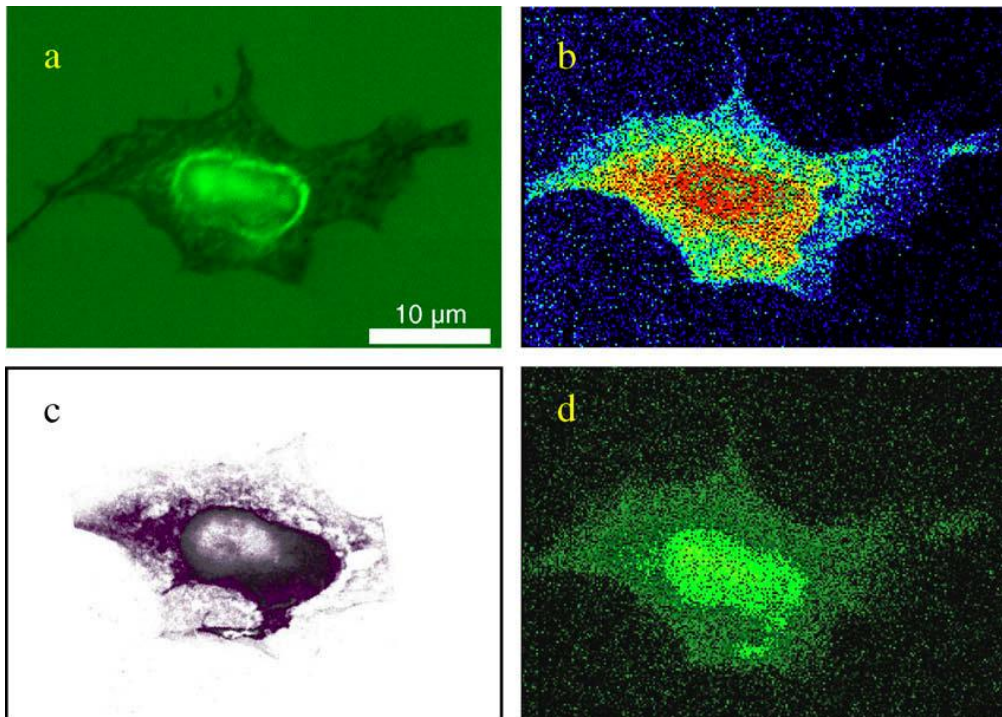


Figure 2.9 Images of a N2A cell stained with Sytox® Green Nucleic Acid Stain: (a) Confocal microscopy, (b) Proton STIM, (c) Alpha STIM, (d) Proton induced fluorescence. Reproduced from [42].

Preliminary imaging results in CIBA also showed that MeV protons can induce fluorescence from many common fluorophores. Proton Induced Fluorescence (PIF) imaging technique was potentially very useful for biological imaging [42]. Figure 2.9, shows an alpha STIM image of a whole cell with a resolution that is better than conventional confocal microscopy. More importantly, Figure 2.9d indicates that MeV proton beams can be used to excite fluorescence and that the signal is strong enough to form a good quality fluorescence image.

Theoretical analysis-MeV ion beam interaction with biological samples

- de Broglie wavelength

As discussed previously, the theoretical achievable resolution for a microscope is determined by wavelength of the illuminating beam used for imaging. For conventional optical microscopy, the typical wavelength is 550 nm; for soft X rays, the wavelength is several nm; for keV electrons, based on equation 2.2 the wavelength can be as low as 0.0037nm (100 KeV electron beam). For one MeV proton beam, the de Broglie wavelength is around 3×10^{-5} nm, in which case, the diffraction is not a problem at all for imaging.

- MeV proton beam trajectory

The trajectory of MeV protons in materials is dependent on the interaction of these protons with both the atomic electrons and nuclei in the material [43]. High energy protons penetrate deep and straight into a material, with a minimal amount of surface disruption for the following two reasons. Firstly, the probability of collisions between the incoming protons with the material's electrons is much higher than collisions with the nuclei of target materials; therefore as a first order approximation, only collisions with electrons needs to be considered for the calculation of beam trajectory. Secondly, since there is a large mismatch between the masses of the proton and electron ($m_p/m_e \approx 1800$), there is little change in the proton's momentum and quite small energy transfer to the target electrons for each collision. As a result, the trajectories of the incoming protons do not change much as they penetrate the material. Consequently, high energy protons can penetrate deep into a material while keeping a straight trajectory. Figure 2.10 is an SRIM simulation that shows that a 2 MeV proton beam can easily penetrate 5 μm human pancreas tissue.

The proton beam maintains a straight path with very little scattering even after a 5 μm thick biological specimen.

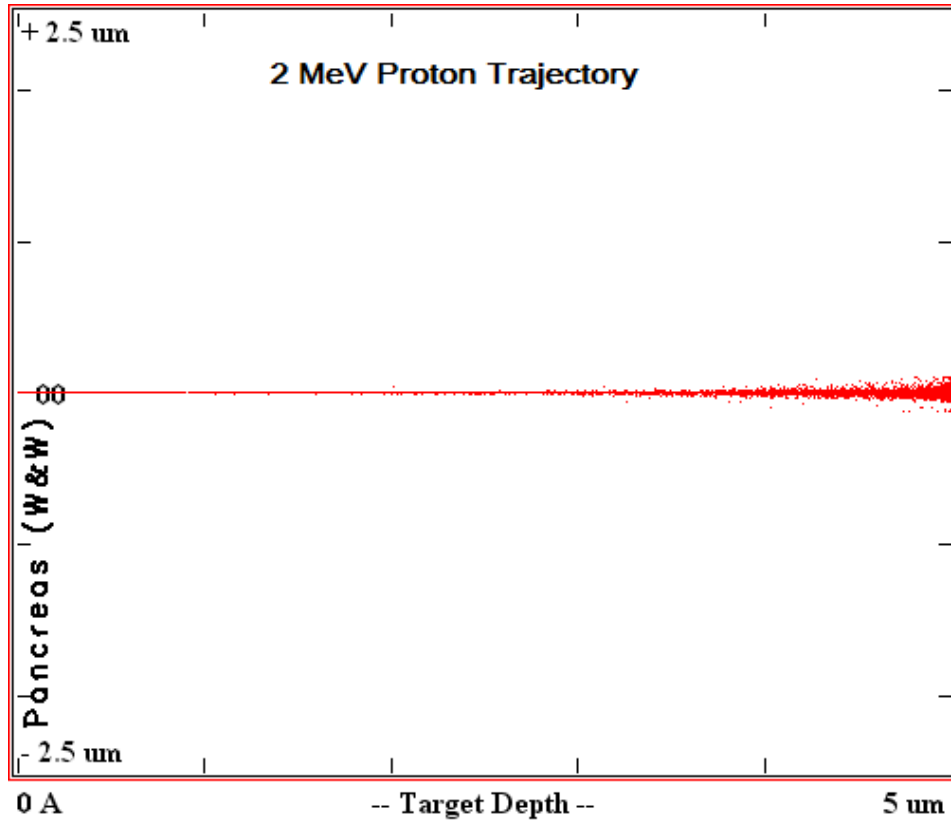


Figure 2.10 The trajectory of 2 MeV protons (1000) penetration into 5 μm human pancreas. [44]

- Spatial energy deposition profile of MeV protons and keV electrons
- keV electrons and MeV protons can probe spatial dimensions much smaller than the diffraction limit of photons and therefore are indispensable for high resolution imaging. Localized energy deposition is the key factor that determines the usefulness of high energy protons, electrons and photons. keV electrons and MeV protons have similar energy loss mechanisms; however the ion-electron mass disparity plays pivotal role in energy deposition. Electrons readily scatter off other electrons; the scattering leads to large (almost 100%) energy transfers and significant path deviations. However, due to the

significant mass and momentum mismatch between MeV protons and material electrons, ion-electron collisions have a much reduced energy transfer, therefore leaving the ion's path and energy almost unchanged. MeV ions produce low energy secondary electrons (δ rays) which have a maximum energy of approximately 2 keV for 1 MeV protons and are ejected at almost right angles to the ion's path. Low energy δ rays cannot penetrate far so they tightly surround the primary proton beam. The extent of energy localization depends on the ion/electron energy. Lower energy cause more localized deposition; however, it also leads to shallower depths. In summary, compared to keV electrons, MeV protons scatter less, produce less energetic delta rays and can probe deeper, making them superior to electrons in microscopy especially for imaging relatively thick samples (several μm).

The energy delocalization for primary protons is predominantly due to delta ray production propagation. Thus, the energy deposition profile for protons will depend on the energy spectrum of the generated delta rays. Although most of the generated **delta** rays are made up of low energy electrons, the maximum energy of secondary electrons increases with the energy of the primary protons. The energy delocalization for primary electrons is not limited by **delta** rays since the primary electrons can also easily be scattered with high energy. In addition, the successive generations of delta rays can also contribute to the energy deposition profile. These factors, coupled with Plasmon generation, lead to a broadening of the final electron energy deposition profile [45].

Figure 2.11 a, b, c shows the energy deposition profile for 3 MeV, 1 MeV and 500 keV protons penetrating into 500 nm thick Poly(methyl methacrylate) (PMMA). As a comparison, the bottom figure d, e, f shows the energy

deposition profile for 100 keV, 25 keV and 10 keV electrons. These plots show that while the proton-energy profiles are confined to a narrow radial cylinder, especially for the case of 500 keV protons, for the electron energy-deposition profiles there is an increasing radial extent with depth coupled with a shadow cone in the energy deposition centred around the primary beam axis.

These profiles agree with our above analysis.

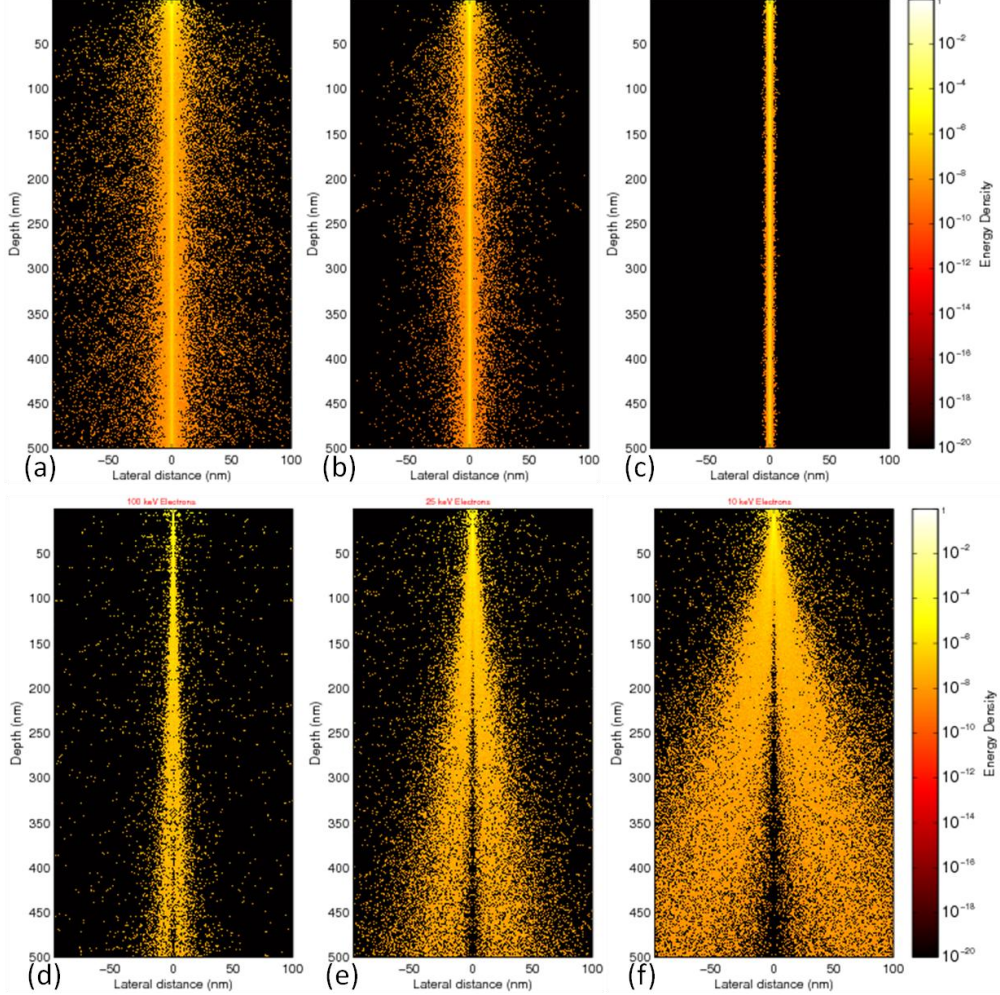


Figure 2.11 Simulations of the radial deposition of energy. The top images correspond to 3000, 1000, and 500 KeV protons while the bottom to 100, 25, and 10 KeV electrons. Reproduced from [45].

As Figure 2.12 shows, the electron energy deposition profile is very compact at the first layer (100 nm) but increases rapidly with penetration depth due to multiple scattering. While for 3 MeV protons, the energy profile is confined to

a narrow cylinder all the way without any significant broadening. Furthermore, most of the energy is deposited tightly (10nm) around the primary protons, due to the small energy of generated secondary electrons.

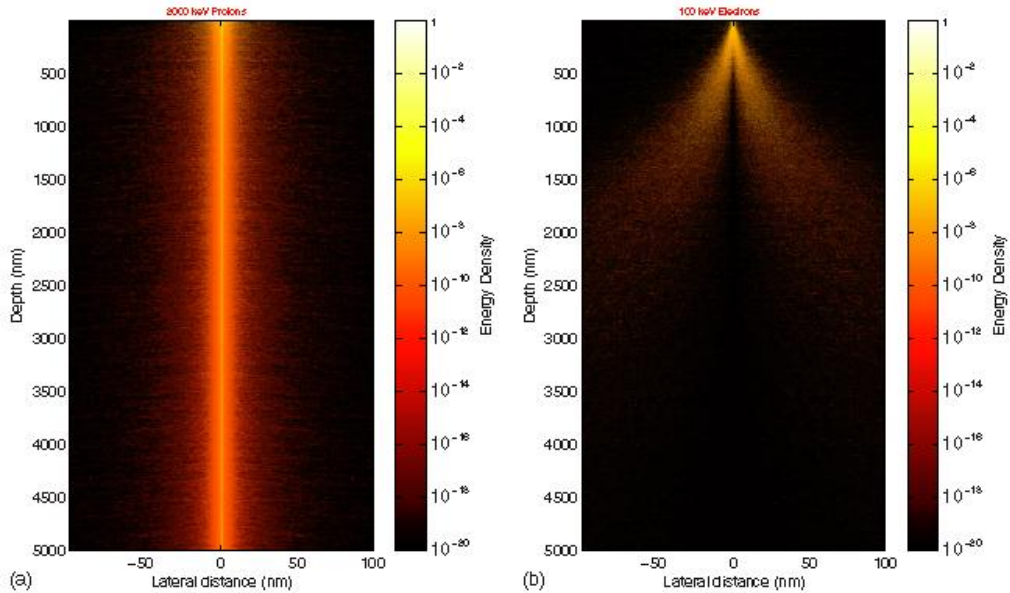


Figure 2.12 Pictorial representation of the radial deposition of energy for 2 MeV protons (a) and 100 KeV electrons (right) for a 5 μm thick layer of PMMA. Reproduced from [45].

- Advantage of using MeV proton and alpha for imaging

MeV protons and helium ions have even smaller de Broglie wavelength than keV electrons and soft X ray, therefore they can easily break the optical diffraction limit and theoretically can be focused down to a much smaller spot size than electron and X-ray. Secondly, non-transparent objects can be studied in contrast to confocal laser scanning microscopy; however, samples have to be in vacuum. The sample preparation for vacuum analysis is fairly straight forward. Freeze-dried samples without metal staining and dye labeling are adequate, which greatly reduces the risk of introducing artifacts. Electron tomography is an emerging new technique; however sample dimensions have to be far below 1 μm due to excessive lateral straggling. Thirdly, the radiation

dose used for transmission ion microscopy is about two orders of magnitude lower compared to transmission X ray microscopy and micro-tomography; thus no cryo-fixation is required and radiation damage plays little role [39].

2.6 Summary

The Centere for Ion Beam Applications (CIBA), NUS, Singapore has demonstrated the world leading MeV proton and helium ion beam focusing ability with a spot size of below 100 nm. With improvements to the current system, the focusing ability can be improved to a spot size of below 50 nm, or better. Considering the superior properties of MeV proton interaction with materials, high resolution (below 50 nm) whole cell imaging using MeV protons and helium ions is a promising technique that is potentially superior to current imaging techniques. Scanning Transmission Ion Microscopy and Proton Induced Fluorescence are two possible high resolution techniques and will be studied in this thesis. The resolution of these two techniques is approximately the spot size of the beam, which can be improved to sub-50 nm. Table 2-2 compares the four commonly used cell imaging techniques. These four techniques are using different illumination sources from laser light, electron beam, soft X-ray to MeV proton and helium ions.

As the table shows, compared to these competing techniques, MeV proton and helium ions imaging has its unique advantage and significance. It is therefore worthwhile to build up a dedicated beam line to improve the beam resolution, and to enable PIF and STIM imaging on biological samples. In the following chapters, the construction, implementation and biological application of this beam line will be discussed in detail.

Table 2-2 Comparison of most commonly high resolution microscopic techniques

Structural imaging technique	Biological state	Information	Spatial resolution	Maximal depth	Disadvantages
MeV proton or alpha	Freeze-dried	Morphology using STIM; Fluorescence using PIF; Elemental analysis using PIXE or RBS	For STIM or PIF, possible to 25 nm or even lower; PIXE and RBS: several hundred nm;	Adjustable by beam energy; can go up to 10 μ m or more	Not applicable to live cells.
Electron microscopy and tomography	Cryofixed hydrated sections; Cryofixed, freeze-substituted and plastic embedded sections	Morphology (by electron transmission) down to the molecular level; Elemental analysis using energy filtered electron microscopy Cathodoluminescence	TEM spatial resolution: sub nm; Tomography: down 1-10nm with thin sample	<500 nm	Only applicable to thin slice; complicated sample preparation
X-ray microscopy and tomography	Cryofixed freeze-dried or hydrated	morphology using absorption, phase contrast and diffraction; Elemental analysis using X-ray fluorescene	Down to 25-60 nm	Up to 10 μ m	synchrotron Facilities; high radiation damage;
Confocal fluorescence microscopy	Live cells	Fluorophores can give access to specific structures	Down to 250 nm	Cell depth	Optical diffraction limit; Fluorescence based
Super resolution optical microscopy	Most applicable for Live cells	Fluorescence labeled to specific structures	Down to 20-100 nm	Cell depth	Fluorescence based, Stringent requirements on fluorophores

Chapter 3 The Design, Implementation and Commissioning of the Cell Imaging Facility

3.1 MeV ion Beam Focusing

3.1.1 Quadrupole Lens

The technology behind the focusing of electron beams is well established. The electron microprobe frequently employs magnetic solenoids which produce their main component of magnetic field parallel to the beam axis. As the electrons diverge through this field, they experience a force that returns them towards the axis. However, owing to the large mass disparity, the field strength required to focus 2 MeV protons turns out to be as much as 430 times stronger than that necessary for 20 KeV electrons, and fields of this magnitude are difficult to achieve without using complicated superconducting solenoids. Compared to these ‘weak’ focusing lenses for electron beam focusing, a much stronger focusing action can be achieved when the main component of the magnetic field is perpendicular to the beam axis, and it is these ‘strong’ focusing lenses which are used to focus high energy ion beams.

The most suitable strong focusing lenses for MeV proton and alpha particles are magnetic quadrupole lenses [46]. The schematic design of a quadrupole lens is shown in Figure 3.1. The field is created by four poles arranged symmetrically about the axis and excited alternately NSNS. The magnetic field lines between the poles are illustrated in figure 3.1 by blue lines. Because of the symmetry, the field on the axis is zero, and moving away from the axis, the field strength increases proportionally to the distance from the center. The lens effects its focusing action via Lorentz force as

$$F = q\vec{v} \times \vec{B} \quad \text{Eq 3.1}$$

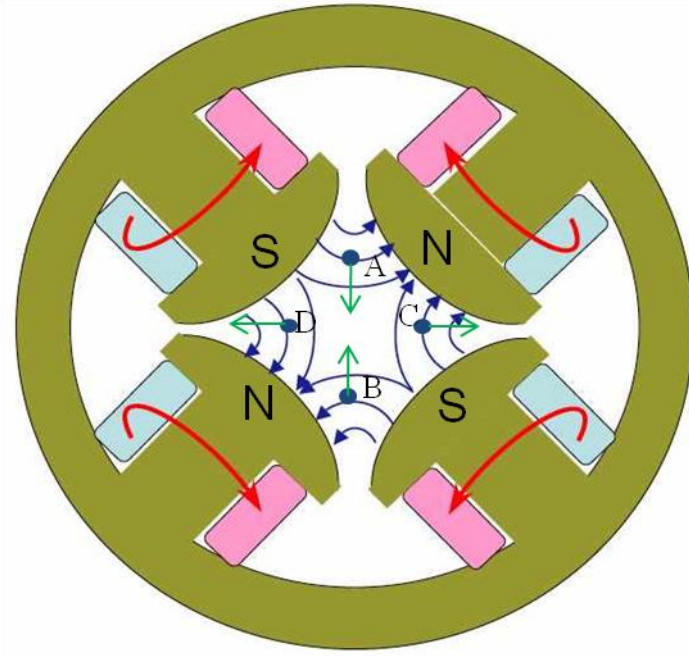


Figure 3.1 A schematic design in a quadrupole lens. Also shown are the lines of field inside the lens and the forces acting on a positively charged particles travelling into the plane of the paper at various points in the quadrupole aperture (A to D). A and B lie in the converging plane, while C and D are in the diverging plane.

A charged particle moving in a magnetic field experiences a force perpendicular to both its direction of motion and the transverse magnetic field component, and so a particle travelling in the anti-symmetry plane at A will experience a force directing it towards the horizontal axial plane. On the opposite side of the lens, at B, the direction of the field is reversed and so the force is still directed towards the horizontal axial plane. The force in regions C and D however direct the particle away from the vertical axial plane, and therefore in these regions a defocusing effect takes place.

As a result, a single quadrupole field tends to converge the particles in one direction while in the orthogonal direction the particles diverge. As Figure 3.2 shows, a square shaped beam entering the quadrupole field will become focused in the horizontal direction, but diverge strongly in vertical direction, resulting

in a vertical line focus. Therefore, for a quadrupole probe forming system, it is necessary to have at least two focusing lens to achieve a point focus.

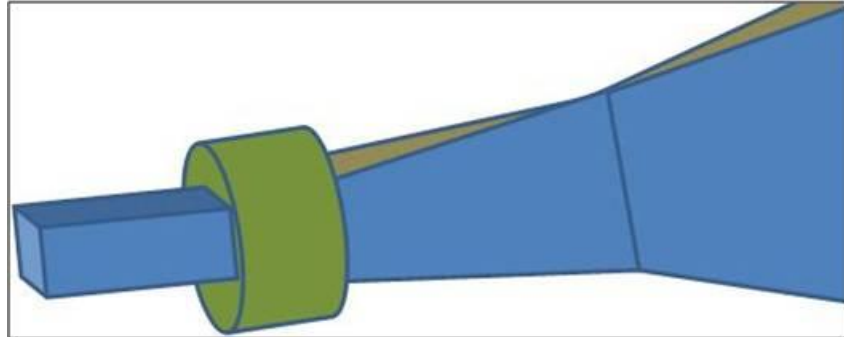


Figure 3.2 The effect of a single quadrupole lens on a charged particle beam entering from the left of the picture.

Probe Forming System

As discussed above, a single lens is only capable of forming a line focus. A point focus can be obtained by combining two or more quadrupoles of alternating polarity arranged to give overall focusing in each plane. There are many ways in which quadrupole lenses can be positioned and excited to obtain a point focus, and each configuration has different demagnification and aberration properties. In the following session, basic ion optics will be introduced, followed by further discussions on some properties of probe forming systems [47].

3.1.2 Basic Theory of Ion Optics

To help understand the further analysis on different probe forming systems, this section describes the general principle and mathematical formalism [37, 46] used in the simulation software such as PBO Lab (Particle Beam Optics Lab) [48].

(1) Matrix Descriptions of Beam Transport

The interaction of a charged particle through a system of magnetic lenses can be treated by a process of matrix multiplication. At any specified position in the system an arbitrary charged particle is represented by a vector (single column matrix) X , whose components are the positions, angles, and momentum of the particle with respect to the reference trajectory, i.e.

$$X = \begin{pmatrix} (x) \\ (\theta) \\ (y) \\ (\varphi) \\ (l) \\ (\delta) \end{pmatrix} \quad \text{Eq 3.2}$$

Definitions:

x = the horizontal displacement of the arbitrary ray with respect to the assumed central trajectory;

θ = the angle this ray makes in the horizontal plane (xoz) with respect to the assumed central trajectory;

y = the vertical displacement of the ray with respect to the assumed central trajectory;

φ = the divergence angle of the ray projected onto yoz plane with respect to the assumed central trajectory;

l = the path length difference between the arbitrary ray and the central trajectory;

$\delta = \Delta p/p$ is the fractional momentum deviation of the ray from the assumed central trajectory.

(2) First Order Theory

Transfer Matrix

The magnetic lens is represented to first order by a square matrix R , which describes the action of the magnet on the particle coordinates. Thus the passage of a charged particle through the system may be represented to first order by the equation:

$$X(1)=RX(0) \quad \text{Eq 3.3}$$

where $X(0)$ is the initial coordinate vector and $X(1)$ is the final coordinate vector of the particle under consideration. The same transformation matrix R is used for all such particles traversing a given magnet. From the equation, the components of R can be identified as the first order coefficients:

$$R = \begin{pmatrix} R_{11} & \dots & R_{16} \\ \vdots & \ddots & \vdots \\ R_{61} & \dots & R_{66} \end{pmatrix} = \begin{pmatrix} (x/x) & (x/\theta) & (x/y) & (x/\varphi) & (x/l) & (x/\delta) \\ (\theta/x) & (\theta/\theta) & (\theta/y) & (\theta/\varphi) & (\theta/l) & (\theta/\delta) \\ (y/x) & (y/\theta) & (y/y) & (y/\varphi) & (y/l) & (y/\delta) \\ (\varphi/x) & (\varphi/\theta) & (\varphi/y) & (\varphi/\varphi) & (\varphi/l) & (\varphi/\delta) \\ (l/x) & (l/\theta) & (l/y) & (l/\varphi) & (l/l) & (l/\delta) \\ (\delta/x) & (\delta/\theta) & (\delta/y) & (\delta/\varphi) & (\delta/l) & (\delta/\delta) \end{pmatrix}$$

Eq 3.4

For a static magnetic system with midplane symmetry, a good deal of simplification occurs. Many of the matrix elements become zero. For the case of an on-axis centroid, the transfer matrix then becomes:

$$R = \begin{pmatrix} R_{11} & \dots & R_{16} \\ \vdots & \ddots & \vdots \\ R_{61} & \dots & R_{66} \end{pmatrix} = \begin{pmatrix} (x/x) & (x/\theta) & 0 & 0 & 0 & (x/\delta) \\ (\theta/x) & (\theta/\theta) & 0 & 0 & 0 & (\theta/\delta) \\ 0 & 0 & (y/y) & (y/\varphi) & 0 & 0 \\ 0 & 0 & (\varphi/y) & (\varphi/\varphi) & 0 & 0 \\ (l/x) & (l/\theta) & 0 & 0 & 0 & (l/\delta) \\ 0 & 0 & 0 & 0 & 0 & (\delta/\delta) \end{pmatrix} \quad \text{Eq 3.5}$$

The Magnification and Demagnification

The magnifications and the demagnifications can be obtained from the first order transfer matrix of the complete lens system. The cardinal elements are defined for a lens system in which there is no coupling between the xoz and yoz plane; that is

$$(x/y) = (x/\varphi) = (\theta/y) = (\theta/\varphi) = (y/x) = (y/\theta) = (\varphi/x) = (\varphi/\theta) = 0.$$

This condition applies in systems consisting of quadruples and drift spaces in which the quadruples are correctly aligned. The magnification and demagnification of a lens system, expressed in terms of the elements of the transfer matrix, and defined by Eq 3.6 and Eq 3.7 provided the system is stigmatic with $(x/\theta) = (y/\varphi) = 0.$

Magnification: $M_x = (\theta/\theta)^{-1} = R_{22}^{-1}$ Eq 3.6
 $M_y = (\varphi/\varphi)^{-1} = R_{44}^{-1}$

Demagnification: $D_x = (\theta/\theta) = R_{22}$ Eq 3.7
 $D_y = (\varphi/\varphi) = R_{44}$

The probe in a nuclear microprobe system is the demagnified image of the object collimator. The sign of the magnification is not important, while the demagnification is quite important. It is desirable that the demagnifications be as large in absolute value as possible so that a greatly demagnified image of the object aperture is focused on the target, although it is also important that the corresponding aberrations are not too large.

Astigmatism Coefficients

The distances from the point at which the transfer matrix is calculated to the x and y image planes are

$$C_{10} = \frac{(x/\theta)}{(\theta/\theta)} = \frac{R_{12}}{R_{22}} \quad \text{Eq 3.8}$$

$$C_{01} = \frac{(y/\varphi)}{(\varphi/\varphi)} = \frac{R_{34}}{R_{44}}$$

The system is stigmatic if $C_{10}=C_{01}$, and the transfer matrix has been calculated at the common image plane of a stigmatic system if $C_{10}=C_{01}=0$. In the latter case, the system is said to be in focus. In the PBO program, it is set as $R_{12}=R_{34}=0$ for system stigmatization. As a consequence of Liouville's theorem, then,

$$\begin{aligned} (\theta/\theta) &= (x/x)^{-1} \\ (\varphi/\varphi) &= (y/y)^{-1} \end{aligned} \quad \text{Eq 3.9}$$

The quantities $(x|\theta)$ and $(y|\varphi)$ are termed the astigmatism coefficients, which are R_{12} and R_{34} respectively in the transfer matrix. The quantities $(x|\varphi)$ and $(y|\theta)$, which are only nonzero if the quadruples are rotationally misaligned, are called the skew astigmatism coefficients.

(3) Higher Orders

The Eq 3.3 may be extended to second order by the addition of another term. The components of the final coordinate vector, in terms of the original, are now given as

$$X_i^{(1)} = \sum_j R_{ij} X_j^{(0)} + \sum_{jk} T_{ijk} X_j^{(0)} X_k^{(0)} \quad \text{Eq 3.10}$$

where T is the second order transfer matrix. Second order calculation can be done if an element is provided which specifies second order calculation in the program PBO.

Third order terms may also be included in the transformation of the particle coordinate vector. The third order terms are given in terms of the U matrix so that our transformation equation becomes

$$X_i^{(1)} = \sum_j R_{ij} X_j^{(0)} + \sum_{jk} T_{ijk} X_j^{(0)} X_k^{(0)} + \sum_{jkl} U_{ijkl} X_j^{(0)} X_k^{(0)} X_l^{(0)}$$

Eq 3.11

In program PBO, the addition of a parameter to the element which specifies second order allows calculations to be done to third order.

Dominant Aberrations

The aberration coefficients are representations of different physical effects, which maybe degrade the imaging and ultimately limit the resolution obtained. Each different aberration changes the image coordinates by an amount depending on the strength of the aberration and some combination of the initial ray coordinates or the system parameters. The combined effect of the aberrations can be expressed as a series of terms such as

$$x_i = x / D_x + C_1 \delta + C_2 \theta + C_3 \theta \delta + \dots + C_n \theta \varphi^2 + C_{n+1} \theta^3 + \dots \quad \text{Eq 3.12}$$

In Eq 3.12, the C terms are quantities which express the strength of the particular aberration and are known as aberration coefficients. In order to denote exactly to which system parameters a particular coefficients relates, Dirac notation can be used. For example, C_2 would be written as $\langle x | \theta \rangle$ and C_n as $\langle x | \theta \varphi^2 \rangle$, which corresponds to an element in the transfer matrix R, T and U. For example, $\langle x | \theta \rangle$ corresponds to (x / θ) in R matrix, which is R12.

On this basis we can distinguish two different types of aberration: ‘intrinsic’ aberrations, which occur even in a theoretically perfect lens as a result of the finite size, divergence or energy spread of the beam, and ‘parasitic’

aberrations, which arise as a result of departures from perfection such as poor construction tolerances or misalignment of the lenses. Obviously, parasitic aberrations can in principle be eliminated by improving construction techniques, while intrinsic aberration set a lower barrier on the attainment of small spot sizes.

Chromatic Aberrations

Chromatic aberration is an important intrinsic imaging aberration affecting quadrupole systems. It arises as a result of the dependence of the focusing force on the velocity of the particle, and can be particularly damaging in ion probes if there is a relatively large energy spread in the particle beam from high energy accelerators. Chromatic aberration is characterized by the terms $\langle x|\theta\delta\rangle$ and $\langle y|\varphi\delta\rangle$, corresponding to T_{126} and T_{246} in the second order transfer matrix; that is, the broadening in each direction is proportional to the product of the entrance divergence in that direction and the percentage momentum spread of the beam.

Spherical Aberrations

Spherical aberration is the only other intrinsic aberration that has any significant effect in microprobe systems. It arises as a result of the slightly different forces experienced by particles travelling at an angle to the axis of the lens, and is characterized by the terms $\langle x|\theta^3\rangle$, $\langle x|\theta\varphi^2\rangle$, $\langle y|\varphi^3\rangle$, and $\langle y|\theta^2\varphi\rangle$, which is corresponding to U_{1222} , U_{1244} , U_{3444} , and U_{3224} in the third order transfer matrix in PBO program. These 4 intrinsic aberrations are usually quite different in magnitude, with the largest aberrations occurring in the plane of least demagnification.

Aberrations due to misalignment

The dominant parasitic aberrations are those due to imperfect mechanical construction of the quadrupole lens leading to higher order multipole contamination of the quadrupole field. A second important source of parasitic aberration can be caused by any misalignment of the quadrupole lenses relative to the optical axis of the system. Three types of mechanical misalignment can be encountered: transverse and tilt misalignments of the lens with respect to the optical axis, and misalignment in the rotation of each lens with respect to each other. With suitable mechanical construction of the lenses, and a correct alignment procedure, these intrinsic aberrations can be minimized.

3.1.3 Quadrupole Probe-forming Systems and Analysis

As discussed in 3.1.1, several quadrupole lenses must be combined together to obtain a point focus. At present, there are many different configurations using three or four lens together which enable a point focus at relatively high demagnification. We have studied several configurations which are in common use, to enable us to select the best lens configuration for the cell imaging facility.

The Oxford Triplet

The Oxford Triplet magnetic quadrupole lens configuration (\overline{CDC}) is shown in Figure 3.3, and is the configuration used in all of our current beam lines in CIBA. The Oxford Triplet is a high excitation lens system with unequal demagnifications in the x and y directions. The individual quadrupole lenses are arranged in a Converging-Diverging-Converging configuration with the first two connected so as to carry the same current. With the use of the compact small bore Oxford Microbeams OM52 high demagnification lenses,

CIBA has managed to achieve a world record spot size of 35nm X 75nm. This configuration has a demagnification of 220 and 70 in the X and Y directions at a working distance of 0.07 m. The quadrupole lenses have a width of 0.055 m and bore radius of 0.00375 m, and the spacing between each lens is 0.025 m.

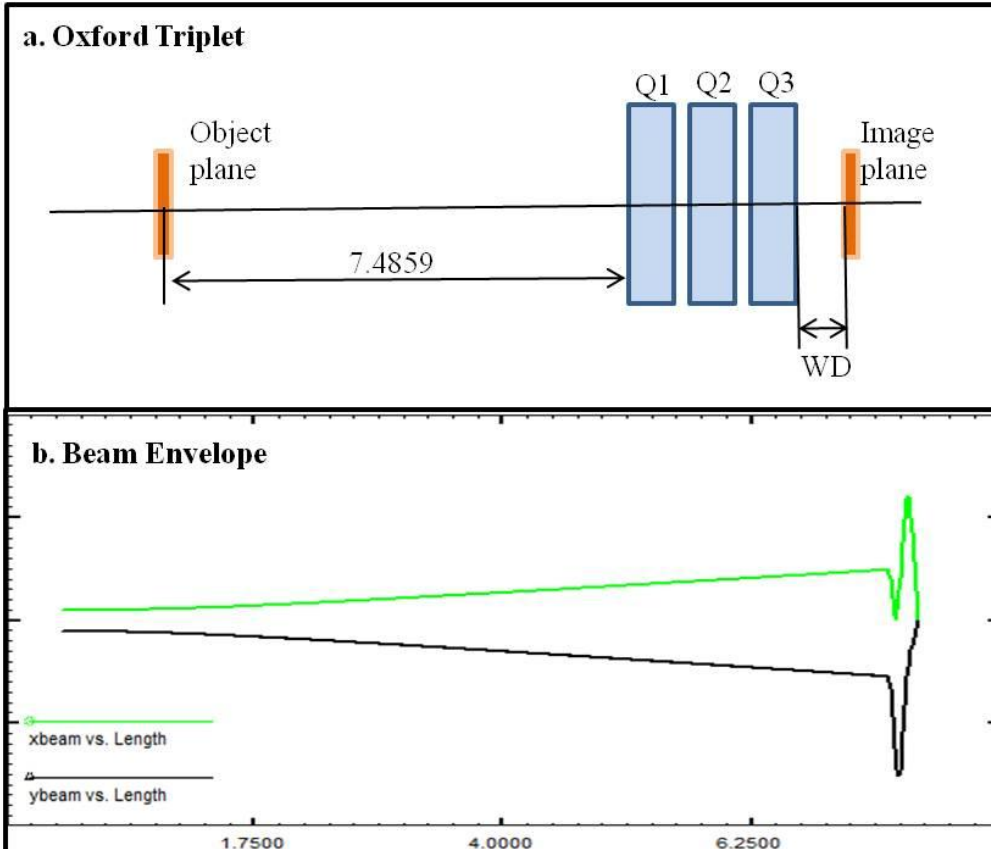


Figure 3.3 Current CIBA proton beam writing probe-forming lenses configuration. Fig a shows the lenses configuration with a workgin distance (WD) of 0.07 m. Fig b show the x and y beam envelopes in the beam trajectory.

Table 3-1 lists the important beam optics parameters and simulated magnetic fields at each quandrupole pole tip. This configuration has been successfully implemented in CIBA, with the experimental results showing good agreement with the theoretical parameters listed in the table.

Table 3-1 Main beam optics parameters for the CIBA proton beam writing line. WD is working distance as show in Figure 3.3; Simulations are using PBO based on 2 MeV protons and current CIBA accelerator beam status.

Working distance (WD) unit is m			0.07	
Non-Zero Abberation Coefficients - units are microns and milliradians	1st order- demag	$1/\langle x x \rangle$	220	
		$1/\langle y y \rangle$	-57	
	2^{nd} order- chrom. um/mr/%energy spread	$\langle x \theta\delta \rangle$	-371	
		$\langle y \phi\delta \rangle$	948	
		$\langle x \theta^3 \rangle$	2016	
		$\langle x \theta\phi^2 \rangle$	2509	
		$\langle y \phi^3 \rangle$	-9410	
	3^{rd} order- spherical um/mr ³	$\langle y \theta^2\phi \rangle$	-9618	
Field at Q1 pole tip (T)			0.38693	
Field at Q2 pole tip (T)			-0.38693	
Field at Q3 pole tip (T)			0.445	

For many of the configurations, a point focus may be achieved at the same image distance corresponding to several different values of the quadrupole excitations. These different values of excitation can be related to different paths of the beam as it traverses the lens system. If the demagnification in a particular plane is negative, then using the definition $D_x = \langle \theta | \theta \rangle$, it follows that a ray must emerge from the lens system with the opposite slope to that with which it entered the system. For a positive image distance, this can only take place if the ray does not cross the axis or if the ray crosses the axis an even number of times. Similarly, if the demagnification is positive, the rays must cross the axis an odd number of times. For the systems discussed in this part,

the number of cross over is never more than one, so it may be stated that if $D<0$ there is no crossover and if $D>0$ there is a crossover.

Spaced Oxford triplet

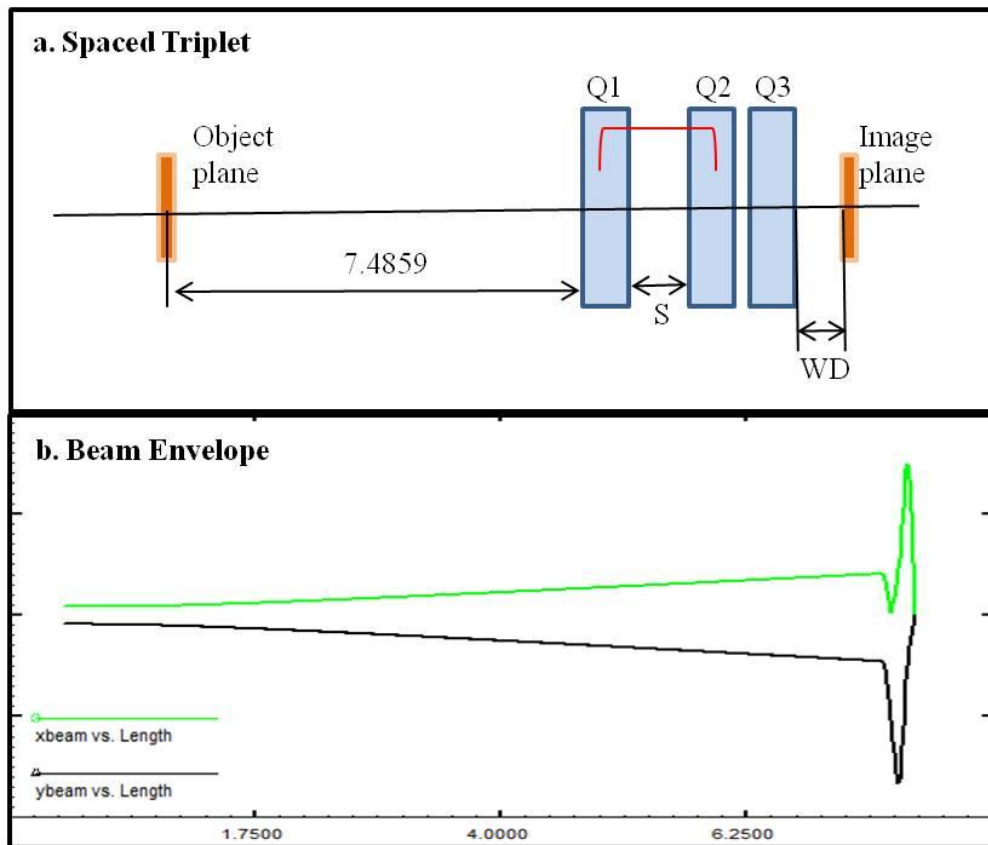


Figure 3.4 Spaced triplet configuration (Fig. a) and its beam envelop (Fig. b). S is the space between coupled Q1 and Q2; WD is the working distance.

As Figure 3.4 shows, the spaced triplet (\overline{CDC}) differs from the Oxford triplet only in that a gap has been introduced between the coupled lenses Q1 and Q2. It also has a quite similar beam envelope. For the Oxford triplet and spaced Oxford triplet, $Dx>0$ and $Dy <0$ indicate that they have a crossover in X direction. Table 3-2 lists all the simulated beam optics coefficients for the spaced Oxford triplet, for different working distances and spacings.

Table 3-2 Beam optics parameters for spaced triplet under different WD and S. Simulations are using PBO based on 2 MeV protons and current CIBA accelerator beam status.

Working distance (WD) unit is m			0.03	0.03	0.04	0.04	0.05	0.05	
Space (S) unit is m			0.08	0.16	0.08	0.16	0.08	0.16	
Non-Zero Abberation Coeeficient s - units are microns and milliradians	1st order- demag	1/ $\langle x x \rangle$	574	790	472	648	396	543	
		1/ $\langle y y \rangle$	-93	-121	-87	-113	-82	-106	
	2^{nd} order- chrom. um/mr/%ene rgy spread	$\langle x \theta\delta\rangle$	-380	-486	-392	-495	-403	-504	
		$\langle y \varphi\delta\rangle$	1049	1211	1029	1179	1017	1156	
	3 rd order- spherical um/mr ³	$\langle x \theta^3\rangle$	7532	18990	6528	15520	5371	13111	
		$\langle x \theta\varphi^2\rangle$	4266	8914	4167	8569	4109	8322	
		$\langle y \varphi^3\rangle$	-13360	-21290	-12380	-19330	-11670	-17860	
		$\langle y \theta^2\varphi\rangle$	-26290	-58060	-22550	-49010	-19910	-42600	
Field at Q1 pole tip (T)			0.2727	0.2344	0.2649	0.2272	0.2583	0.2209	
Field at Q2 pole tip (T)			-0.2727	-0.2344	-0.2649	-0.2272	-0.2583	-0.2209	
Field at Q3 pole tip (T)			0.4917	0.4685	0.4328	0.4113	0.3904	0.3693	

Compared to the normal Oxford triplet, the spaced triplet demagnifications are higher in both X and Y directions. However, the spherical aberrations are also increased for the spaced triplet, especially in the Y direction. There is therefore a compromise in the spaced triplet performance: The geometric spot size will be smaller due to increased demagnification in both x and y

directions, but since the beam has to be collimated more to reduce the effects of the increased aberrations, then the beam current will be correspondingly less.

Spaced Quadruplet

The quadruplet, consisting of four quadrupole lenses, is currently being used by several groups (eg Leipzig and Melbourne), primarily because if the four lenses arranged CDDC are configured in the ‘Russian Quadruplet’ configuration (ie Q1-Q4, and Q2-Q3 linked) then the system is orthomorphic, ie the system demagnification parameters are the same in both x and y directions. This has the advantage that the geometric image spot size has the same aspect ratio as the object aperture size, although the performances in general have not been as good as those obtained by the Oxford Triplet configuration.

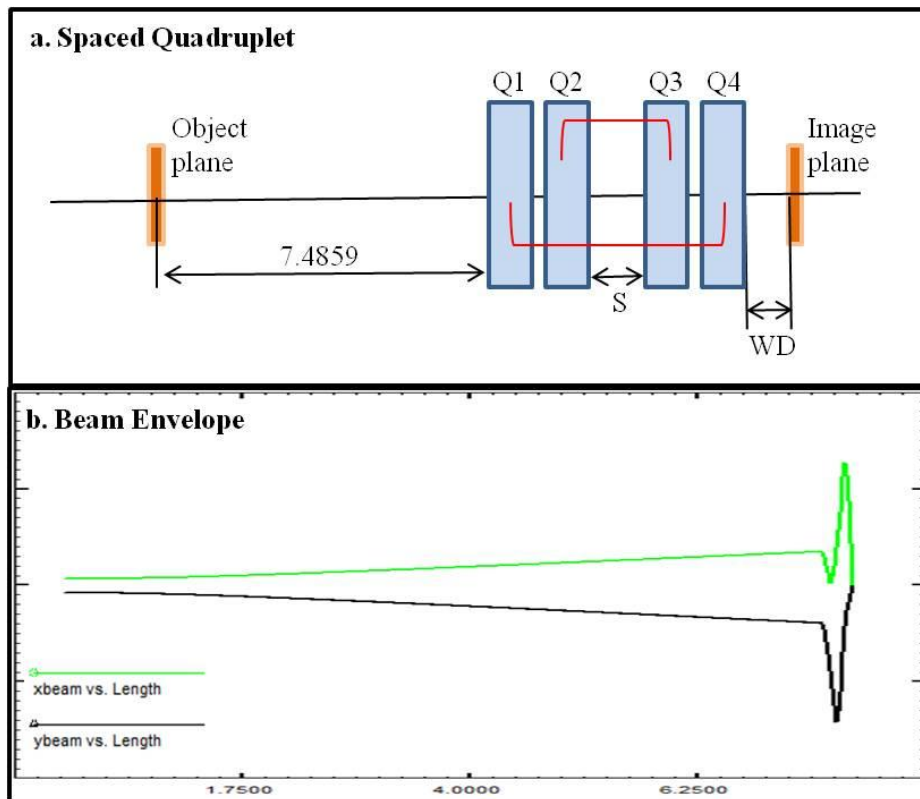


Figure 3.5 Spaced Quadruplet configuration (Fig. a) and its beam envelope (Fig. b). Q1 is coupled with Q4, while Q2 is coupled with Q3. S is the space between Q2 and Q3. WD is the working distance from Q4 to the image plane.

Table 3-3 shows the simulated beam optics parameters for the spaced quadruplet. The demagnification is around 180 with a working distance of 3 cm and a space of 8 cm. It can be increased as the working distance becomes smaller or the space becomes bigger. However, the chromatic and spherical aberrations are also increased as the demagnification increases, and generally the spherical aberrations are extremely high compared to Oxford triplet. With regard to practicalities, it is more difficult to focus the beams using the Russian quadruplet, since focusing requires many more iterations between minimizing the x and y astigmatism compared with the Oxford Triplet.

Table 3-3 Beam optics parameters for spaced quadruplet under different WD and S. Simulations are using PBO based on 2 MeV protons and current CIBA accelerator beam status.

Working distance (WD) unit is in m			0.03	0.03	0.04	0.04	0.05	0.05	
Space (S) unit is in m			0.08	0.16	0.08	0.16	0.08	0.16	
Non-Zero Abberation Coeeficien ts - units are microns and milliradian s	1 st order- demag	1/<x x>	181	261	165	219	144	187	
		1/<y y>	181	261	165	219	144	187	
	2 nd order- chrom.	<x θδ>	-6822	-3955	-4715	-3432	-4056	-3074	
		<y φδ>	-3308	-868	-1855	784	-1559	-747	
	3 rd order- spherical	<x θ ³ >	883600	422400	386600	268700	250100	184500	
		<x θφ ² >	224500	34770	81077	24950	52650	19330	
		<y φ ³ >	207100	15010	54500	9840	32510	7423	
		<y θ ² φ>	219500	34770	81070	24950	52650	19330	
Field at Q1 pole tip (T)			0.8908	0.5750	0.6674	0.4997	0.5790	0.4479	
Field at Q2 pole tip (T)			-0.3122	-0.2504	-0.2994	-0.2437	-0.2926	-0.2383	
Field at Q3 pole tip (T)			0.3122	0.2504	0.2994	0.2437	0.2926	0.2383	
Field at Q4 pole tip (T)			-0.8908	-0.5750	-0.6674	-0.4997	-0.5790	-0.4479	

Calculation of the probe size using simulation parameters

Considering the practical difficulties of focusing the beam using the Russian Quadruplet, the increased aberrations and the relatively poor performances for the quadruplet by other groups, we have opted for the spaced triplet design for

our cell imaging beam line. In this section we calculate the aberrations and the final probe size for the spaced Oxford Triplet, based on computer simulations.

The results of the aberrations are shown in **Table 3-4**.

Table 3-4 CIBA beam parameters and beam optics parameters required for probe size calculation

Experimental beam status		beam optics parameters		
Lens configurations	Single spaced (0.08m) triplet	1 st order- demag	1/<x x>	574
Particle	2 MeV proton		1/<y y>	-93
Object distance	7.4859 m	2 nd order- chrom. um/mr/ %energy spread	<x θδ>	-380
Object Aperture	$10 \times 2 \mu\text{m}^2 (x = \pm 10 \mu\text{m}, y = \pm 1 \mu\text{m})$		<y φδ>	1049
Collimate Aperture	$40 \times 20 \mu\text{m}^2 (x = \pm 20 \mu\text{m}, y = \pm 10 \mu\text{m})$	3 rd order- spherical um/mr ³	<x θ ³ >	7532
Momentum spread	0.001% ($\delta = \pm 0.0005\%$)		<x θφ ² >	4266
Entrance angle divergence	$\theta_{\max} = 0.0013 \text{ mrad}$ $φ_{\max} = 0.0012 \text{ mrad}$		<y φ ³ >	-13360
Working distance	0.03 m		<y θ ² φ>	-26290

(1) First-order spot size:

$$X_{1st} = 10 \mu\text{m} / |Dx| = 17.42 \text{ nm} \quad \text{Eq 3.12}$$

$$Y_{1st} = 2 \mu\text{m} / |Dy| = 21.51 \text{ nm}$$

(2) The second-order chromatic aberration increases the spot size equally

in the positive and negative X direction and Y direction by an amount

$$\begin{aligned}\Delta X_{ch} &= |\langle x | \theta \delta \rangle \theta_{\max} \delta_{\max}| \\ \Delta Y_{ch} &= |\langle y | \varphi \delta \rangle \varphi_{\max} \delta_{\max}|\end{aligned}\quad \text{Eq 3.13}$$

Therefore, the total broadening in the X direction is then $2\Delta X_{ch}$:

$$\begin{aligned}2\Delta X_{ch} &= 2(380 \times 0.0013 \times 0.0005) = 5.1 \times 10^{-4} \mu m = 0.51 nm \\ 2\Delta Y_{ch} &= 2(1049 \times 0.0012 \times 0.0005) = 1.26 \times 10^{-3} \mu m = 1.26 nm\end{aligned}$$

The effect of spherical aberration is to draw out the image of a point object

into four cusps. An examination of spherical aberration coefficients of

(3) Table 3-2 shows that the two coefficients relating to each plane of the system are always of the same sign. Thus the maximum extent of the spherical aberration pattern is given for the positive X direction as 0.0

$$\Delta X_{sph} = \left| \langle x | \theta^3 \rangle \theta_{\max}^3 + \langle x | \theta \varphi^2 \rangle \theta_{\max} \varphi_{\max}^2 \right| \quad \text{Eq 3.14a}$$

$$, \text{ similarly } \Delta Y_{sph} = \left| \langle y | \varphi^3 \rangle \varphi_{\max}^3 + \langle y | \theta^2 \varphi \rangle \theta_{\max}^2 \varphi_{\max} \right| \quad \text{Eq 3.14b}$$

Therefore the total broadening in the two directions are $2\Delta X_{sph}$ and $2\Delta Y_{sph}$

respectively, where

$$\begin{aligned}2\Delta X_{sph} &= 2[7532 \times 0.0013^3 + 4266 \times 0.0013 \times 0.0012^2] = 0.05 \times 10^{-3} \mu m = 0.05 nm \\ 2\Delta Y_{sph} &= 2[13360 \times 0.0012^3 + 26290 \times 0.0013^2 \times 0.0012] = 0.15 \times 10^{-3} \mu m = 0.15 nm\end{aligned}$$

As a result, the final beam spot size can be obtained as

$$\begin{aligned}X &= X_{1st} + 2\Delta X_{ch} + 2\Delta X_{sph} = 17.42 + 0.51 + 0.05 = 17.98 nm \\ Y &= Y_{1st} + 2\Delta Y_{ch} + 2\Delta Y_{sph} = 21.51 + 1.26 + 0.15 = 22.92 nm\end{aligned}\quad \text{Eq 3.15}$$

The final maximum dimensions of the spot size are then $17.98 \times 22.92 nm^2$. As the calculation shows, for the input parameters as set out in Table 3-4, the second-order chromatic aberrations and third-order spherical aberrations altogether have caused the beam broadening of 0.56nm and 1.41nm in X and Y direction respectively, which are around 3% and 6% of the final beam

dimensions in each direction. The increase in spot size from chromatic and spherical aberrations in the X direction is especially low for the input conditions as given in table 3.4. These simulations are consistent with our experimental results on measurement of beam spot size, which is discussed in later sections.

3.2 Design of Cell Imaging Facility

3.2.1 Justification for a new cell and tissue imaging beam line

As discussed in the last session, using improved beam optical parameters, we should be able to improve on current performances of the existing CIBA beam focusing systems. Our eventual aim is to reach the predicted beam spot size of around 20nm or even smaller, which is around ten times smaller than the optical diffraction limit. Using such a finely focused beam, the potential exists for the implementation of a wide selection of high resolution ion imaging techniques. The justification for constructing this new facility is two-fold: (a) There is an increasing demand for high resolution techniques that can image biological cells in novel ways, applicable for example to cell biology, biomedicine and targeted delivery of pharmaceuticals, and (b) Recent work by the CIBA group [43, 45] has indicated that not only does a finely focused beam of MeV protons maintain resolution as it passes through a whole biological cell, but the induced secondary electrons are in general short range, and have a lateral span of only a few nanometers. This raises the interesting possibility that if we can focus the proton beam to spot sizes below 10 nm, then not only will we be able to image the interior structure of cells with high resolution using Scanning Transmission Ion Microscopy – STIM, but proton

induced fluorescence (PIF) microscopy can also be realized at resolutions below 10 nm.

The design specifications of the new facility are as follows: (a) Sub 50 nm resolutions (at low proton current), featuring high demagnification imaging and short lens–image distance, (b) the capability of STIM, secondary electron and fluorescence imaging, (c) the potential capability of PIXE and RBS, although it must be noted that since these techniques require at least 100 pA proton current, sub-100 nm resolutions are unlikely to be achieved using conventional ion accelerator systems, (d) in-built optical and fluorescent microscope for sample imaging, identification and positioning, (e) accurate and stable sample manipulation using piezoelectric drivers, and (f) up to 2048x2048 pixel imaging using IONDAQ [49, 50].

3.2.2 General design of the new beam line

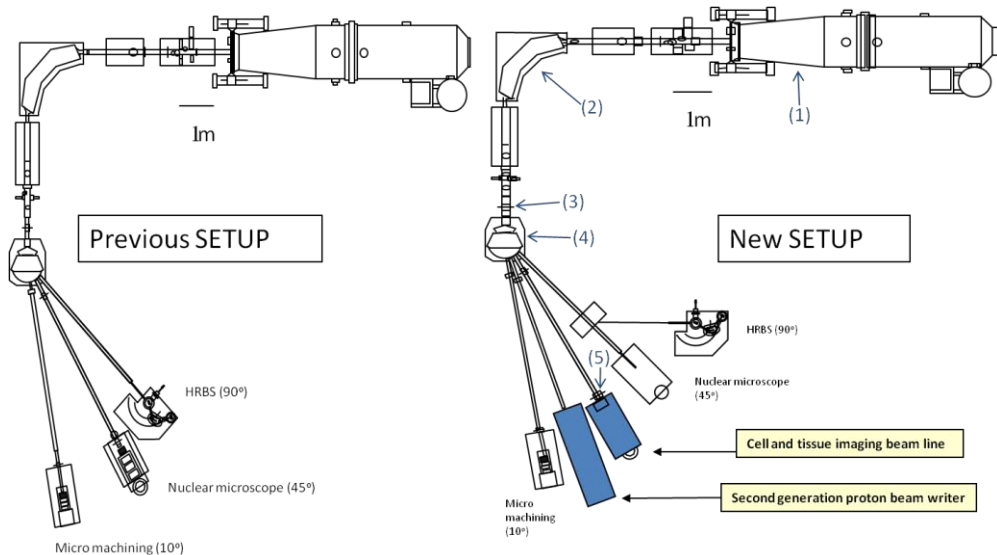


Figure 3.6 A whole view of CIBA ion beam facilities. The left figure shows the previous setup, while the right one includes the newly built two beamlines--next generation proton beam writing facility (in the 20 °position), cell and tissue imaging beam line (in the 30 °position).

As shown in Figure 3.6, the CIBA ion beam facility is based around a 3.5 million volt nuclear accelerator. The previous set-up consisted of 3 advanced

beam line facilities (shown in the left hand figure), and included the prototype proton beam writer (micro machining), the nuclear microscope beam line and the high resolution RBS (HRBS) facility. In the right hand figure, the new cell and tissue imaging beam line is shown at the 30 degree layout position. Another advanced beam line facility at the 20 degree position is also being built up as second generation proton beam writer, in order to further improve proton beam writing technology. The main components of the new set-up are indicated in the right hand figure, and are (1) 3.5 MeV Singltron accelerator with an RF ion source inside, capable of ionizing Hydrogen and Helium gas and accelerating H^+ , H_2^+ and He^+ ; (2) 90 degree analyzing magnet, functioning as an analyzer to select specific beam with reduced energy spread; (3) Object aperture slits to provide an entrance collimator for the probe forming system; (4) Switching Magnet, functioning as a deflector to guide the beam to a specific beam line; and (5) collimator aperture slits in order to reduce beam divergence and therefore the effects of aberrations.

Figure 3.7 shows the schematic design of new cell imaging beam line end station. The object aperture slits and collimator aperture slits are also included in the figure. The beam optical system follows the normal layout of microprobe formation, that of a demagnified image of the beam passing through an object aperture. In our case we use differential micrometer controlled beam apertures (Oxford Microbeams Ltd OM10) both as object apertures and also as downstream collimator slits to control beam aberrations. An electrostatic scanning system is used for beam scanning. An optical fluorescence microscope is situated on top of the vacuum chamber, with a 45 degree reflection mirror and an objective inside the chamber to enable optical

observation of the sample. Transmitted ions, backscattered ions, proton induced fluorescence and secondary electrons can be detected by the various detectors placed inside the vacuum. The signals from these detectors are analyzed and processed by the PC based IONDAQ system developed in CIBA.

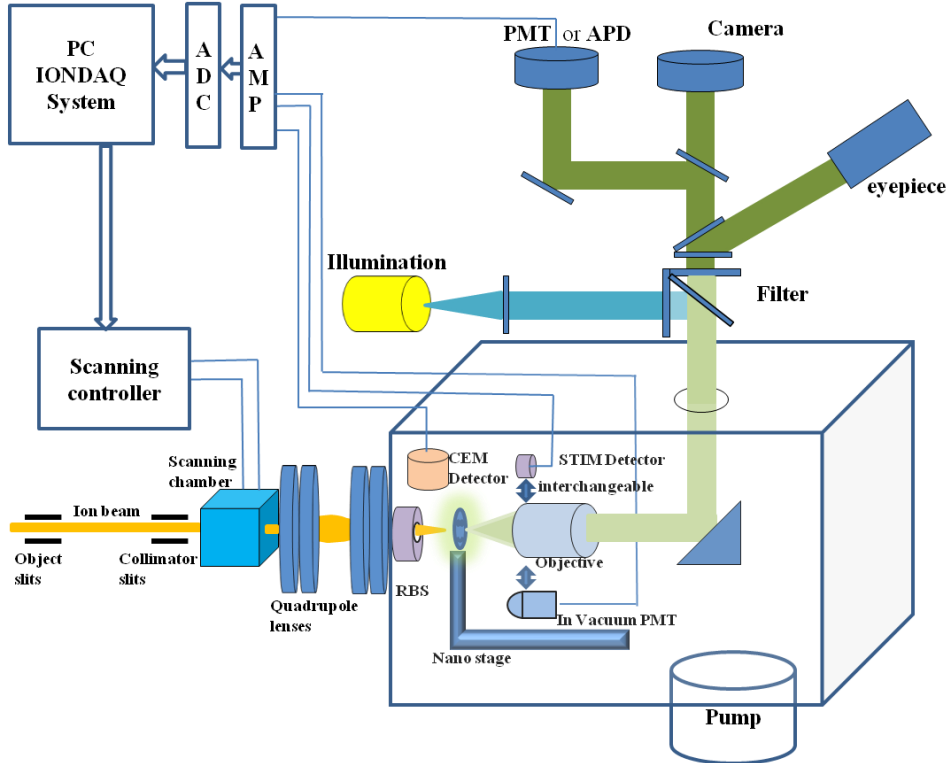


Figure 3.7 Schematic design of the endstation chamber in the new cell and tissue imaging beam line facility.

The layout of the cell imaging facility end stage is shown in Figure 3.8, which indicates from right to left (i) the electrostatic scanning system, (ii) the lens system, made up of 4 compact OM52 quadrupole lenses, and (iii) the target chamber and optical microscope system.

Proton beam scanning is achieved electrostatically, since hysteresis effects are in general less compared with magnetic scanning. A module containing X and Y parallel plates positioned just before the lens system is driven by 2 electrostatic

amps (Trek high voltage amplifiers model 609E6) via IonDaq. The details on electrostatic scanning will be discussed in a later session.

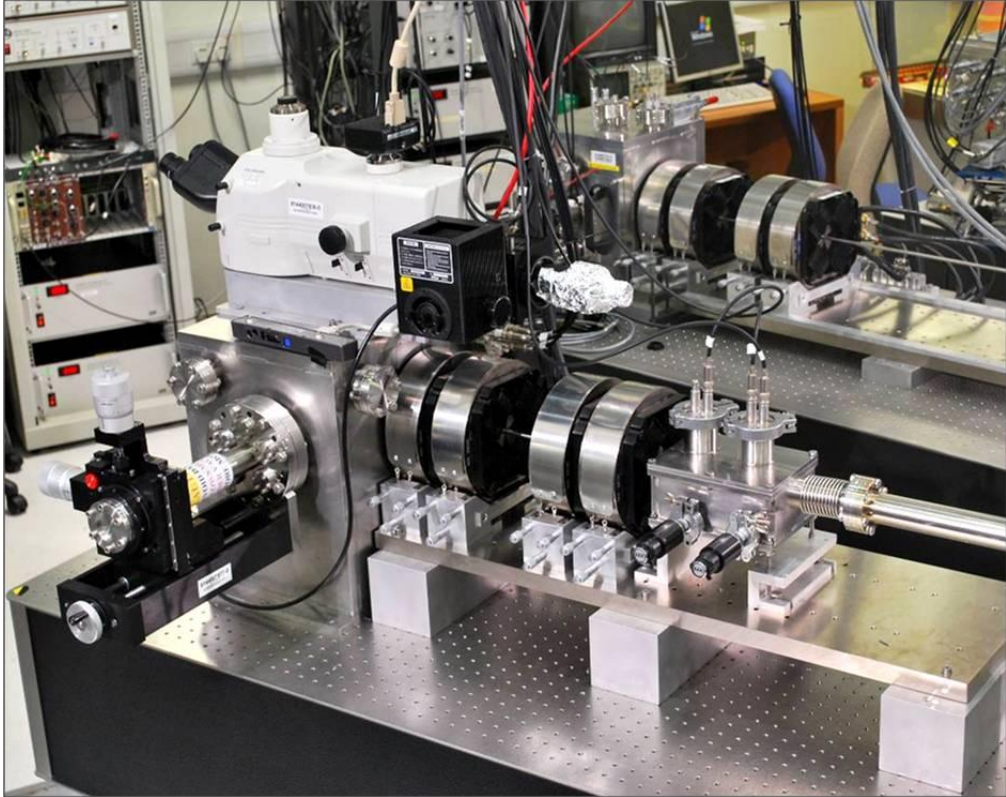


Figure 3.8 Layout of the cell and tissue imaging facility, showing from right to left: the electrostatic scan module, the 4 OM 52 quadrupole lenses, and the target chamber (with the side mounted XYZ stage and the top mounted microscope).

The lens configuration includes a space equal to 1 lens length (in this case 80 mm) between the 1st lens doublet and the second doublet. This enables the following lens configurations to be tested: The single spaced Oxford triplet (using lenses 2, 3 and 4), the double spaced Oxford triplet (using lenses 1, 3 and 4), and the single spaced Russian quadruplet. Note that since the conventional Russian quadruplet has relatively low demagnifications, we intend to use this type of configuration in a single-space double-crossover mode, which has greatly increased demagnifications in both the X and Y directions.

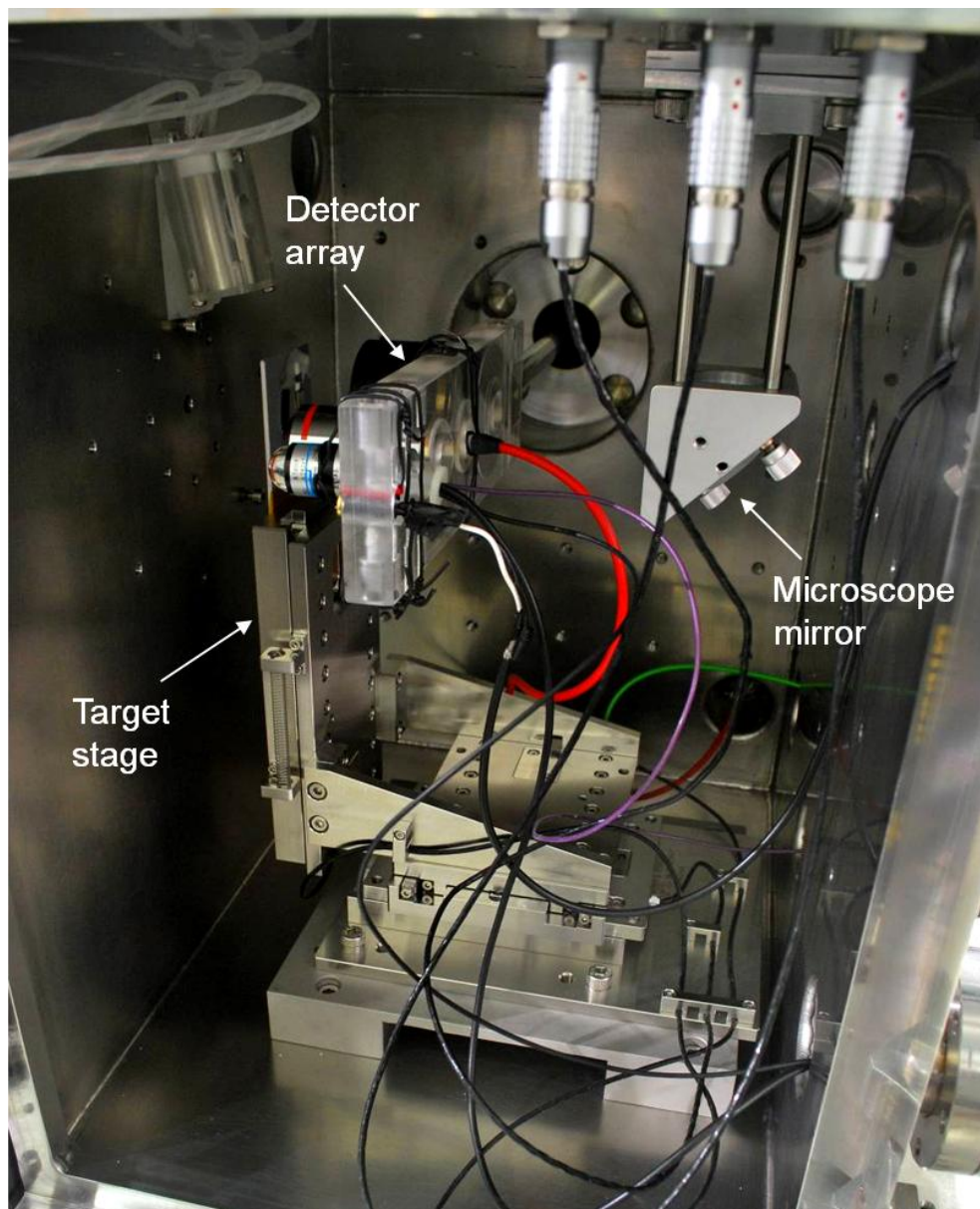


Figure 3.9 Layout of the inside of the target chamber, showing the XYZ target stage, the detector array (which includes a 5X and 15 X objective), and the mirror which transfers the target image into the top mounted microscope.

The inside of the target chamber is shown in Figure 3.9. The chamber houses a piezoelectric XYZ positioning stage (PI N-310K059) controlled by the stage controller: E-861 NEXACT®, and is capable of 25 mm movement in each of the XYZ directions. The positioning stage holds the samples, which also includes a quartz target for optical focusing down to the micron level, and a calibrated grid for fine focusing. Detectors, including a pin diode STIM

detector (Hamamatsu S1223), a conventional surface barrier RBS detector, a annular surface barrier RBS detector, a Hamamatsu photomultiplier (model PMT R7401P), and an objective lenses 5x are mounted on a linear drive behind the target stage. The detectors and optical lenses are moved into place using a manual XYZ translator (model MTS MA1006) connected to the chamber side. A fixed mirror is positioned behind the moveable objective lenses to optically connect the sample image to the microscope (Nikon D-DIH Digital Imaging Head M including filters block and fluorescence illuminator) which is situated on top of the target chamber. The microscope also includes provision for sample illumination and fluorescence imaging.

3.2.3 End Station Target Chamber Housing

As discussed above, in order to enable all the proposed functions, the vacuum chamber should be designed to satisfy the following requirements: (1) enough space for the three dimensional nano stage and various detectors; (2) provision for the target holder to be placed as close to front wall as possible, to enable a small working distance from the lens to the target, thereby increasing the system demagnifications; (3) the chamber should be as compact as possible for fast pumping, the optimal pressure is at the level of 10E-6 mbar; (4) provision for easy attachment of the optical microscope head; (5) various vacuum feedthroughs for electronic communications, XYZ stage control, and detector signal collection, and (6) easy access to the target area for target replacement. Based on these requirements, the chamber is designed as shown in Figure 3.10.

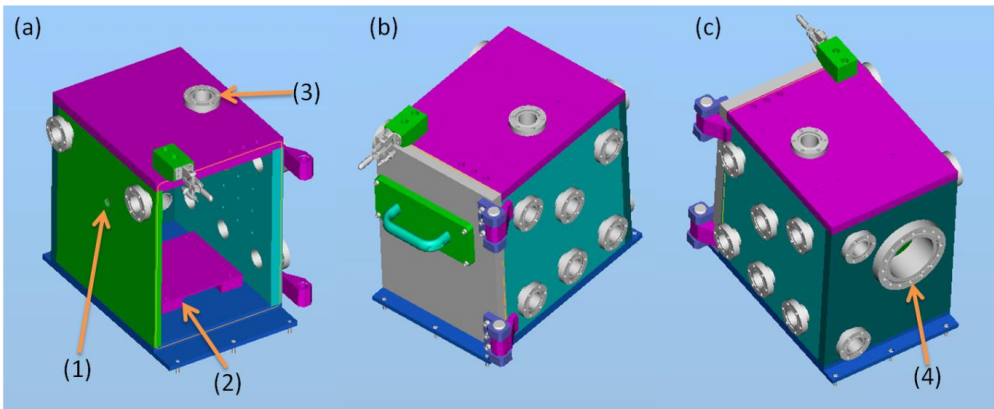


Figure 3.10 Three dimensional views of designed vacuum chamber. In the figure, (1) beam entrance in the front chamber wall; (2) 3D nano stage support, under which there is pumping port; (3) view port feedthrough on the top plate connecting to optical microscope; (4) 6 inch feedthrough for holding the XYZ manual manipulator on the side wall.

Figure 3.11 shows the detailed drawing of the whole chamber. The whole chamber is constructed using stainless steel with a dimension of 395mmx405mmx285mm. All the chamber walls are 25 mm thick except the front wall, which is only 10 mm for reduction of working distance between lens and sample. The left wall of the chamber is a full door. A small door is incorporated into the full door for easy sample exchange. A 6 inch port is included on the right side of the chamber and used to connect the manual XYZ manipulator for detector and objective manipulation. An optical view port (2.75 inch feedthrough) is included on top plate as part of the optical path to the optical microscope. In addition, there are 10 feedthrough ports (2.75 inch diameter) for electronic communications. The pumping port has a diameter of 102 mm, and is situated underneath the stage support on the bottom of the target chamber. A turbo molecular pump (Oerlikon Leybold TURBOVAC MAG W 300P) is used for pumping down the chamber and maintaining the pressure below 10E-5 mbar. The chamber is pre-pumped to 2x10E-1 mbar by a dry pump (BOC Edwards XDS 5). The whole chamber and end station is mounted on to an anti-vibration TMC optical table.

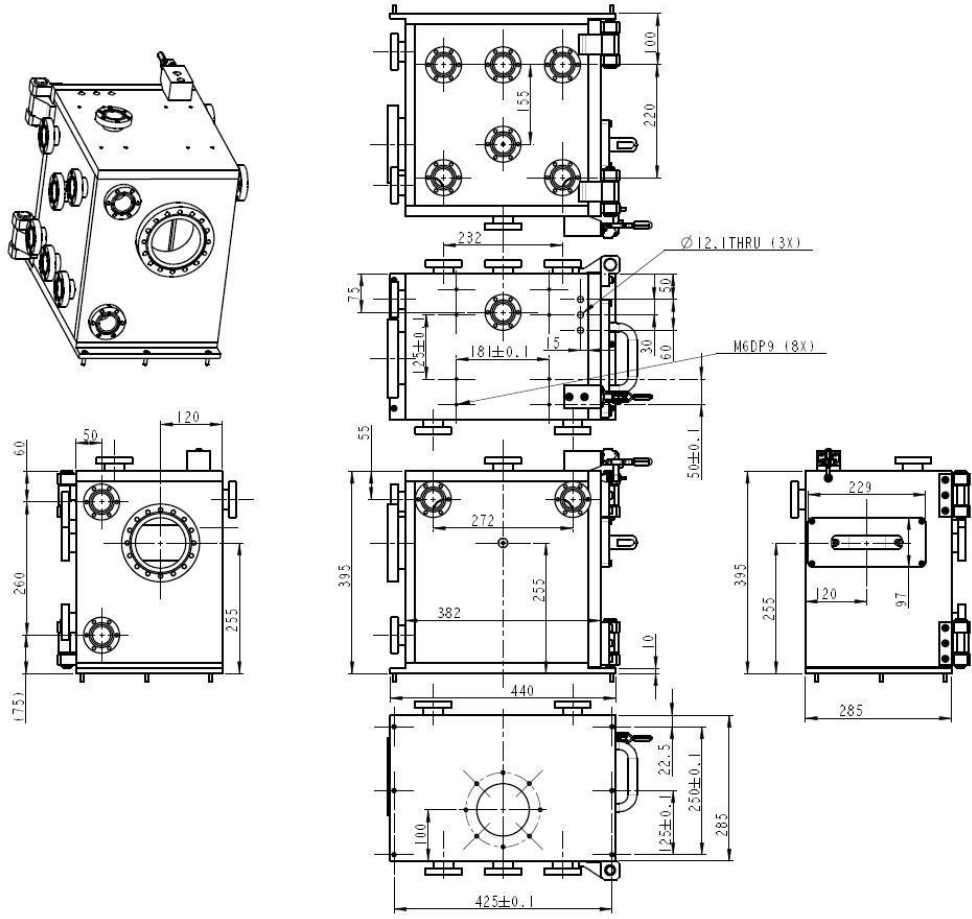


Figure 3.11 The vacuum chamber drawings. The top left is a three dimensional view. The middle drawing is front view of the front chamber wall, on the left, right, top and bottom of the front view are left view, right view, top view and bottom view of the chamber, while the back view is on the top. Unit is in mm.

3.2.4 Scanning Controller Analysis and Design

As discussed before, the beam scanning is realized by electrostatic scanning instead of magnetic scanning in order to reduce hysteresis effects. Figure 3.12 shows the basic principle of electrostatic scanning. Two parallel copper plates, insulated so as to support high voltages, can generate an electrical field which will control the beam scanning in one direction. If two more parallel copper plates are placed in orthogonal directions, then a raster beam scanning can be easily realized in two directions. The rotational alignment of the parallel plates

can be precisely adjusted outside the scanning chamber by a micrometer screw to ensure the orthogonality between the X and Y scanning.

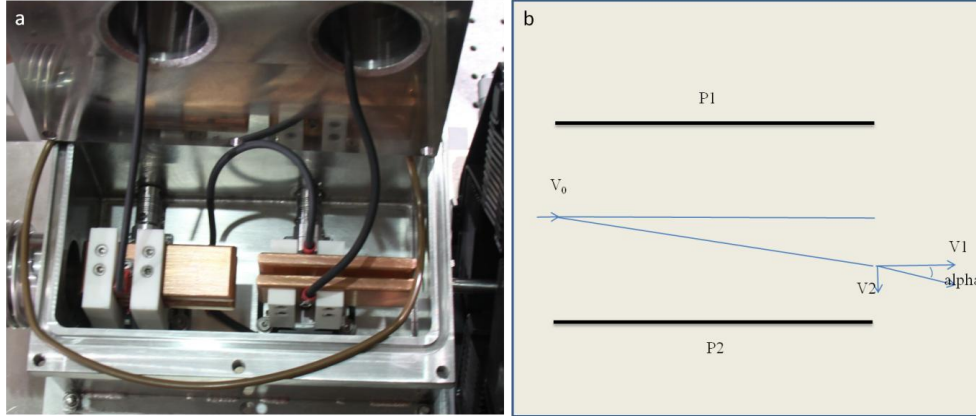


Figure 3.12 Scanning plates and the effect caused on the beam going through the plates.

The calculation of the required scanning voltages to achieve a particular x or y deflection at the target is as follows: If the designed plate length is denoted by 'L'; the distance between two plates is 'd'; ' E_0 ' is the beam energy; ' v_0 ' is the particle velocity before entering the scanning field; ' v_1 ' and ' v_2 ' are the velocity components in beam trajectory Z and vertical direction Y; 'm' is the particle mass; 'U' is the applied voltage; 'F' is the force caused by electrical field; 'a' is the acceleration; 'q' is the charge of the particle; then 'alpha' is the particle exit angle with respect to the Z axis.

$$\left. \begin{aligned} 1/2mv_0^2 &= E_0 \\ v_0t &= L \\ a &= \frac{F}{m} = \frac{Uq}{dm} \end{aligned} \right\} \Rightarrow t = \frac{mv_0L}{2E_0} \right\} \Rightarrow v_2 = at = \frac{UqLv_0}{2dE_0} \Rightarrow \tan(\text{alpha}) = \frac{v_2}{v_1} = \frac{v_2}{v_0} = \frac{UqL}{2dE_0}$$

Eq3.16

If ' Z_{op} ' is the distance between object aperture to the plates, then the scanning induced deflection can correspond to a virtual translation ' h_o ' in the target plane as follows:

$$h_o = Z_{op} \times \tan(\alpha) = \frac{UqL}{2dE_0} Z_{op} \quad \text{Eq3.17}$$

Therefore, if ' D_y ' is the demagnification in Y direction, the scanning induced deflection will cause a scanning translation ' h_i ' in the image plane in Y direction.

$$h_{iy} = \frac{h_o}{D_y} = \frac{UqL}{2dE_0 D_y} Z_{op} \quad \text{Eq3.18a}$$

Similarly, the calculation can be applied to X direction,

$$h_{ix} = \frac{h_o}{D_x} = \frac{UqL}{2dE_0 D_x} Z_{op} \quad \text{Eq3.18b}$$

(1) From Eq3.18a and Eq3.18b, if we want to get the same scan size in X and Y direction for a specific beam, then the ratio of the voltage applied to each direction should be proportional to the demagnification ratio as shown in Eq3.19.

$$\frac{U_x}{U_y} = \frac{D_x}{D_y} \quad \text{Eq3.19}$$

(2) For a specific lens configuration system, L, d, D and Z_{op} are fixed, therefore Eq3.18 can be simplified as:

$$h_i = C \frac{Uq}{E_0} \quad \text{Eq3.20}$$

C is constant in Eq3.20. For the beam we normally use protons, H_2^+ or He^+ . If we wish to use a common scan size, then the voltage applied to the plates is proportional to the beam energy.

(3) Based on practical considerations and related calculations as described above, d and L have been designed to be 4mm and 70 mm respectively.

Table 3-5 Scanning voltage calculation for typical beam energy and scan size. Calculation is based on single spaced triplet lenses configuration and beam optics parameter in Table 3-4.

Beam (H^+ or He^+)	Scan size (um)	Voltage required for the scanning plates	
		X (V)	Y(V)
2 MeV	10	204	34
	50	1006	165
	100	2042	335
	150	3048	500
	200	4084	670
1.5 MeV	10	152	25
	50	761	125
	100	1524	250
	150	2286	375
	200	3048	500
1 MeV	10	101	16.5
	50	503	82.5
	100	1006	165
	150	1524	250
	200	2042	335

Z_{op} is 6.46 m in the new cell imaging beam line. Considering the parameters in Table 3-4, demagnification in x and y directions are 573 and 94 respectively. Based on Eq3.18a and Eq3.18b, the voltage required in X and Y plates for typical beam energy and scan size can be calculated, and are shown in Table 3-5. All these calculated results are in agreement with experimental scanning parameters. As shown in Table 3-5, for 2 MeV proton beam, the voltage

required for 100 um raster scanning in X and Y direction are 2042 volts and 335 volts. In order to realize such scanning voltages, voltage amplifiers (Trek high voltage amplifiers model 609E6) with an amplification of 1000 are used. The signals driving the high voltage amplifiers are determined by the OMDAQ system. For relatively large scan sizes of 100 microns, the TREK high voltage amplifiers are ideal. However, for smaller scans (eg 10microns at 1012x1012 pixels ie 10nm per pixel) then the noise levels from the TREK amplifiers may be detrimental to the ultimate resolutions since the noise levels are in general greater than the pixel step size. For smaller scans therefore, high precision industrial amplifiers (AE Techron 7224 DC-Enabled AC Amplifier) with an amplification of 160 are used.

3.2.5 Scanning clipping analysis

As well as determining the voltages required for specific scan sizes, there is a limitation on the total scan size from clipping of the beam path as it passes through the quadrupole lenses. In this section, we calculate the maximum scan size possible before clipping becomes the limiting factor.

The calculations are based on a single spaced triplet lens system with a space of 80mm and working distance of 30 mm, which gives demagnifications of 574 and 93 in the X and Y directions. The analysis is for 2 MeV protons with momentum spread of 0.001%. Detailed parameters have been shown in Table 3-4. The system was stigmatized first using the Transport module in PBO.

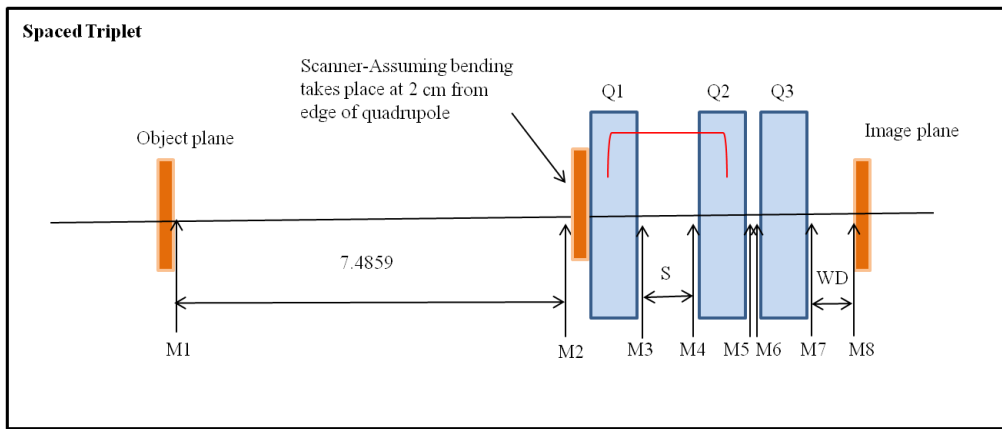


Figure 3.13 Figure for beam scanning analysis. M1 to M8 are Markers put in PBO program for beam extent monitor.

In figure 3.13, the extent of the beam envelope is monitored at the markers (M1, M2 to M8) using the Turtle module in the PBO program. In order to keep the beam spot at the target the same size in both directions, the object aperture is set at 10 by 2 um. Similarly, for the scanning, the voltage applied to X and Y plates are also different such that the scanning divergence angles for X and Y are set according to the ratio of D_x and D_y . From the analysis at all the markers, the beam extent is always biggest at M6 for X and M4 for Y. For beam clipping analysis therefore we only consider these two points. Furthermore, in a typical square raster scan, the X direction is always the first to exhibit beam clipping because of its large scanning divergence angle. We therefore only consider the X direction for beam clipping analysis.

Table 3-6 shows the envelope beam extent and astigmatism coefficients simulated using the beam parameters in Table 3-4. Both $\langle x|\theta \rangle$ and $\langle y|\varphi \rangle$ increase as the scanning angles increase. As a result, stigmatism is affected by the scanning angles. If the tolerance of astigmatism coefficients for stigmatism is 0.01, then the beam can only be kept focused for a scan below around 80 μm for 2 MeV protons.

Table 3-6 Beam extent and astigmatism coefficients for different scan size based on 2 MeV proton.

Square Scan Size (μm)	Half Scan		Astigmatism Coefficients		Max Half Beam Extent (mm)	
	X	Y	$\langle x \theta \rangle$	$\langle y \varphi \rangle$	X in M6	Y in M4
20	0.77	0.125	0.0006	-0.00079	0.174	0.063
80	3.08	0.5	0.00954	-0.01157	0.573	0.162
120	4.6	0.75	0.02153	-0.02803	0.834	0.227
160	6.115	1.005	0.03807	-0.04954	1.09	0.294
200	7.645	1.26	0.05951	-0.07751	1.35	0.356
240	9.6	1.48	0.09369	-0.12088	1.64	0.424

In our system, the outside diameter of the beam pipe passing through the quadrupole bore is 6 mm. Assuming the wall thickness is 0.8 mm, then the beam is clipped if the beam envelope in one direction goes beyond 2.2 mm from the beam axis. The beam envelope in the X direction always has its largest extent in Quadrupole 3, which is in between the markers M6 and M7 which unfortunately cannot be monitored using the Turtle module in the PBO program. We have therefore used a reduced value of 1.6mm for the maximum axial displacement, to account for this limitation. As shown in Table 3-6, scanning up to a square of 240 μm are within the clipping range. For scan size larger than 240 μm , then the beam will begin to suffer clipping in the X direction.

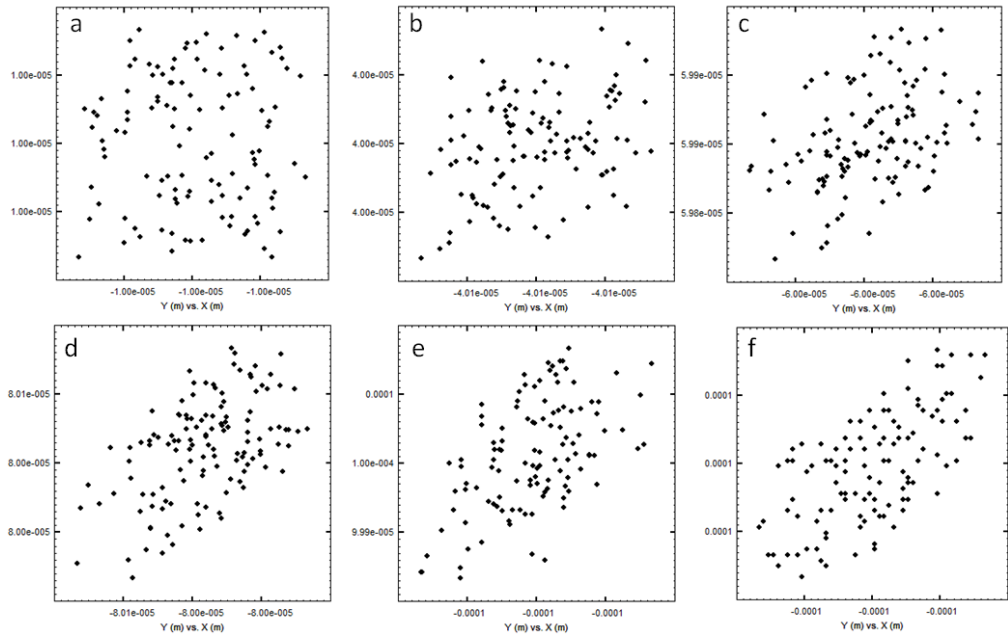


Figure 3.14 Final beam plots for different scan sizes based on parameters shown in **Table 3-4**. (a) 20 μm , (b) 80 μm , (c) 120 μm , (d) 160 μm , (e) 200 μm , (f) 240 μm .

We have also briefly considered the deterioration in the final beam spot size due to off axis aberrations introduced as the beam is deflected away from the central axis. As shown in Figure 3.14, beam shapes in figure a and b are in a relatively nice square, while, for figure c, d, e and f, the beam becomes significantly stretched and the beam spot increases in size twice or even more from the original 20 nm. If we take into account beam stigmatisation, beam envelope clipping and off axis scanning aberrations, then an optimum size for good quality beam scanning at high resolution for 2 MeV protons is around 80 μm . However, this is adequate for high resolution whole cell scanning, since most cells are less than 80 microns in extent.

3.3 Alignment of the Whole Beam Line Facility

Probe-forming lens systems will only achieve optimum performance if careful attention is paid to the accurate alignment of each lens in the system. In this section, the alignment procedures will be discussed.

3.3.1 Mechanical alignment during beam line assembly

The first step is to ensure that the beam line itself is optically aligned. This was accomplished by a theodolite with a precision of sub-millimeter. As Figure 3.6 shows, the object slits and switching magnet have been shared with all the other previous beam lines for many years, which indicates they are well aligned with the beam. The straight through beam line aligned with the switching magnet and object aperture forms the zero degree reference. Based on this reference, the 30 degree axis can be easily and precisely determined both horizontally and vertically. With the location of this axis, the microprobe components can be optically aligned to this axis using the theodolite.

All the parts in the endstage are designed to be located on the same axis. However there are several key components which require extra attention in their mechanical alignment. Firstly, the beam apertures should be aligned with extra precision. Both object and collimator slits use polished tungsten carbide roller bearings as the defining edges (Oxford Microbeam Ltd) and have a maximum aperture opening of 5 mm, controlled manually by differential micrometers. Even though there is spatial flexibility built into the aperture positioning via the micrometers, it is still important to have the centre of the aperture aligned with the beam line to avoid off axis object aberrations. Since each aperture housing is linked with the beam line using flexible bellows, this coarse adjustment is relatively easy. Secondly, the scanning

plates need to be aligned in the centre with high precision, since the distance between the two plates is 4 mm. Thirdly, the beam entrance hole in the target chamber front wall needs to be well aligned to ensure the small beam pipe connecting the scanning chamber to target chamber is on the optical axis. Finally the quadrupole lenses should be optically aligned as precisely as possible with the optical axis, although as we will see below, the final more sensitive alignment is carried out by using the beam itself to determine the beam axis. The beam axis does not necessarily coincide with the optical axis.

3.3.2 Optical alignment of the microscope

As shown in Figure 3.7, the target chamber incorporates an optical fluorescence microscope (Nikon D-DIH Digital Imaging Head). The optical microscope is aligned so as to view the target area scanned by the beam. This initially is assumed to correspond to the central axis of the beam entrance port in the front face of the target chamber..

(1) Illumination lamp alignment. The microscope is optically connected via an objective lens and 45 degree mirror. Lamp alignment can be easily carried out by viewing a blank paper target positioned in the focal plane, while adjusting the lamp alignment screw and lamp lens, until the lamp filament images merge together to form a uniformly illuminated area in the center.

(2) Mirror alignment. As shown in Figure 3.7, a 45 degree mirror is used to reflect the light from the target into the microscope. To align the mirror, an alignment laser which can be slotted into the microscope eyepiece, is used. The laser light is transmitted through the microscope and the 45 degree mirror on to a mirror positioned at the target plane.

The light is then reflected back into the microscope, and the position of the mirror adjusted until the reflected laser spot coincides with the emitting laser



Figure 3.15 Alignment laser for optical mirror alignment. The laser can sit in the eyepiece or the microscope camera port.

(3) Objective lens alignment. If we move the objective lens slightly along the optical path, the broad circle of light can be focused to a smaller spot. By moving the objective lens horizontally or vertically, the beam spot can be moved to coincide with the centre of the beam entrance port. During normal operation however, the particle beam does not necessarily coincide with the centre of the beam entrance port. In this case, we can view the fluorescence the beam makes on a glass target, and adjust the objective lens to the focal point on the beam axis.

3.3.3 Alignment using the beam as an alignment tool.

(1) **Defining the beam axis.** Because of the effect of stray magnetic fields on the beam, and also because the magnetic centre of each lens does not necessarily coincide with its mechanical centre, the path of the beam will be close to, but usually not lie along the surveyed optical axis. The true axis of the system is therefore defined to be the path of a charged particle which passes through the centre of the object slits to the centre of the field of view of the microscope. The next task is to set the collimator slits onto this axis, so that an axial pencil of rays may be defined. This is done by allowing the beam to pass through the system with both the object and collimator slits fairly wide open and the quadrupoles turned off. The beam is observed as a fluorescence area on thin quartz at the target position. By moving in each of the collimator slit jaws in turn, the position can be found at which the shadow of the slit jaw passes through the centre of the field of view of the microscope. These positions are noted as the central positions of the collimator slits.

(2) **Aligning the quadrupole lenses to the beam axis.** By reducing both sets of slits about their central positions, a narrow axial beam can be defined, and the quadrupole lenses can be aligned so that their magnetic axes coincide with the defined beam axis. This is done by exciting each quadrupole in turn as a singlet lens, thereby forming a line focus on a glass target positioned in the target plane. In general, if the quadrupole lens is not aligned, there will be a dipole steering effect on the beam: In this case the line focus on the glass target will not be aligned with the centre of the field of view of the microscope, ie the

defined beam axis. By adjusting the quadrupole lens in a direction perpendicular to the line focus, the line can be steered to coincide with the defined beam axis. In this case the dipole steering is zero and the lens is aligned in the direction perpendicular to the line focus. By reversing the excitation of the lens, the adjustment can be carried out in the other direction. All lenses can be independently aligned by repeating this procedure.

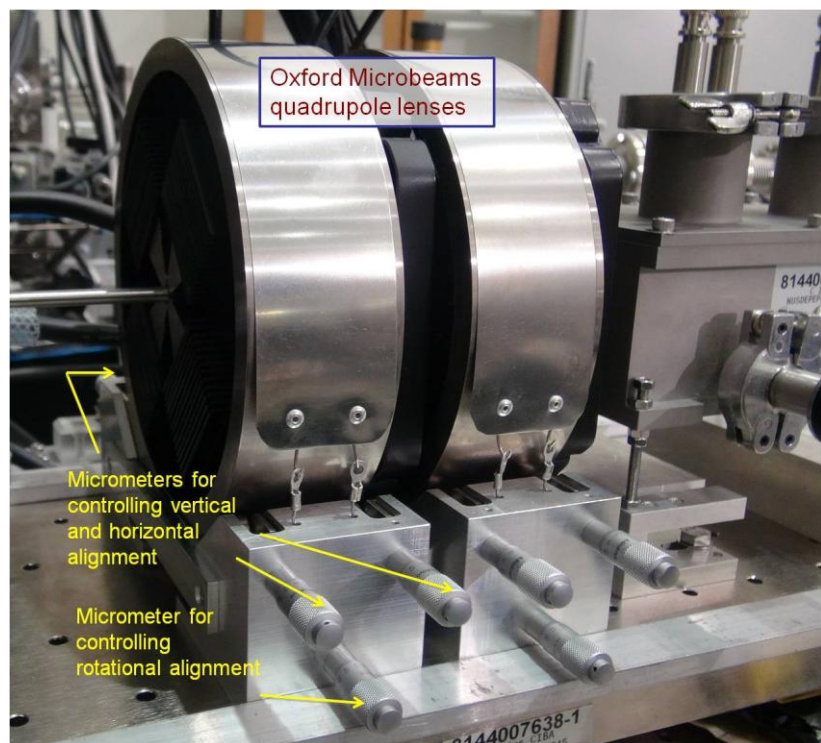


Figure 3.16 Oxford Microbeams quadrupole lenses. Micrometers for controlling vertical and horizontal alignment are shown in the figure as the top two, the other two are in other side. The bottom micrometer is to control the rotational alignment.

(3) Adjusting the rotational alignment. The quadrupoles can now be rotationally aligned with respect to each other. This is done for each individual lens by making sure that the line focus for each lens does not exhibit any vertical or horizontal tilt in the image plane. Further fine tuning of the rotational alignment can be carried out by exciting

two of the lenses as a doublet, thereby forming a focused spot on the glass target. By adjusting the excitation of the lenses, a rectangle of illumination is seen; this collapses to a point and expands again as the focus is passed. If, however, there is any rotational misalignment, we can see a tilted rectangle which appears to rotate as the focus is passed. By adjusting the rotation of the lens to be aligned (as shown in Figure 3.16), this effect can be minimized. The same procedure is carried out for each of the lenses in the system, using one common lens as a reference.

We can now connect the 3 aligned lenses in the spaced Oxford Triplet configuration, in other words the first 2 lenses are connected to one power supply, and the 3rd lens is connected to the second supply. By increasing the currents to the lens, a point focus as imaged by the beam fluorescing on the glass target can be achieved. Focusing down to around 1 micron can be achieved by visually minimizing the beam spot image. For achieving smaller beam spots, usually with smaller beam currents, scanning the beam over a metal grid calibration target is required; this is discussed in the next sections.

3.4 Brief description of IONDAQ data acquisition system

IonDAQ is the new PC based DAS of CIBA, at National University of Singapore. At its heart is a Xilinx Virtex-II 3 Million gate Field Programmable Gate Array (FPGA) controlling core (CORE) that works together with rack mounted ADCs and a high level host programme (HOST) that allows the user to interact with CORE. This FPGA CORE resides on a compact National Instruments PCI computer card (NI PCI-7833R) that also contains 96 DIO

(digital input/output), 8 DAC (digital to analog convertors) and 8 AI (simple onboard ADCs). The DIO lines are TTL compatible, the DACs support output rates of 1 MHz (1 μ s conversion time) and the AIs have a conversion time of 5 μ s [49]. Figure 3.17 shows a schematic of IonDAQ and its CORE. Each of the loops shown in the image of the CORE represents a process that can run independently.

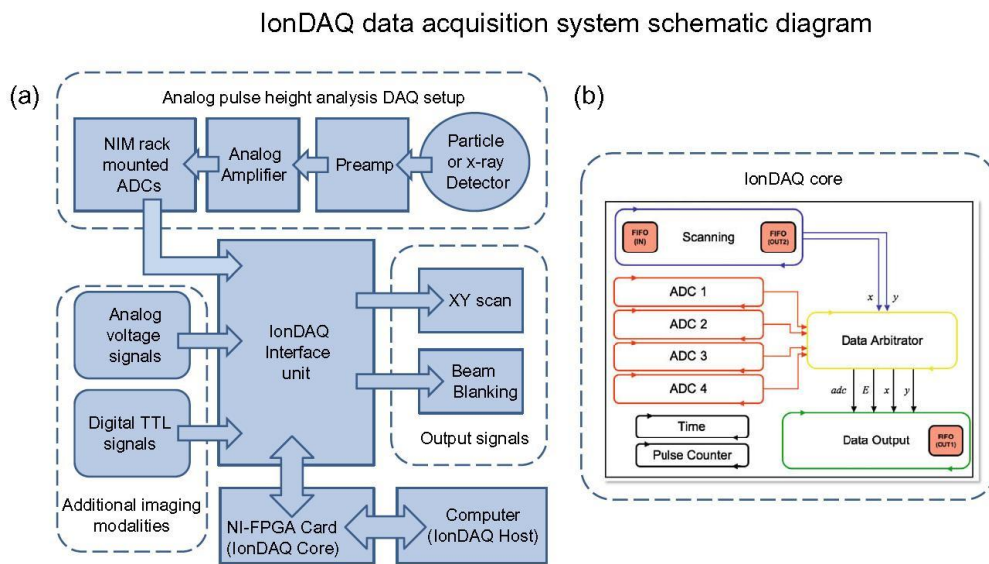


Figure 3.17 (a) Schematic showing IonDAQ system. (b) Schematic diagram of the functionality of the CORE component of IonDAQ. Reproduced from ref [49].

Table 3-7 shows all the features supported by IonDAQ. The IonDAQ data acquisition system supports several imaging methods that can be used concurrently. Up to four NIM rack mounted ADCs can be used to simultaneously image signals and perform pulse height analysis (PHA) from a variety of traditional ion beam analysis detectors. The user can add sorts to these ADCs and the data can be acquired in listmode for post acquisition playback and processing. Two fast pulse imaging (FPI) inputs are provided on the IonDAQ interface box. These utilize DIO lines on the FPGA card and

allow the user to spatially map using detectors that have a TTL pulse output. This imaging mode is useful for pulsed signals that do not carry any energy information such as signals from photomultiplier tubes and channel electron multipliers. Since there is no analogue to digital conversion performed, FPI can be effectively used to image signals that have high count rates with minimal deadtime. Besides, two further inputs are provided on the IonDAQ interface box that enable the user to perform analogue imaging (AI). This imaging method is useful for imaging detectors such as photomultiplier tubes configured in voltage output mode.

Pixel Normalization is an added function but quite important to mention here. Instead of dwelling at each pixel for the same period of time to collect the data, Pixel Normalization controls the beam scan rate so as to make the beam stay in one pixel until the system collects a certain number of particles or signal counts. In other words, each image contains the same number of particles or counts for each pixel, instead of the same dwelling time in conventional scanning. For STIM, where all the particles pass through the sample and are collected by a detector positioned behind the target, this method removes statistical fluctuations in the final image and improves contrast. Pixel normalization also removes the effects of beam fluctuations, which would otherwise create intensity fluctuations in the final STIM image.

Table 3-7 Features supported by IonDAQ. Reproduced from ref [49].

Main <i>IonDAQ</i> features	
Scanning	
Pixel resolution	$256^2, 512^2, 1024^2, 2048^2$
Scan polarity	Bipolar or unipolar
Scan voltage	User defined [0– ± 10 V] with variable aspect ratio and direction (Software)
Beam blanking	User defined [0–10 V]
Pixel dwell time	1 µs (PHA, FPI), 5 µs (AI)
Scan modes	Point, Line, Raster, Interlaced, Triangle, User defined, File (EPL), Beam Monitor
ADCs	
NIM ADC modules	Support for FastComTec, Ortec, Canberra
DAQ	TQSA or Listmode operation with sorts
Mapping and imaging	
NIM ADCs (PHA) imaging	Digital interface (4 channels)
Analogue imaging (AI)	Voltage signals [0–10 V] (16 bit), Point, Line and Frame averaging (2 channels)
Fast pulse imaging (FPI)	TTL signals (2 channels)
Deadtime	Mapping and correction
Mapping features	Median and mean maps. Real time user defined colour bar analysis. Digital magnification of selected regions
Data collection and processing	
DAQ presets	Frames, Time, Total Counts, ADC Counts, Counter, Charge
Data transfer	FPGA core and CPU via DMA
Data rates	In excess of 100 kHz with NIM ADCs, higher rates for FPI
Batch mode DAQ	Multiple samples by specifying position and a preset (requires motorized stage)
Other	
Motorized XYZ stage	Current support for EXFO Burleigh inchworm stage

3.5 Beam Test, Performance Analysis and Discussions

3.5.1 Resolution Standard

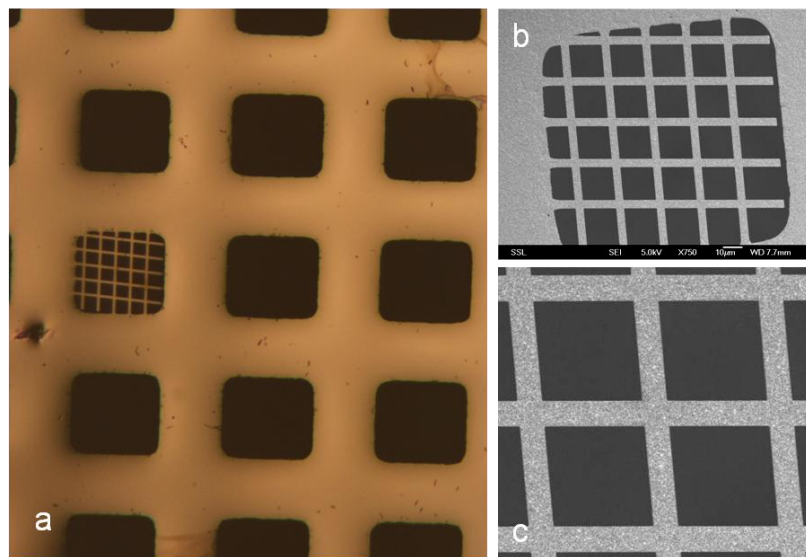


Figure 3.18 Nickel grid resolution standard. Figure a shows the optical micrograph of the grid; Figure b and figure c is the electron micrograph of the small grid area in figure a.

Resolution tests of the new beam line (in the single spaced Oxford triplet mode) were undertaken using a calibration grid fabricated using proton beam writing in CIBA. Optical photographs and SEM scans of the Ni grid are shown in Figure 3.18. The grid, which exhibits sharp sidewall edges has grid bar dimensions of 4 micron, and a nominal thickness of 2 microns.

3.5.2 Beam focusing

A 1.7 MeV Helium ion beam was focused down as a performance test for the new cell imaging beam line. The beam focusing procedures are discussed here.

- (1) **Optimizing the beam.** Using relatively large aperture settings for the object and collimator slits, the beam current as measured in the target chamber is optimized by varying selected accelerator parameters. The next step is to adjust the object slits to make sure the beam is going

through the center of object aperture and is shaped by the aperture in all directions. This can be carried out by moving the object aperture to find the position of maximum transmitted beam current and then cutting the beam to a current of around 100 pA. Then, by viewing the transmitted beam current on a glass slide at the target position, we can adjust the quadrupole currents and focus the beam down to a point. When focusing the beam it may steer from its central position, which means that the beam trajectory does not correspond to the magnetic axis of the lens system. If the system has already been well aligned, then the problem is usually that the collimator slits are not centrally positioned, forcing the trajectory of the beam away from the magnetic axes of the lenses. This effect can be remedied by quite simply re-adjusting the collimator slit positions until the focused beam spot does not steer.

(2) **Focusing the beam on quartz.** After axially aligning the collimator aperture with the magnetic axes of the quadrupole lenses a point focus can easily be obtained by adjusting the lens currents and viewing the glass slide using the microscope. It is convenient to make sure that the beam spot image corresponds to the centre of the microscope field of view. This can be achieved by adjusting the position of the objective lens, and is useful when we scan a selected target at a later time, because we can then use the microscope position to determine where the beam spot is located. Using visual imaging of the beam spot , we can optimize the beam spot down to around 1 micron.

(3) Focusing the beam to sub-micron spot sizes using a nickel calibration grid.

The next step is to move the calibration grid to the beam position and focus the beam by finely adjusting the quadrupole lens current while raster scanning the beam over the grid.. Transmitted ions are collected to form a square image of the grid. By placing the particle detector in an off-axis position, the particles scattered by the grid bars will be collected to form an image of the grid bars. If we place the detector directly on axis, the detector then collects all the directly transmitted particles, and this produces two different peaks in the transmitted particle energy spectrum. The higher energy peak is from the particles that have passed between the grid bars, and have suffered no energy loss, and the other lower energy peak is caused by the particles that have penetrated the grid bar and lost energy. By creating two images by sorting the data from the 2 energy windows, a grid bar image and an image depicting the areas between the grid bars can be formed. If we assume that the cross-section of the beam particle beam can be approximated to a Gaussian profile, as the beam spot becomes smaller, the grid bar edge will be sharper in the image.

Focusing on the grid can be divided into two steps. First, by setting the object slits to a small aperture size eg 10x2 um (which is the typical setting for a 20 nm geometrical beam spot size since the demagnification in x and y are around 500 and 100) while leaving the collimator slits relatively wide open 250x250 um, then we can try to adjust the quadrupole lens current until we obtain the sharpest edge image using off axis STIM. In this case, because the collimator

aperture is relatively wide, the spot size will be heavily aberrated. When it is difficult to improve the sharpness of the image any further by adjusting the quadrupole currents, this means that the system is stigmatic. Next, by closing down the collimator aperture to around 40X20 (keeping Y aperture smaller since the aberrations coefficients in Y directions are 2-4 times higher than X), the effect caused from aberrations will mostly be reduced and the image will be much sharper. Finally, we can slightly adjust the X and Y lens current to get the best grid image.

(4) **Using the focused beam for cell scanning.** Assuming we have achieved the best spot size possible, the next step is to use this focused beam for sample imaging and analysis. As long as the sample is located in the plane of the grid, the beam will remain highly focused and no depth of focus problems will occur. Since the grid is in the focal plane for both optical microscope and the quadrupole lens system, as long as we keep the objective lens fixed and move the sample using the nano-stage to the beam position as determined by the center of optical field of view, then we can use the focused particle beam for high resolution sample imaging and analysis. If, when we move the sample to the centre of the optical field of view, the optical image is not in focus, then by readjusting the z-position of the nanostage the sample can be brought back into the focal plane of the optical system and particle beam.

3.5.3 Beam Test Results

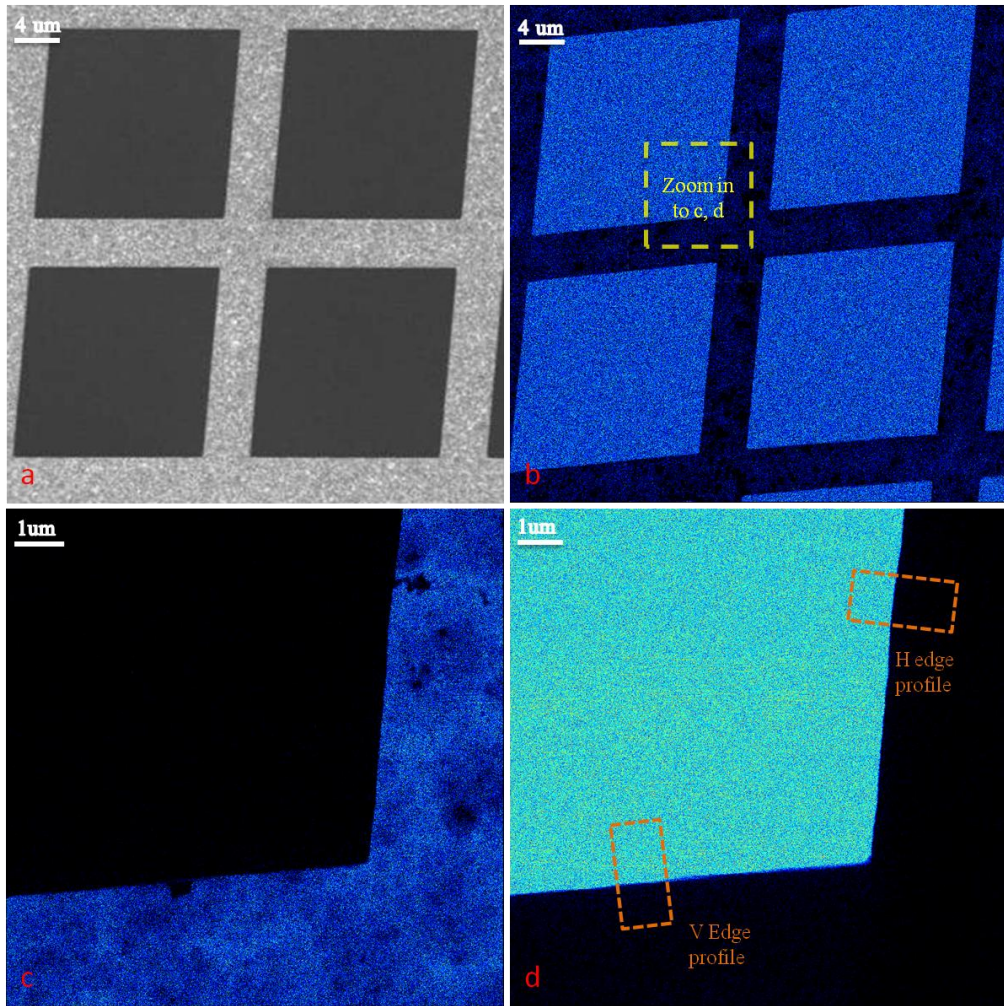


Figure 3.19 Grid image for beam performance test using 1.7 MeV helium ions. Figure a shows SEM image of a grid area; Figure b shows direct on axis STIM image of the same area; Figure c and d show 10 um direct STIM image of the area selected in the yellow square in figure b. In figure d, edge profile data are extracted from the two rectangular areas for beam spot size analysis in horizontal and vertical directions.

Figure 3.19 a and b show SEM image and direct STIM image of the same grid area. Figure 3.19 c and d show 10 um direct STIM image of the area selected in figure b. Figure c and d are sorted from the two different peaks in the energy spectrum, which represent the particles penetrating grid bar and passing through the grid bar gaps respectively. Quite interestingly, several structures with the size around 100nm to 500 nm can be clearly showed in figure c. This indicates the potential of the focused beam for imaging cells,

since many organelles are in this size range. The beam current in this case was approximately 10,000 particles per second.

3.5.2 Beam spot size analysis

It is always necessary to be able to have a quantitative measurement of the beam spot size. The particle distribution within the beam spot is typically assumed to be a Gaussian distribution, which has been confirmed by experimental observations. The formula shown in Eq3.21 exhibits the mathematical correlation between the signal intensity and the FWHM of the beam spot based on previous mathematical analysis [51].

$$F(x) = \frac{1}{2} [1 + Erf(\frac{2\sqrt{\ln 2}}{f}(a - x))] \quad \text{Eq3.21}$$

Eq3.21 can be used to describe the shape of line scan produced with signals such as RBS, PIXE or STIM, by scanning the beam over a sharp edge. In the function, f is the FWHM of the beam spot in the direction orthogonal to the scan direction, and a is the position of the edge along the X axis. The beam scan scenario is shown in Figure 3.20. Note that the above function is in a form where it has been normalized to unity. Note that

$$F(x) = [0,1] \quad \text{for } x \in R$$

And

$$\begin{aligned} F(a - \frac{1}{2}f) &= \frac{1}{2} [1 + Erf(\sqrt{\ln 2})] \approx 0.88 \\ F(a + \frac{1}{2}f) &= \frac{1}{2} [1 - Erf(\sqrt{\ln 2})] \approx 0.12 \end{aligned}$$

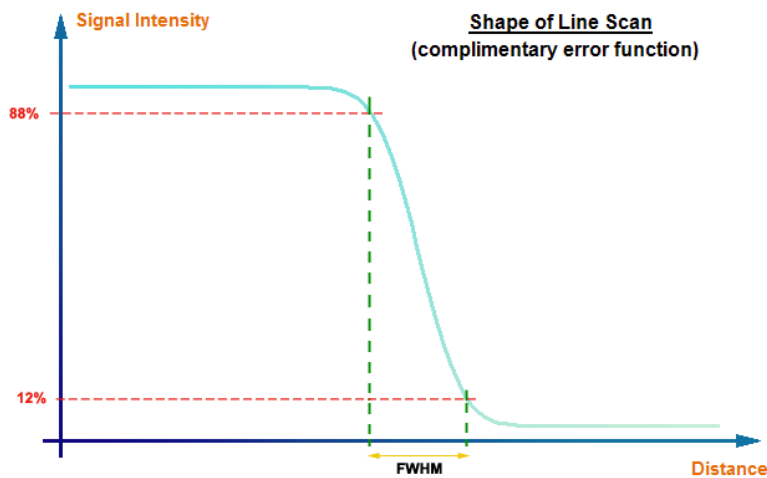
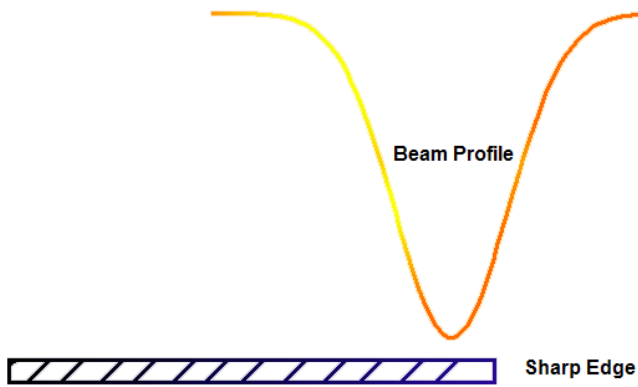


Figure 3.20 Shape of the line scan in scanning a Gaussian profile over a sharp edge. The above shape is obtained with signals such as RBS, PIXE and STIM.

Thus, we may gauge the value of f by measuring the distance between the points where the line scan intensity is 88% and 12% of the maximum. The exact calculation of FWHM can be carried out by fitting the formula with experimental line profile data. The line profile data of rectangular areas labeled as ‘H edge profile’ and ‘V edge profile’ in Figure 3.19d has been extracted. Based on Eq3.21 and the experimental data, the fitted FWHM (in Matlab) for the results in Figure 3.19 is 19.5 nm in Horizontal and 25 nm in Vertical directions as shown in Figure 3.21.

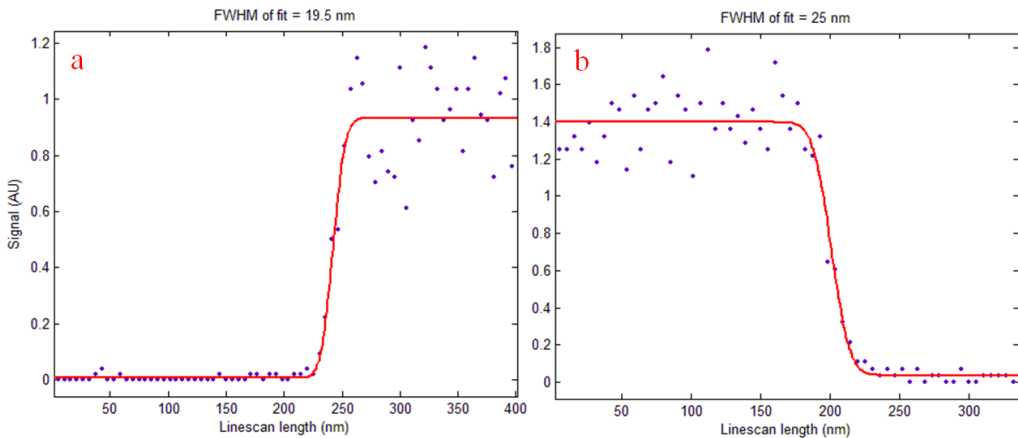


Figure 3.21 Beam spot fitting results for the experimental data in Figure 3.19 d. Figure a is for horizontal direction, while figure b is for vertical direction. FWHM of fit is 19.5 nm and 25 nm in the two directions.

3.5.3 Discussions on several challenges and future improvements for improving the beam spot size.

Lens cooling

As a large current is applied to the quadrupole lenses, particularly when focusing alpha particles, the coils will heat up. Although the lens is well designed with copper vanes to dissipate the heat, when the current applied is high, for example more than 60 amps, it is still necessary to use fans to help to cool down the lens. In the Figure 3.19, the image is taken using 1.7 MeV helium ions which requires one of the quadrupole lenses to maintain a current of 96 amps. In this case, a fan is normally used to cool the lenses from the side. In high resolution images, instabilities in the form of jagged edges can appear in the grid bar edges. If we temporarily turn off the cooling fan while the beam is scanning across the grid, then the jagged edge effect tends to disappear (as shown in the red square box in Figure 3.22). However, with the fan turned off, the lens rapidly heats up and the dimensions of the lens changes slightly. This is sufficient to move the beam axis, and as also shown in Figure 3.22 this rapid heating effect manifest itself as a movement in the STIM image. The

difference in the edge quality between the fan on and off indicates that the ‘jagged edge’ effect may be caused by air generated by the cooling fan. In order to keep the lens temperature stabilized to an acceptable level, the fan needs to create a powerful stream of air, which is invariably turbulent. This turbulence causes mechanical vibrations in the quadrupole lenses. These tiny movements (which are much less than 100nm) may be reflected in the image as jagged edges in images where the scan size is reduced.

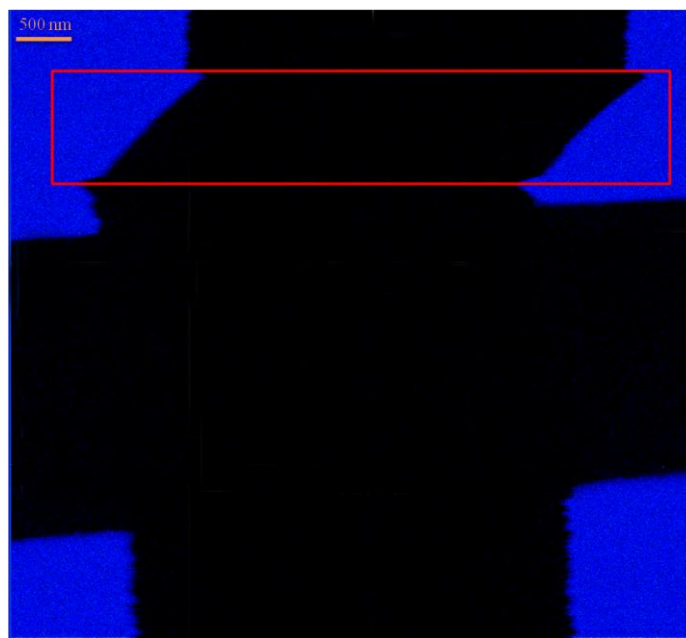


Figure 3.22 6 μm image of nickel grid cross. The beam is scanned faster in X direction and going down gradually in Y direction. Red box is the image when the cooling fan is temporarily switched off.

To solve or mitigate the fan’s effect, it may help to cool the lenses by blowing the air in the beam direction, since it looks as though the instabilities are in the horizontal and vertical directions. Figure 3.23 shows a simple cooling system we have used. Since the current applied to L1 is typically twice as those for L2 and L3 normally used for single spaced triplet, L1 is the hottest lens which therefore requires the most cooling. The white pipes in the figure extend their air outlets toward L1 and blow the air along the inside of the quadrupole lens

rather than from the side. This helps to dissipate the heat much faster, and hopefully will reduce lateral vibrations. For a current of 80 A applied to L1, the temperature of L1 can be stabilised at 48 °C using this cooling method. Figure 3.24 shows the grid image obtained using 1.7 MeV helium ions when this cooling method is applied and although the results are not definitive, it does indicate some improvement in edge smoothness..

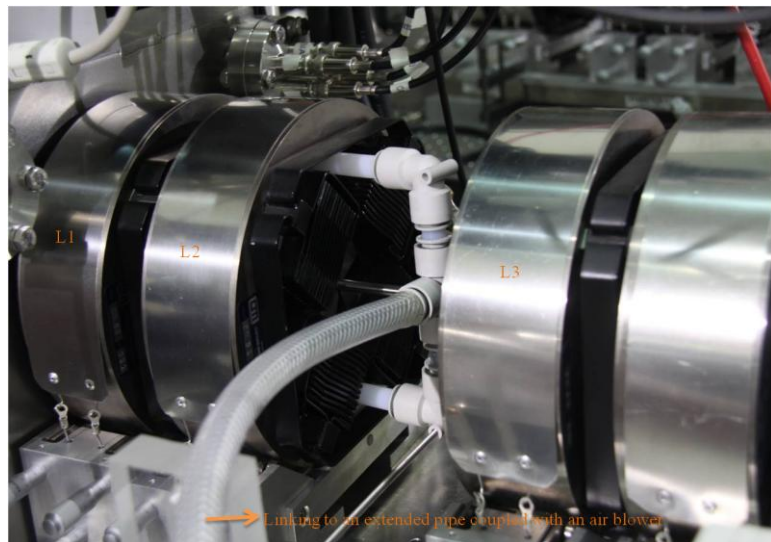


Figure 3.23 A simple improved cooling way. The current applied to L1 is the highest. The white pipe extends its blowing exit toward L1 to blow air in.

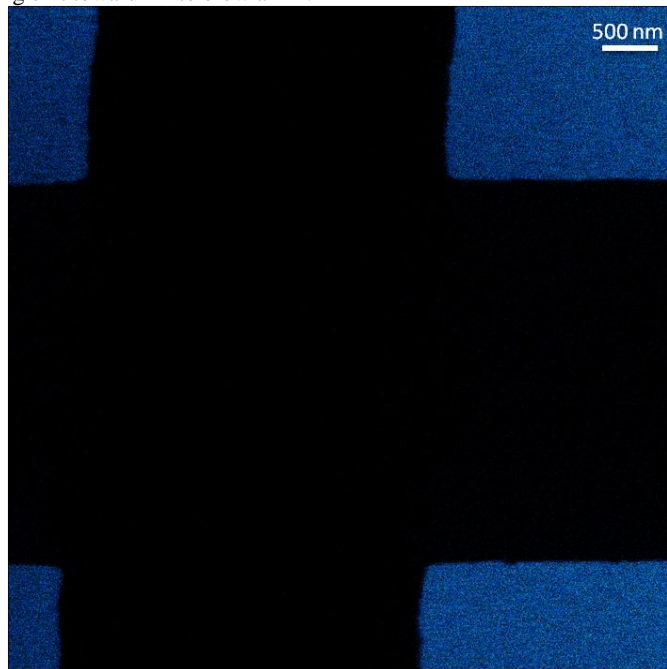


Figure 3.24 1.7 MeV alpha STIM image of grid after improvement on lens cooling.

Objects Slit surface damage

As discussed above, the final beam spot is the demagnified image of object slits aperture. Therefore the qualities of the object slits are important in focusing performance. However, since the object slits are continuously bombarded with protons and particularly alpha particles, they are easily damaged. This damage can manifest itself as pitting or flaking of the surface, or highly insulating cracked amorphous carbon layers forming on the slit surface. When charged particles pass through irregular surface structures, the edge of the slits are not well defined and this invariably affects the beam spot quality. In addition, the slit edges may charge up, which will in turn can create large localized time varying electric fields which may alter the beam path and cause the final resolution to be reduced. These effects can be avoided by regular replacement of object slits.

Scanning noise

Another important factor to affect the final image quality is scanning noise. The scanning noise can be divided into two parts. The first part is the noise from the computer card system, while the other part is from the scanning amplifiers. The noise level from computer card system is around 10 mV when the scanning output is 10 volts as measured using an oscilloscope. For images with 1024x1024 pixels, the voltage step for each pixel is around 10 mV, which is the same level as the computer system noise. By using high stability electronic components, the system noise level can be reduced to manageable levels. In our case, for the noise introduced by the scanning amplifier, as discussed in Chapter 3.2.4, high precision Techron amplifiers with 160

amplification are used to reduce scan amplifier noise for scans lower than 15 um.

Sample or target movement

For small scan sizes such as 10 um, using a 1024 or 2048 pixel data array, even a tiny movement of the sample can be reflected in the image. These tiny movements can occur when the nano stage current is not stable or a vibration is induced in the environment. For the first case, we found that target stability increased when we switched off the nano stage. For the second case, it is best to install some anti-vibration setup to completely solve the problem. Luckily, at present resolutions down to 20nm, the mechanical vibration in the CIBA lab appears acceptable.

Other Considerations

For high resolution ion beam microscopy work, a lot of things may affect the final beam size and image quality. During the beam line construction, proper beam line isolation, turbomolecular pump isolation and proper grounding are required to be considered. Any electromagnetic interference or vibration which may cause serious effect to the final result should be avoided.

3.6 Summary

As a summary for the chapter, a unique ion beam facility for biomedical imaging has been successfully built up in CIBA, and the performance achieved has easily reached the design goals. After precise alignment, it has demonstrated excellent performance in beam test experiments. The facility is capable of focusing MeV proton and helium ions to a spot size of around 25 nm. The scanning area for 2 MeV protons can be as large as 80x80 um without any perceived reduction in beam resolution. The following chapters will

further discuss some possible applications of this unique facility in current biological research.

Chapter 4 High Resolution Scanning Transmission Ion Microscopy and its Applications

Chapter 3 has demonstrated the excellent beam performance and superior system features achieved in the newly built cell imaging facility. This Chapter will discuss two related cell imaging techniques based on energetic ions that are capable of passing through the cell. These techniques are Scanning Transmission Ion Microscopy (STIM) and Forward Scattered Transmission Ion Microscopy (FSTIM), which is sometimes referred to as off-axis STIM. Because of the nature of fast ions, both techniques maintain the probe resolution through the cell, and are therefore suitable for high resolution whole cell imaging. In this chapter we demonstrate the use of STIM to image feature inside cells, and also use the techniques of STIM and FSTIM to demonstrate the ability of fast ions to visualize and quantify gold nanoparticles in a whole cell. We also show the ability of the well known technique RBS to ascertain the depth of the nanoparticles within the cell. Finally, some future work and possible improvements on these techniques will be discussed.

4.1 Basic Principles, Experimental Setup and Analysis of STIM

4.1.1 A description of ion beam biological imaging techniques

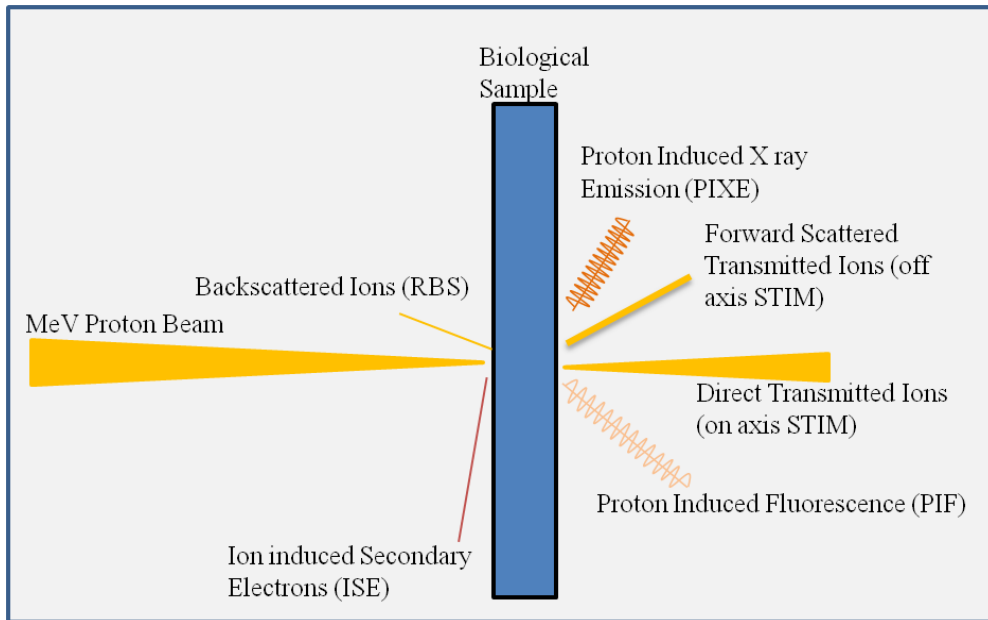


Figure 4.1 MeV ion beam interactions with biological sample. Each ion induced signal can be detected and developed as an imaging technique labeled in the bracket.

Figure 4.1 shows typical MeV ion beam induced signals from biological samples. Among them, Proton Induced X-ray Emission (PIXE) is the most developed technique and is already widely used for elemental analysis in biological research. Rutherford Backscattering Spectroscopy (RBS), Scanning Transmission Ion Microscopy and Proton Induced Fluorescence have been introduced in Chapter 2. Ion induced Secondary Electrons is a surface imaging technique which in principle similar to Scanning Electron Microscopy (SEM) except that we use the ion beam to excite secondary electrons. The Helium Ion Microscope (HIM) utilising low energy ions is a commercial microscope based on this technique, and this instrument has already demonstrated better performances than current SEM technology, with sub nm resolutions achieved so far. Among all these techniques, PIXE and RBS require relatively large beam currents (typically more than 50 pA), and so sub-100nm resolutions are

currently not possible for these techniques. However, all the other techniques require low beam currents (eg less than 10fA) and therefore based on the beam performance of the new cell imaging beam line, these techniques can be used for high resolution imaging. We do not concentrate on the technique of ion induced secondary electron imaging in this chapter, since this can be carried out at much better resolutions using the low energy Helium Ion Microscope. In this chapter we discuss the application of fast ion STIM, and in chapter 5 we introduce the new technique of proton induced fluorescence.

4.1.2 Basic Principles of STIM

Scanning Transmission Ion Microscopy (STIM) is a microscopic technique based on detection of transmitted ions. The particle detector is placed on the beam axis, directly behind the sample. STIM images are normally energy loss contrast maps generated by measuring the transmitted ion energy at each image pixel within the scanned area. STIM detects all the directly transmitted ions, which can suffer many hundreds of electron collisions in passing through a whole biological cell. The incoming ions also interact with atomic nuclei, but with much lower cross sections. The energy loss of an ion transmitted through a thin sample depends on the elemental composition and thickness, that is, the areal density, where

$$\text{density} = \int_{E_o}^{E_r} \left[\frac{dE}{d(\rho z)} \right]^{-1} dE \quad \text{Eq 4.1}$$

E_o is the initial ion energy and E_r is the remaining ion energy after passing through the sample. With STIM, the transmitted ion energies and number of ions at each pixel within the scanned area are measured using a detector located on the beam axis behind the sample. The DAQ system then generates

an image corresponding to the ion energy loss, which essentially is an image showing variations in the areal density. Only one ion per pixel is required in principle to measure the energy loss, but, in practice, owing to energy straggling, several ions are required to generate low noise images. The best method of generating a STIM image is using an event-by-event data acquisition system such as IONDAQ, as described in Chapter 3. The measured data set of the ion energy loss values at each pixel can be manipulated in median processing to give the best image contrast. With median processing, the measured energy loss of every ion falling within an image pixel is ordered by increasing energy loss, and the central value is chosen.. Median processing of event-by-event STIM data improves the accuracy of measuring the ion energy loss at each pixel by utilizing the information from all the measured ions, which reduces the effect of the measured ion energy spread. This reduces statistical noise, and sharpens the image considerably. Depending on the thickness of the sample, the resolution of STIM throughout the sample is similar to the beam spot size. The highest resolution can be achieved in thin samples with a thickness of around several micrometers, although due to small angle scattering of the beam, the final image in thicker samples may be degraded due to the spread of the beam. However, for cell imaging, whole single cells are only several micrometers thick in the dry state, which is optimal for high resolution STIM imaging.

4.1.3 Basic principle of FSTIM

Direct transmitted ions which have suffered energy loss but virtually no scattering can be imaged using STIM. However, there are a smaller number of ions which have also suffered small angle nuclear collisions. The transmitted

ions which have been scattered in a forward direction can also be detected, and this technique is called Forward Scattered Transmission Ion Microscopy (FSTIM), or off-axis STIM. The energy loss of these ions includes both the multiple electron collisions and small angle nuclear collisions. Because of the lower cross section of nuclear scattering, a typical FSTIM signal is obtained from an ion which has suffered multiple electrons collisions but only one or several small angle nuclear collisions. FSTIM images are generated by measuring variations in the number of ions at each image pixel within the scanned area. Variations in the number of ions are mainly determined by the small angle nuclear scattering process, which is given by the Rutherford Formula:

$$\sigma = \frac{Z_1^2 Z_2^2 e^2}{4E_0^2 \sin^4\left(\frac{\theta}{2}\right)} \quad \text{Eq 4.2}$$

where σ is the cross section of the nuclear scattering through a given angle; Z_1 and Z_2 are the atomic numbers of incident ion and target element respectively; E_0 is the initial energy of incident ions; and θ is the scattering angle [52]. For the same beam and experimental setup, the cross section is proportional to the square of target atomic number. Therefore FSTIM can be utilized effectively to image heavier elements, and this interesting feature will be further discussed later in the chapter.

4.1.4 Pixel Normalization

Conventionally, in raster scanning the beam is controlled to stay at each pixel for a certain time period (named pixel dwell time), collect data at this pixel, and then move to subsequent pixels, until the whole image is complete. However, when the beam intensity is not quite stable, this scanning method

may result in large variations in the number of ions received in each pixel, which will cause noise and poor image quality. As discussed in Chapter 3, an added function in IONDAQ called Pixel Normalization is able to solve the problem. It controls the beam so as to dwell at each pixel until the detector collects a specific number of ions, and then moves the beam to another pixel. In this case, even when the beam intensity is fluctuating considerably, pixel normalization ensures the same number of ions is collected for every pixel. Figure 4.2 shows a comparison between the images taken with pixel normalization and without pixel normalization. The left image taken with pixel normalization shows reduced noise and much better quality. Some of the bright spots in Figure 4.2b which are caused by beam instability disappear in the image with pixel normalization since the received count rate for each pixel is constant in spite of beam fluctuation.

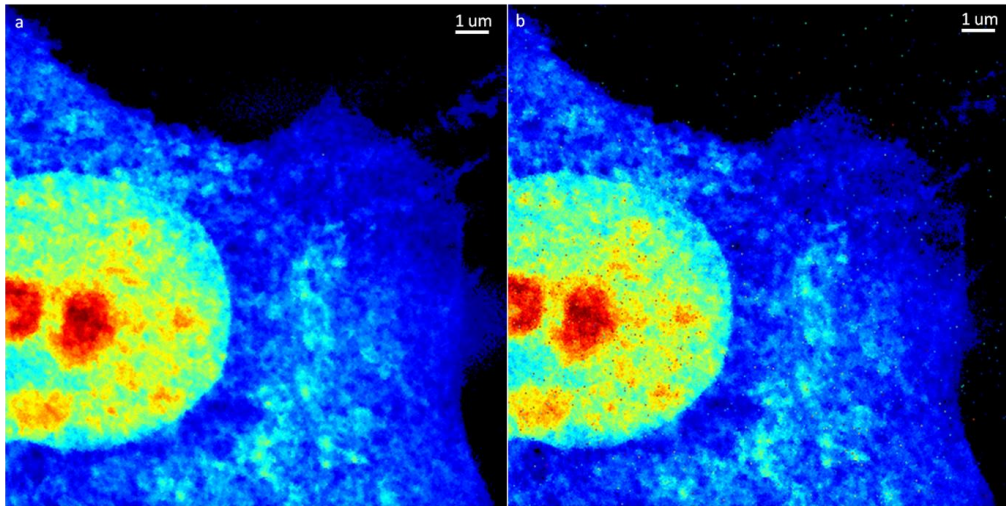


Figure 4.2 Direct Helium ion STIM images of a human fetal liver cell. Image taken with pixel normalization is showed in figure a; while image of the same cell taken without pixel normalization is showed in Figure b. Beam current is fluctuating in 20% around 10 KHz. Beam: 1.2 MeV helium ions. Color map: Jet.

4.1.5 Comparison of proton STIM and helium ions STIM

The large number of collisions that MeV ions suffer as they pass through the sample results in energy straggle, lateral spread, and angular spread of the beam emerging from the rear of the sample. The resolution of small variations in areal density improves with the use of heavier ions, because they have a higher rate of energy loss, but is limited by the increasing ion energy straggle. However, areal density contrast increases with increasing ion mass, because the rate of energy loss increases much faster than the energy straggle. The lateral beam spread for the different ions passing through a thin (less than 1 μm) layer of biological material does not vary greatly, but the spread is significantly greater for ions passing through denser material. The range of heavier MeV ions drastically decreases with increasing ion mass, which limits the use of heavy ions for STIM measurements. Therefore, MeV proton and helium ions are the most suitable particles used for STIM.

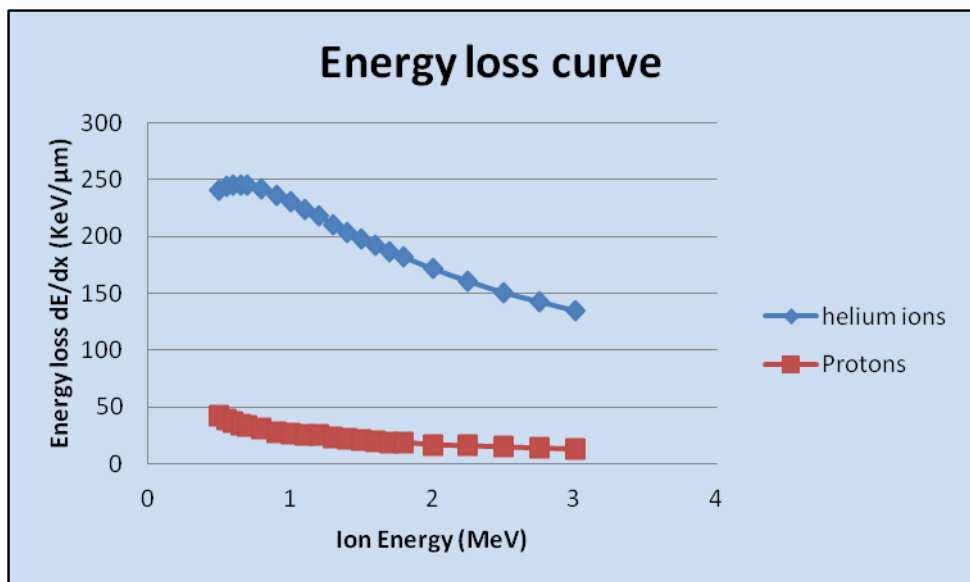


Figure 4.3 Energy loss curve of helium ions and protons penetration into biological material (human pancreas tissue).

Figure 4.3 shows the energy loss for helium ions and protons penetration into biological material. For beam energies from 1 MeV to 3 MeV, the energy loss dE/dx gradually reduces. In addition, for the same energy, the energy loss for helium ions is roughly 10 times greater than for protons. If we consider the characteristics of straight paths and relatively deep penetration, both MeV proton and helium ions are suitable for STIM of whole cells. Compared with protons, helium ions have higher stopping power, and therefore higher energy loss contrast. Figure 4.4 shows a comparison of proton STIM and helium ions STIM images of the same HeLa cell. The beam parameters, including number of ions per pixel, and spatial resolution, are essentially the same. However, Figure 4.4 shows quite a large difference for the two beams: As expected, helium ion STIM shows much higher contrast and exhibits more detailed features, while for protons it is even hard to distinguish the cell edge with the substrate. On the other hand, due to the much higher stopping power, the penetration power for MeV helium ions is much smaller, although for this case, the penetration is adequate. However, because of the higher stopping power of He ions, there is also a higher number of multiple nuclear scattering effects. This results in an increasing lateral broadening of the beam as it traverses the cell. The effective spatial resolution of helium ions STIM is therefore slightly lower than for protons of the same incident beam spot size.

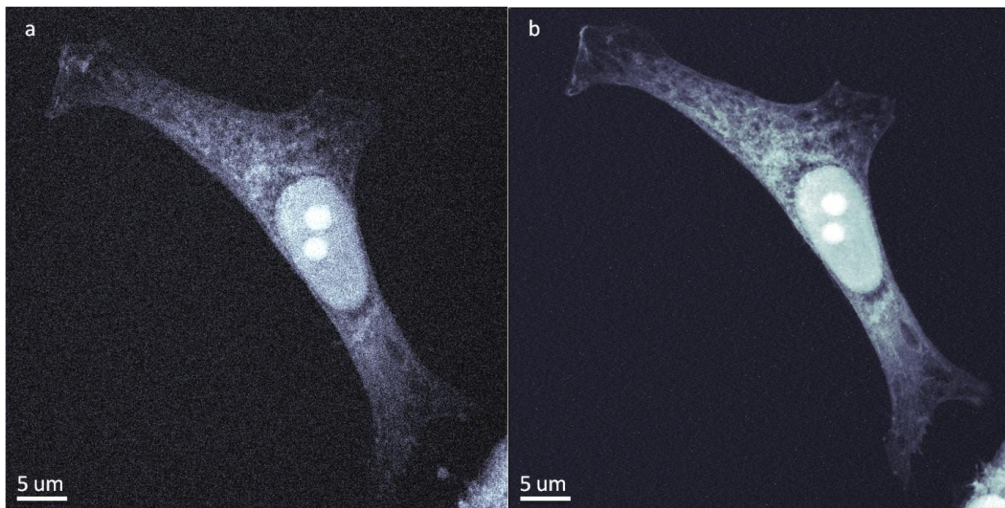


Figure 4.4 On axis STIM images of a HeLa cell from the same energy (1.5 MeV) protons and helium ions. Figure a is for proton STIM and Figure b is for helium ions STIM. The beam currents are 10 KHz for both of them. The beam spot size is around 50 nm.

If we consider the damage to the sample, the surface sputtering effect is higher when using helium ions, especially for lower energies. Helium ions also produce more sample atomic displacements compared to protons with the same energy. As a result, helium ions cause more damage to both the sample surface and internal structure, although this does not seem to be a major problem since information is usually extracted from the sample before such damage is noticeable..

Radiation damage however is a critical problem for semiconductor charged particle detectors [53]. It is necessary to consider this when comparing proton STIM with helium ion STIM. Two basic radiation damage mechanisms can be occurred for semiconductor silicon detectors; displacement damage and ionization damage. Displacement damage is caused by the displacement of silicon atoms from lattice sites by incident radiation particles. Ionization damage occurs when energy is absorbed by electronic ionization in insulating layers, typically SiO_2 . This liberates charge which drifts or diffuses and is eventually trapped either in the insulator layer or interfaces. Radiation damage

can change the effective doping concentration, increase leakage current, charge carrier trapping, and finally cause detector failure. The symptoms of radiation damage are higher leakage current and noise, with degradation of energy resolution. This is exhibited in the energy spectrum by peak broadening and sometimes double peaking. For the silicon surface barrier detectors currently used in the CIBA high resolution STIM imaging, the threshold doses for protons and alpha particles are 10^{10} and 10^9 particles/cm² respectively [54]. Since the threshold dose for protons is ten times higher than alpha particles, detectors can be used for 10 times longer for protons for the same radiation dose. In alpha STIM experiments, the peak broadening can easily be observed when scan times are long (eg 10,000 ions per second for 30 minutes). Since this degrades the contrast, we usually limit our experiments to around 20 minutes. For multiple scans, we move the detector to a new position in between different images frames. Comparably, this effect is an almost negligible issue for proton STIM.

The energy resolution of current silicon-based particle detector is not sensitive enough for proton STIM to achieve high contrast images. If the energy resolution could be improved to 10 times higher than current values, then we could utilize protons to get the same effective contrast as helium ion STIM images. This would have the advantage of being able to scan thicker samples, and also this would result in much less damage to both samples and detectors compared with the same energy helium ions. One possibility may be to employ time of flight detection technique, which is likely to improve the energy resolution 10 times higher than currently widely used silicon particle

detectors. With such a high energy resolution detection system, we could utilize MeV protons, instead of alphas, to achieve high contrast STIM images.

4.1.6 Helium Ion Microscope and Helium Ion STIM

In order to get high resolution cell images from any scanning beam microscope one must be able to produce a sufficiently small probe which maintains its probe size as it penetrates the cell, have a small interaction volume within the sample and produce an abundance of information-rich signals to create the image. Due to the much smaller de Broglie wavelength, in theory, helium ions can be focused to a size much smaller than either electrons or X-rays. Slow (eg 10-50keV) helium ion beams can now be focused to sub-nanometre dimensions, and can be used to image the surface of samples by detecting induced secondary electrons. Low energy helium ion microscopy offers significant advantages compared with electron microscopy for surface imaging since insulating samples can be imaged without the need for a conducting metallic coating [34, 36, 55]. In addition, fast (eg 1 – 2 MeV) helium ions can also be focused to 25 nm as shown in Chapter 3, and because of the increased energy and high mass of the helium ion, this resolution is maintained when penetrating whole cells.

Although low energy Helium Ion Microscope and high energy Helium Ion STIM use the same ion species, the way the techniques function are fundamentally different. Figure 4.5 gives an indication of the interaction of slow and fast helium ions with respect to a cell. For the case of a MeV ion beam, energy losses are due mainly to multiple electron collisions, and while the energy remains high, there is minimal scattering. Because MeV ions pass

through the cell, nuclear collisions are rare and large-angle scattering is minimal. Therefore, images that are formed by detecting the energy loss of transmitted ions do not suffer any significant deterioration in spatial resolution. In the case of low-energy HIM, the ions do not have the range to pass through the cell, resulting in large-angle scattering within the cell. However, because images are formed by detecting secondary electrons originating near the cell surface, the surface image quality is not affected.

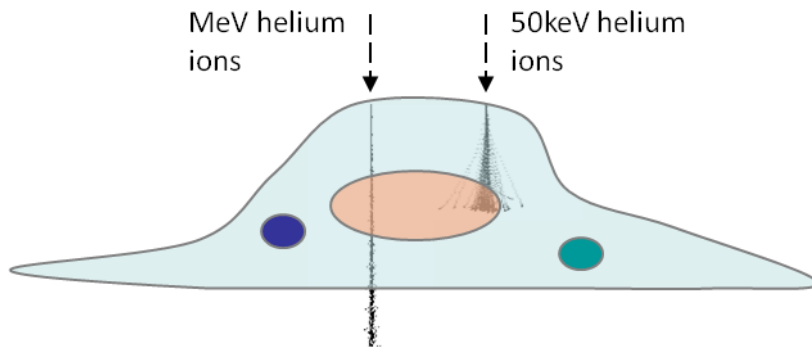


Figure 4.5 Paths of fast (eg ~MeV) and slow (eg ~50keV) helium ions through a cell of nominal thickness 1 micron. The ions initially travel in straight lines losing energy via multiple electron collisions. Towards the end of range nuclear collisions, and therefore large angle scattering, becomes predominant.

Figure 4.6 shows Monte Carlo simulations of fast helium ion trajectories through organic material. If the nominal thickness of a dehydrated cell is taken to be $1 \mu\text{m}$, then MeV ions can pass through the cell with most ions maintaining a straight trajectory. At MeV energies, only a small minority of ions suffer large-angle nuclear collisions. Monte Carlo simulations for 500 He ions indicate that 1), for 1 MeV He ions passing through the cell, 45% are contained within a radial distance of 5 nm of the original beam axis, and 80% are contained within 10 nm; 2), for 1.5 MeV He ions, 75% are contained within a radial distance of 5 nm, and 93% are contained within 10 nm; and 3), for 2 MeV He ions, 83% are contained within a radial distance of 5 nm, and 95%

are contained within 10 nm. The current state of the art for focusing MeV ions is 25 nm, and these simulations indicate that this resolution does not deteriorate significantly as the ions pass through the cell.

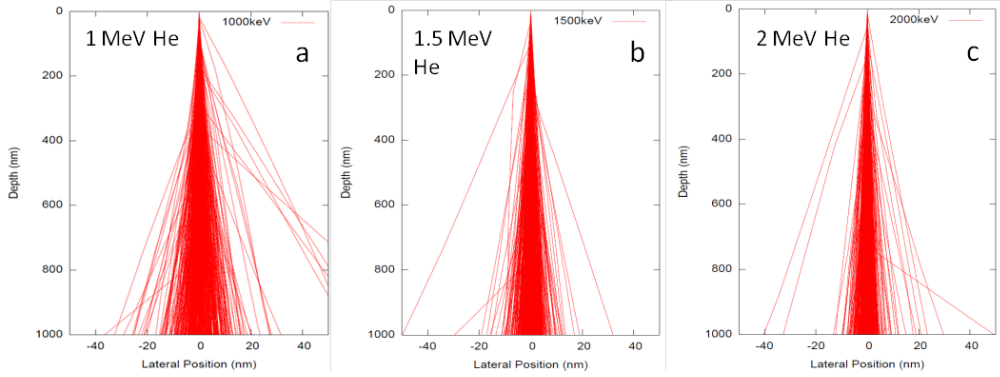


Figure 4.6 Fast helium ions paths ((a) 1 MeV, (b) 1.5 MeV, and (c) 2 MeV) through 1 μm of biological material calculated using the Monte Carlo simulation code DEEP [45].

As a comparison, the simulated trajectories of a low energy helium ion beam (50 KeV) and an electron beam (50 keV) passing through the cell are shown in Figure 4.7. Figure 4.7a shows simulations for slow helium ions (50 keV) indicating they do not have the range to pass through a cell of nominal thickness 1 μm , and that their trajectories show significant spreading within the cell. Slow helium ions cause slight sputtering of the target material, and induced secondary electrons are emitted from the surface, which can subsequently be detected to create a high-resolution image of the surface. The nuclear scattering toward the end of the range results in a high degree of lateral and longitudinal straggling, but this does not affect the surface image quality. For electrons, as shown in Figure 4.7b, there is a significant deviation of trajectories as the incoming electrons interact with atomic electrons in the sample. The energy loss mechanism in this case is mainly electron/electron collisions, resulting in significant large-angle scattering. The scattering,

estimated at >100 nm at the cell exit, precludes high-resolution transmission electron microscopy on thick samples. Trajectories of slow helium ions also show significant spreading, where in this case ion/nuclei scattering is predominant[56]. However, compared with electrons, due to the higher mass and momentum, the helium ion beam has a smaller interaction volume at the surface and higher depth of focus. This gives the HIM significant advantages for surface imaging. Furthermore, considering that both the SEM and HIM techniques function by detecting the secondary electrons emitted from the sample surface, since one helium ion is capable of inducing 2 to 8 secondary electrons compared with one for an incoming electron, the surface contrast using helium ions is much better.

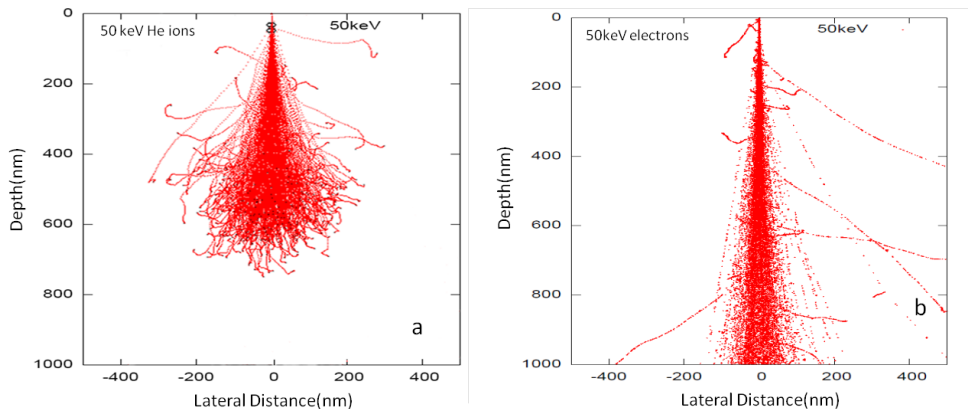


Figure 4.7 (a) Slow helium ion paths through biological material calculated using the simulation package [56]. In this case, the range for 50 KeV helium ions through 1 μm biological material is ~600 nm, which is insufficient to pass through a cell of nominal thickness 1 μm . (b) As a comparison, simulated paths of 50 KeV electrons through 1 μm of biological material is also simulated using [45].

As an example of the imaging potential of microscopy using helium ions, a human fetal liver cell is imaged using both slow and fast helium ions. Human fetal liver cells [57] were seeded on to silicon nitride windows of thickness 100nm, with a density of 10,000 cells/cm² and allowed to attach for 24h prior

to fixation in 4% formaldehyde. Samples were then dehydrated through an ethanol gradient followed by critical point drying [41].

The HIM images in Figure 4.8., *a* and *d*, were taken at 45 keV ion energy, and many surface features are apparent. Whether these surface features are artifacts or part of the cell is unknown. Images of the same cell obtained with fast helium ions (1.2 MeV) were also acquired at the cell imaging facility of CIBA [50]. The images depicted in Figure 4.8, *b* and *e*, are transmission images based on the energy loss of 1.2 MeV helium ions passing through the cell. These images quite clearly show both surface and internal features, including filamentary structures assumed to be part of the cytoskeleton. Of interest, not all of the surface features shown in the surface images appear with high contrast in the transmission image (see, for example, features marked with arrows in Figure 4.8, *a*, *b*, *d* and *e*). We assume that in these cases the surface structures are hollow and therefore have lower contrast in the transmission images as compared with the surface images. As expected, however, the nucleus, nucleoli, and various internal structures around the nucleus, which are not seen in the surface image, are observed in the transmission image with high contrast and edge sharpness. The helium ion images in Figure 4.8 indicate the complementary nature of imaging using slow and fast helium ions.

Further information can be extracted from the transmission energy-loss data. As the fast helium ions pass through the cell, each ion undergoes multiple collisions with atomic electrons, and at each collision the ion loses a small amount of energy. The link between mass and energy loss can be obtained from the stopping power of the ion in traversing the cell, which can be

extracted from known tabulated data. For example, a 1.2 MeV ion passing through a A-150 tissue-equivalent plastic has a stopping power of 2218 MeV cm²/g [58]. By measuring the energy loss of each ion at each position in the cell, we can obtain an image that represents the mass distribution within the cell. For example, for the case in which a 1.2 MeV helium ion has lost half of its energy (600 keV) in passing through a cell, the ion will have traversed a calculated tissue-equivalent mass areal density of 2.75 attograms (ag)/nm². The images in Figure 4.8, *c* and *f*, represent the mass distribution of the cell, and indicate the high-density difference between the cytoplasm and the nucleus. There is a similar difference in density between the nucleus and the nucleoli. If we assume that we can measure the transmitted α particle beam energy to within 6 keV, which represents the state-of-the-art performance of a silicon particle detector positioned directly behind the cell, then for a 1.2 MeV α particle passing through a cell, the mass/unit area resolution is 0.0275 ag/nm². This represents an extremely high-contrast mechanism for structural imaging.

HIM at keV and MeV energies has a high potential for imaging surface and internal structures in whole cells at resolutions that are not attainable with other techniques. HIM at keV energies uses a high brightness field emission ion source that enables resolutions of 0.25 nm to be achieved. By increasing the beam energy to 100 keV in the same column, we may be able to achieve a spatial resolution approaching 0.1 nm. The prototype fast helium microscope operating at MeV energies uses a low-brightness RF ion source, and as such the spatial resolutions are currently limited to \sim 25 nm. Work is currently in progress to improve the spatial resolutions of MeV HIM to the nanometer

level by increasing the ion source brightness, and this will enable structural imaging of whole cells at nanometer dimensions.

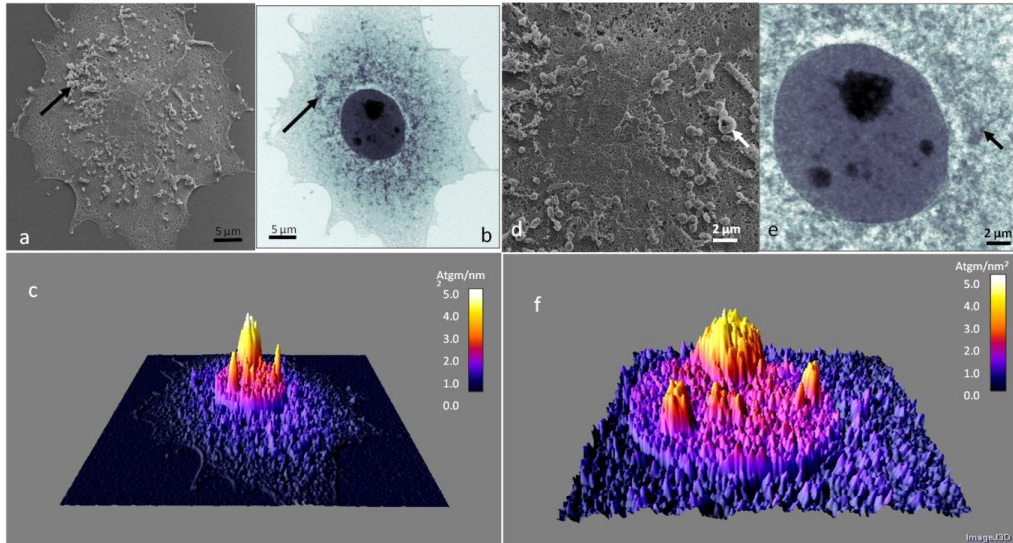


Figure 4.8 (a) HIM secondary electron image of a human liver cell, showing surface features. Helium ion energy = 45 KeV. (b) Helium ion (STIM) transmission energy loss images of the same cell, showing structural features common to the surface as well as structural features from within the cell. Helium ion energy = 1.2 MeV. Filamentary structures within the cell, as well as the nucleus, can be observed. (c) Mass image showing a 3D plot of the mass distribution (in units ag/nm²): [1 ag = 10⁻¹⁸ gm]. Helium ion energy = 1.2 MeV. The arrows in a–b correspond to a surface feature that has high contrast in the surface image but exhibits a low-contrast circular structure in the transmission image, implying a hollow structure. (d–f) Higher-magnification images from the region of the cell containing the nucleus. The arrows in e and f correspond to a surface feature that has high contrast in the surface image but has a ring-like structure in the transmission image, once again implying a hollow structure.

4.2 Three dimensional visualization and quantification of gold nanoparticles in a whole cell

4.2.1 Nanoparticles and conventional microscopic techniques for nanoparticles imaging

In the field of nanotechnology for biomedical applications, scientists and clinicians are combining their efforts towards medical intervention at the molecular scale for diagnosis, prevention, and treatment of diseases. To this end, particles with sub-microscopic dimensions represent ideal candidates to penetrate the least accessible compartments within tissues and cells and further,

and offer the additional advantage of escaping from premature degradation and elimination from the body.

Multifunctional nanoparticles already have widespread biomedical applications [59, 60], for example as carriers for targeted drug delivery and gene delivery [61], as efficient contrast agents for molecular imaging in medical diagnostics [62] and as therapeutical reagents for targeted photothermal therapy [63]. Recently, nanoparticles have proven to be useful in cancer therapy allowing for effective and targeted drug delivery [64, 65]. However, because of the lack of adequate imaging techniques that can visualize three dimensional local populations of nanoparticles within a whole cell or inside cellular components [66], the mechanisms underlying the cell's ability to internalize external particles, coupled with the transport of functionalized targeted nanoparticles within the cell, remains difficult to investigate.

Single NPs cannot be resolved by conventional optical microscopy due to diffraction limits placed on its spatial resolution, and for that reason, electron microscopy is typically used to visualize nanoparticles. Although Transmission Electron Microscopy (TEM) has been very successful in identifying nanoparticles in thin cellular sections, it remains difficult to resolve the gold nanoparticles at nanoscale resolution in the whole cell. Due to large angle electron/electron scattering, electron microscopy can only maintain its high resolution in a thin sample, and therefore sample preparation for TEM typically includes processing of samples into 50-200 nm thin serial sections, a step that involves the risk of NP removal or displacement. A further disadvantage is the difficulty in obtaining quantitative results, since thin

sections may slice through three-dimensional structures such as vesicles containing high densities of NPs. To overcome these disadvantages, several other techniques have been applied to image NPs inside whole cells. Scanning Transmission Electron Microscopy (STEM) has been reported to visualize gold nanoparticles in a whole cell [23]. This method enables high resolution around 10nm in the focal plane, although out of this plane, the resolution is greatly reduced due to electron scattering. Another recently developed technique, known as scanning near field ultrasonic holography (SNFUH), also offers a way to resolve sub-surface NPs with sub 100nm resolution [67, 68].

4.2.2 Visualization and quantification of gold nanoparticles (AuNPs) using helium ions

A new microscopic approach has been developed to visualize NPs three dimensionally and also to quantify the numbers of NPs within a whole cell using fast helium ions. As discussed in the above sections, fast ions with sufficient energy capable of penetrating through a whole cell (eg > 500 keV protons, and > 1 MeV alpha particles) have high potential for imaging internal structure of the cell since fast ions maintain a straight trajectory when traversing material. The interaction of fast ions with matter is mainly through ion/electron collisions, and due to the high mass mismatch with electrons, ions suffer very low energy transfer and minimal scattering for each collision. As a result, thousands of collisions can occur before the ions stop, and the ion path is characterized by straight, deep penetration into the material [45]. By detecting directly transmitted ions, a map of energy loss contrast can be obtained, which includes detailed cell structural density information (Scanning Transmission Ion Microscopy - STIM) [69].

As well as ion/electron interactions, there is also a smaller probability that the MeV ion undergoes elastic scattering from atomic nuclei. The cross section for nuclear elastic collisions (σ) is given by Eq 4.2.

$$\sigma = \left[\frac{Z_1 Z_2 e^2}{4E_c \sin^2(\theta_c / 2)} \right]^2 \quad \text{Eq 4.2}$$

Where Z_1 and Z_2 are the atomic numbers of the incoming ion, and the target ion respectively, E_c is the incoming ion energy, and θ_c is the scattering angle from the original ion path.

In nuclear elastic collisions, the incoming ion can be forward scattered ($\theta_c < 90^\circ$) or backscattered ($\theta_c > 90^\circ$) (Rutherford backscattering). By detecting forward scattered ions at angles $\theta_c \sim 5-10^\circ$, an image reflecting sample elemental information can be formed. In this technique, called Forward Scattered Transmission Ion Microscopy (FSTIM), the scattering cross section increases as Z^2 and therefore there is a higher probability of scattering from high Z heavy elements compared with the low mass elements (C, O, H) normally found in the cell.

By measuring the energy of the backscattered ions (eg at $\theta_c \sim 160^\circ$, in a process known as Rutherford Backscattering Spectrometry (RBS), the depth position of the target atom can be identified, although at the expense of much lower scattering cross-sections. RBS is a technique well known in materials research, and is particularly efficient at element identification and depth profiling heavy elements in low mass matrices such as organic materials. In the case of NPs buried within a cell, the energy loss exhibited by backscattered ions is approximately proportional to the depth of the NP.

Therefore we employ three complementary and related techniques in order to provide a 3D image of the nanoparticles in the whole cell: (i) STIM: Direct energy loss imaging using on-axis detection of transmitted ions to image cell structure, (ii) FSTIM: Detection of off-axis transmitted ions that have undergone forward nuclear scattering to provide a lateral image of the nanoparticles in the cell, and (iii) RBS: Detection of backscattered ions to provide information on the depth of nanoparticles in the cell.

As discussed in Chapter 3, current state-of-the-art performances for MeV ion beam focusing at the Centre for Ion Beam Applications, Dept of Physics, National University of Singapore [50] are 25 nm spot sizes for STIM and FSTIM, which require low probe currents of 5,000 – 20,000 ions per second, and 200 – 300 nm spot sizes for RBS. As a result of the reduced cross section at backward angles, the resolution for RBS is degraded because higher probe currents up to 100 pA are required.

Results:

A schematic diagram of the experimental set-up is shown in Figure 4.9. A focused beam of MeV ions pass through an annular surface barrier (RBS) detector and is scanned over the cell. The backscattered ions from the cell are detected by the RBS detector. The transmitted ions that are forward scattered at shallow angles are detected by an annular surface barrier (FSTIM detector), and the ions that pass directly through the cell without significant angular scattering are detected by the STIM surface barrier detector.

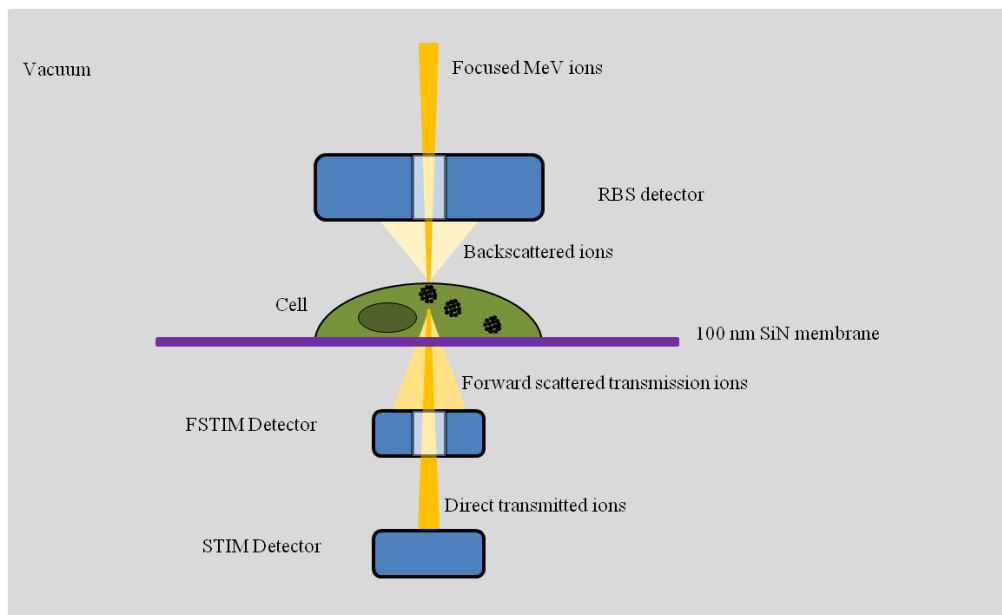


Figure 4.9 Schematic diagram of the experimental setup for cell imaging using fast ions.

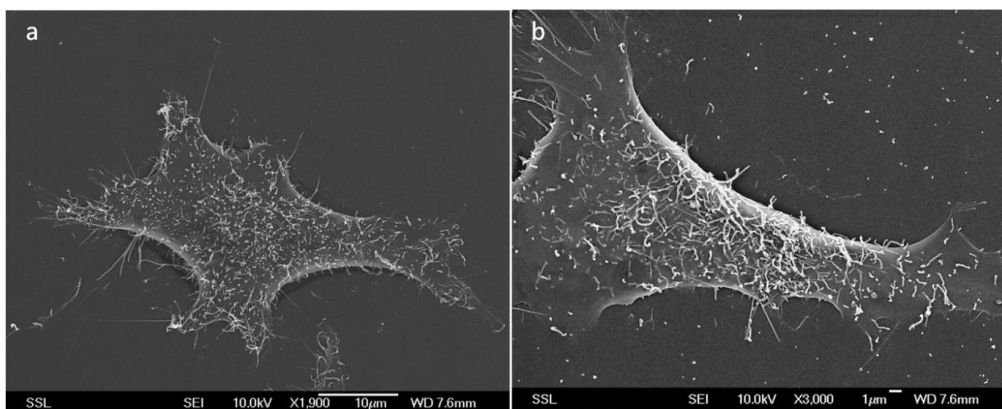


Figure 4.10 Scanning electron micrographs of a) HeLa cell (control), b) HeLa cell cultured in an environment of Au NPs.

Figure 4.10 shows SEM images of two cells (refer to Appendix A): a HeLa cell grown in a control environment (control cell), and a HeLa cell grown in a 100 nm gold NP environment (NP cell). The NP cell SEM image shows nanoparticles present in the background, whereas in the control cell none are observed. Figure 4.11 and Figure 4.12 show STIM images of the control and NP cells at different magnifications. The images differ in that the SEM images depict the cell surface, whereas the STIM images depict the ion energy loss as

the ions pass through the cell, and therefore are indicative of the internal structure of the cell. The STIM images show that the nuclei and nucleoli have greater densities compared with the surrounding cytoplasm and organelles, and whilst there is some evidence of nano-sized structures in the NP cell images, the contrast is not sufficient to differentiate the Au NPs from dense focal structures normally found within the cell.

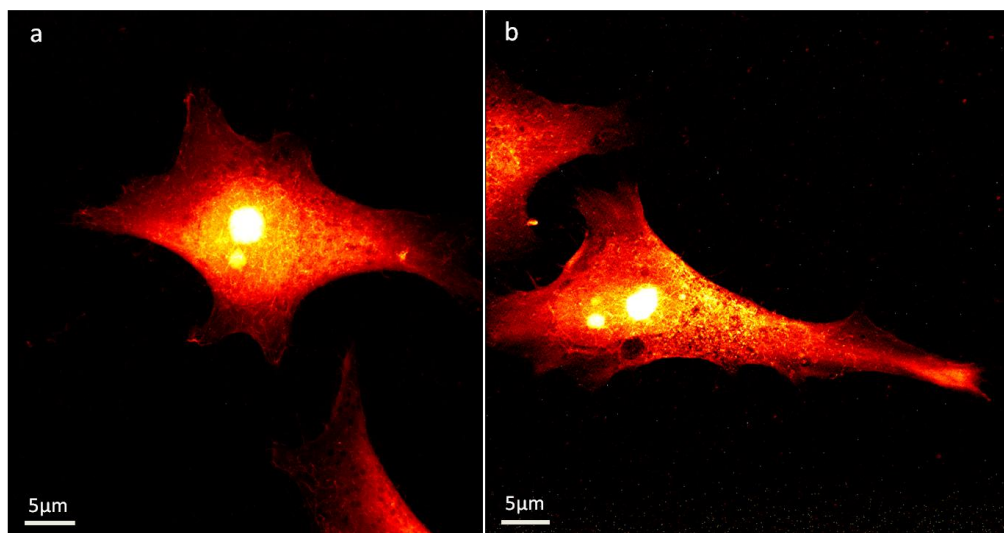


Figure 4.11 Scanning transmission ion microscopy (STIM) images of a) HeLa cell control, b) Hela cell cultured in an environment of Au NPs. 1.6 MeV helium ions.

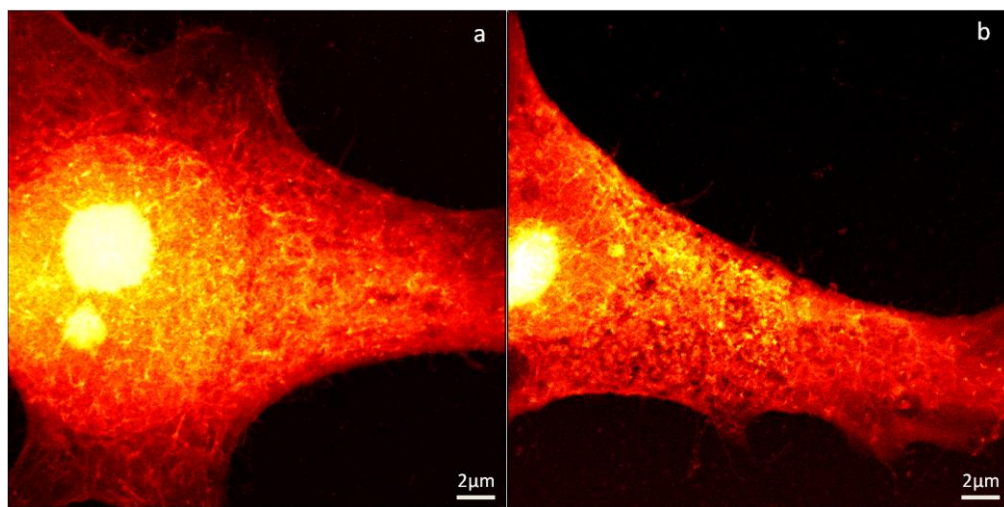


Figure 4.12 Higher magnification scanning transmission ion microscopy (STIM) images of a) HeLa cell control, b) HeLa cell cultured in an environment of Au N/Ps. 1.6 MeV helium ions.

Figure 4.13 shows images of the FSTIM results for both the control and NP cells. The FSTIM image of the NP cell, as expected, has increased scattering from the gold nanoparticles. The contrast is high, and individual nanoparticles as well as NP clusters are easily resolved. No NPs are detected in the control sample. FSTIM however does not differentiate between the NPs on the surface of the cell and those which have been internalised by the cell. We therefore need to utilize the depth resolving feature of RBS to elucidate whether or not the particles are on the surface or within the cell.

Figure 4.14 shows the RBS energy spectrum from the cell scan, and indicates the energy windows chosen to differentiate between surface and subsurface NPs. Images of the RBS results are shown in Figure 4.15.

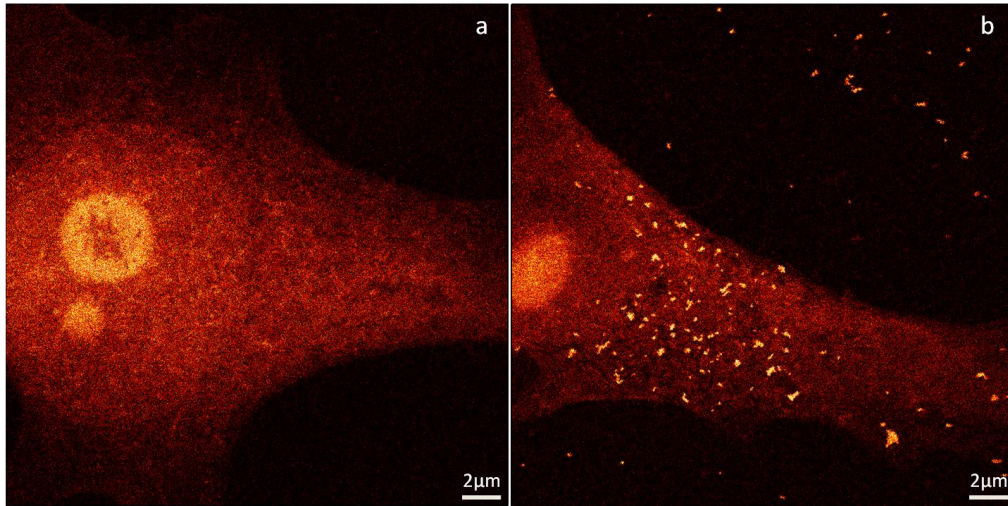


Figure 4.13 Forward scanning transmission ion microscopy (FSTIM) images of a) HeLa cell control, b) Hela cell cultured in an environment of Au NPs. 1.6 MeV helium ions.

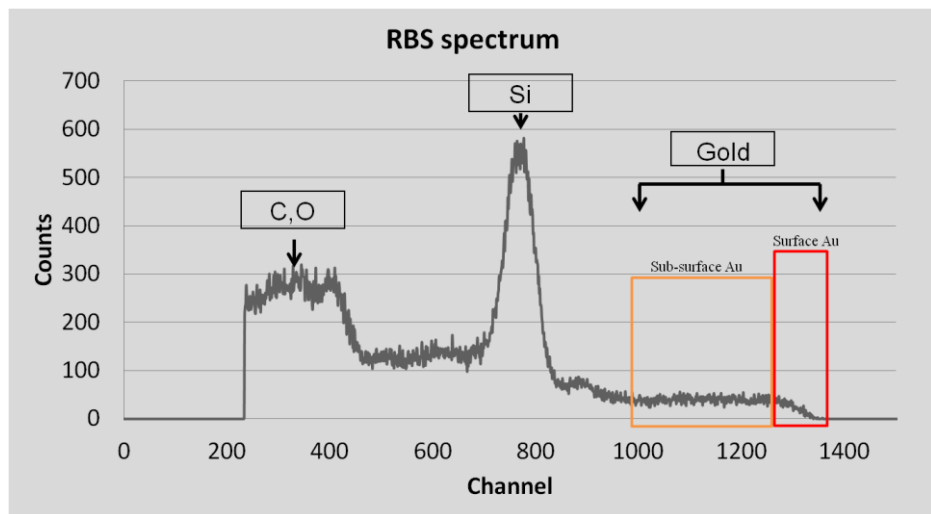


Figure 4.14 RBS energy spectrum from the NP cell showing C and O counts from the cell, Si and N counts from the Silicon Nitride Window, and Au counts from the NPs. 1.6 MeV helium ions.

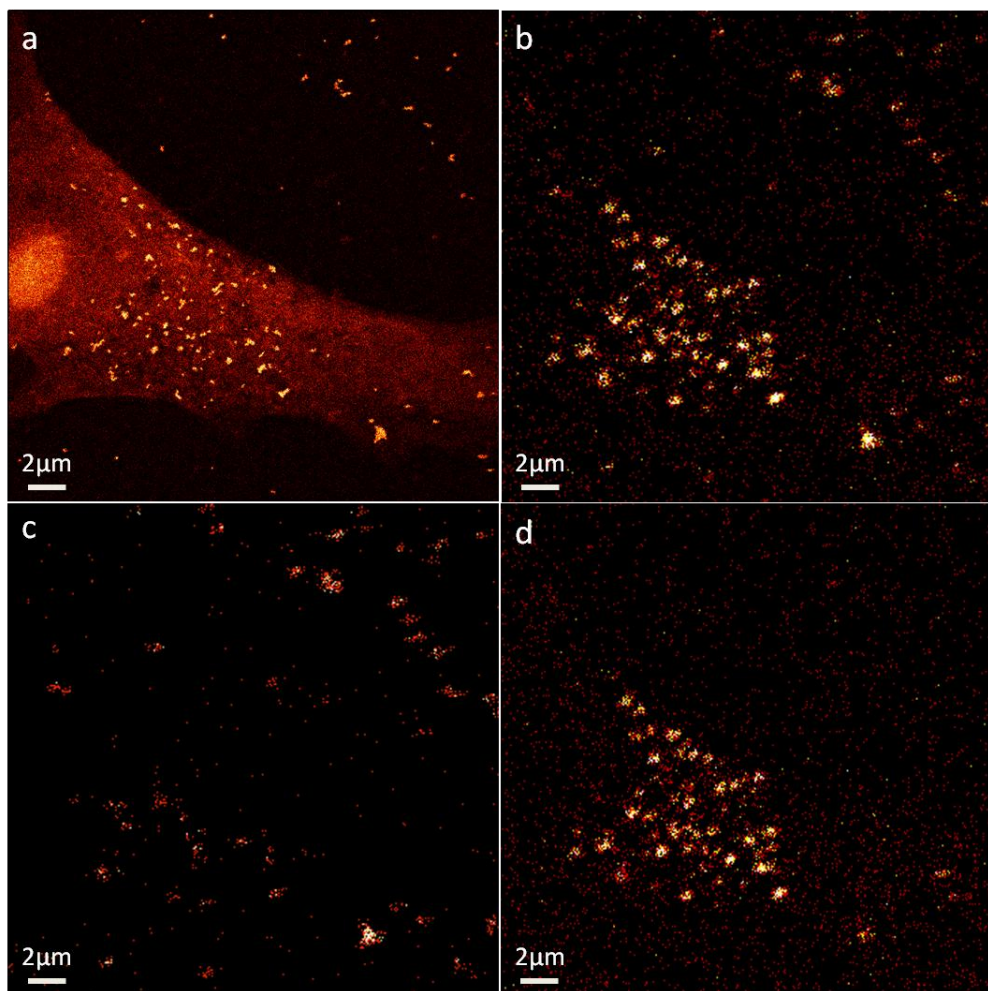


Figure 4.15 a) FSTM image of HeLa cell cultured in an environment of Au NPs; b) Total RBS Au image of HeLa cell cultured in an environment of Au NPs; c) Surface RBS Au image of HeLa cell cultured in an environment of Au NPs. d) Subsurface RBS Au image of HeLa cell cultured in an environment of Au NPs

Figure 4.15a is the FSTIM image for comparison. Figure 4.15b is the RBS image of the gold NPs using the total RBS gold data and, as expected, is similar to Figure 4.15a except for the poorer spatial resolution exhibited by RBS. Figure 4.15c is the RBS image of the NPs using only the backscattered ions from gold detected with low energy loss, i.e. from the surface, and Figure 4.15d shows the RBS image of the NPs using only the backscattered ions from gold detected with high energy loss, i.e. the NPs from within the cell. These images clearly differentiate between those NPs that have been internalised by the cell (as in Figure 4.15d), and those that are still on the surface (Figure 4.15c). It can be seen from Figure 4.15c that, as expected, surface NPs are relatively evenly distributed in the image. However, consistent with the idea that NPs usually gain entry into cells through endocytosis and are enclosed in endosomal or lysosomal vesicles [70, 71], the accumulation of intracellular NPs (as shown in Figure 4.15d) is not uniform within the cell, but appears to coincide with the perinuclear region, which is the location of late endosomal or lysosomal compartments within the cell^[72].

Further information can be obtained from the RBS results. For each NP or NP cluster, depth information can be extracted from the RBS data. Each NP or NP cluster can therefore be positionally located within the cell: High resolution (~25 nm) lateral information can be generated using FSTIM, and depth information can be generated from the RBS data. The energy resolution in our RBS detection system has been estimated at 24 keV, and if we use the typical stopping power of helium ions in a biological cell (192 KeV/um for 1.6 MeV helium ions) [56], then the depth resolution can be estimated as 62 nm. A 3D image of the NPs within the cell can then be constructed. Figure 4.16 shows

the FSTM image of the NP cell, using RBS depth information to colour code the depth of the NPs and NP clusters within the cell.

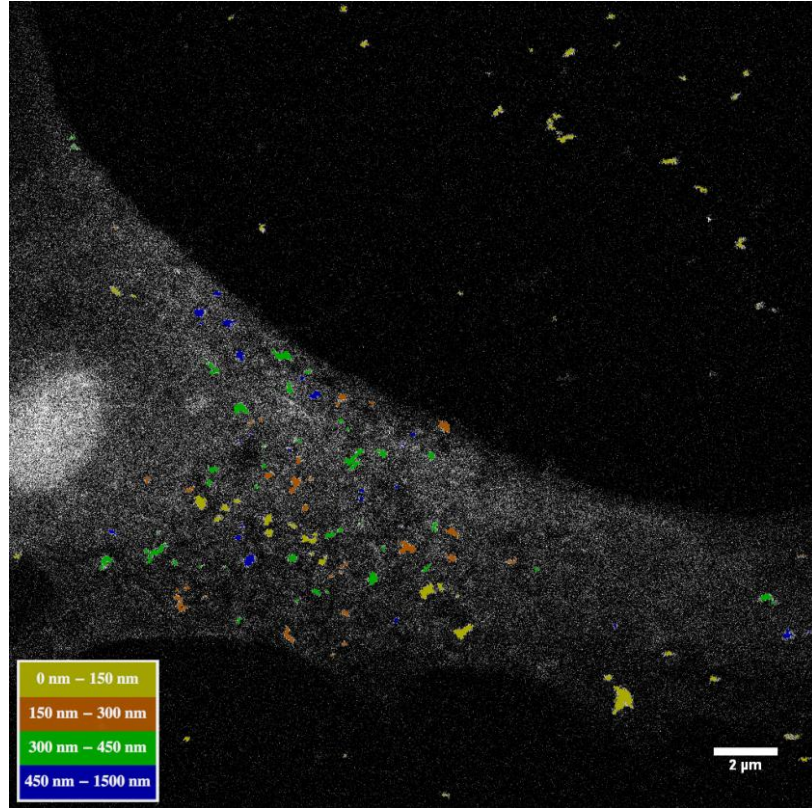


Figure 4.16 FSTM image of the NP cell, using RBS depth information to colour code the depth of the NPs and NP clusters within the cell. 0-150nm represents the surface NPs.

Quantifying the number of nanoparticles present within the cell:

The number of gold nanoparticles contained within the cell can be determined independently by the two techniques of RBS and FSTM.

Using RBS, the number of detected backscattered ions Y can be written as [52].

$$Y = \sigma \Omega Q N_t \quad \text{Eq 4.3}$$

Where Q is the total number of incident particles; σ is the RBS cross section (from equation 4.2) and Ω is the detector solid angle, which can be measured

from the detector geometry. By measuring Y, then the number of atoms per unit area Nt can be determined.

In the case of gold nanoparticles in a biological cell, if we know the number of gold atoms present per unit area inside the cell, and we know the area of the cell, then we can calculate the number of gold NPs corresponding to 100nm diameter gold spheres. Our RBS results indicate -1256 gold NPs are located within the cell.

Using FSTIM, we can resolve individual nanoparticles, and we therefore can measure the number of forward scattered ions from a single nanoparticle. If we then measure the total number of forward scattered ions from all NPs within the cell (and we do not need to differentiate between single NPs or NP clusters), then we can ascertain the total number of NPs. Using FSTIM, we measure 1341 gold NPs within the cell. Both sets of results are in good agreement. It should be noted that since we are considering nuclear scattering, then any effects due to chemical effects are negligible in both cases.

As a short summary for this section we have shown that, using a focused beam of fast helium ions, we can visualize the three dimensional location of gold NPs at lateral resolutions of ~25 nm, and depth resolutions ~60 nm in whole cells. Particles that have been assimilated into the cell can be resolved from particles residing on the surface, and using FSTIM and RBS we can ascertain the number of particles within the cell. The imaging times are relatively fast, with STIM and FSTIM taking around 15 minutes per cell, and RBS imaging around 1 hour.

Microscopy using MeV ions will enable a quantitative evaluation of particle accumulation in specific cellular organelles and therefore aid the prediction of

potential risks of toxicity, as well as providing useful insights on the mechanism of internalization and the intracellular bio-distribution of drugs [73]. The cell internalization of NPs is influenced by both nanoparticles properties such as size, shape or surface [74, 75] and cell types or cell phases [76]. The capability of quantifying AuNPs amounts in a whole cell is particularly useful for determining the efficacy of internalization process for drug targeting and delivery, which is a critical goal in the development of medical uses of NPs.

4.3 Discussions and future improvements

4.3.1 Discussions on Noise Reductions

At present, both STIM and RBS imaging employ silicon charged-particle detectors for energy spectroscopic analysis. Because such detectors produce very small output signals for each particle detected, it is essential that the input stage of the preamplifier contributes little noise. The requirement for low noise and stable sensitivity with these detectors is met by using a charge sensitive preamplifier with an FET (Field-Effect Transistor) input stage. The Ortec Charge sensitive preamplifiers, operating at room temperatures, are employed in both STIM and RBS measurements. Any noise originating from preamp input capacitance is minimised, because the preamplifiers are generally built as an integral assembly with minimum internal circuit capacitance. In general, the larger the detector, the higher the input capacitance and the higher the noise level. There are also sources of noise from cabling between the preamplifier and the detector, ground loops, and radio frequency pickup. To reduce the noise from these sources, the preamplifiers should be mounted as close as practically possible to the detector. However, in our case, since these

preamplifiers are mounted outside the vacuum chamber then the external capacitance and noise pickup from the cabling between the preamplifiers and the detectors are higher than they need be.

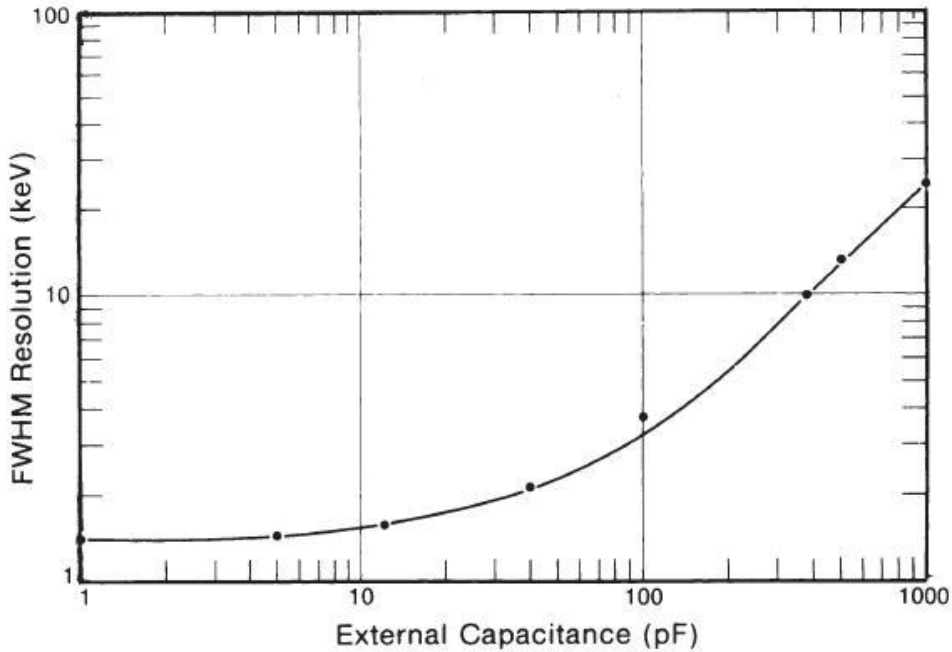


Figure 4.17 Noise Vs external capacitance for a typical ORTEC charge sensitive preamplifier.
Reproduced from [77].

Figure 4.17 is a graph showing the noise versus external capacitance for a typical Ortec charge sensitive preamplifier. In our practical setup, the microdot cable between the detector and the preamplifier is normally about 20 to 50 cm in length with a typical capacitance around 100pF per meter, resulting in an external capacitance of 20 to 50 pF. As the figure shows, the noise level can be reduced to two or three times lower than current value by controlling the external capacitance to be lower than 10 pF. The most practical way to further reduce the noise introduced by external capacitance is through an in-vacuum preamplifier, which we can place inside the vacuum just connected to the detector. This project is going on in CIBA at present.

Another important factor is the need for adequate signal grounding. Ground loops created by improperly designed or improperly grounded equipment can introduce serious noise to the particle detection system. In general, any possible electromagnetic interference can be picked up by the detector, amplifiers and cabling, adding extra noise to the final signal. This should be avoided as much as possible.

4.3.2 Three Dimensional STIM Tomography

STIM uses a focused MeV ion beam to generate images showing variations in sample areal density as viewed from a specific orientation. In the applications discussed above, this orientation is with the sample surface perpendicular to the incident ion beam and this gives a two dimensional view of the areal density. A three dimensional view of the sample can be obtained by taking two dimensional images at different angles and generating three dimensional models via imaging reconstruction techniques. One of the significant advantages of MeV proton and helium ions over the widely used electron beam is their capability to maintain the well focused resolution in a relatively thick sample. Three dimensional STIM tomography can exert this special advantage and give a three dimensional view of a relatively thick sample in a non destructive way. What's more, the extension of this technique to particle induced X ray emission (PIXE) can enable us to explore the three dimensional elemental content of microscopic samples such as biological cells. At present, these projects are under progress in CIBA.

4.4 Summary

Based on the newly built ion beam facility, high resolution STIM and FSTIM imaging have been carried out on whole biological cells.. Both techniques

exhibit sub-50 nm resolution and are capable of showing abundant sub-surface information of whole cells without the need for staining or sectioning. Fast helium ion STIM has been carried out on a single whole human liver cell, and compared to low energy helium ion microscopy. The techniques are complementary, in that low energy HIM can image the cell surface at high resolutions, whereas the highly penetrating STIM technique can image the cell internal structure. STIM, FSTIM and RBS have been combined together to study cell internalization of gold nanoparticles. In this study we demonstrated that 100 nm AuNPs internalised within a HeLa cell can be resolved three dimensionally and the amounts of AuNPs inside the whole cell can be quantified separately using RBS and FSTIM.

Chapter 5 High Resolution Proton Induced Fluorescence and its Applications

The MeV ion beam focusing performance achieved in the newly built cell imaging facility was discussed in detail in Chapter 3. Chapter 4 reviewed the STIM imaging technique and how it is being utilized in current biomedical research. This Chapter will discuss another emerging imaging technique that utilizes focused MeV proton beams called Proton Induced Fluorescence (PIF). PIF was initially proposed and developed in CIBA and still under development at present. Several PIF studies have been carried out in CIBA that demonstrate the techniques' potential and several promising application areas have been studied. This Chapter will present this work in detail, followed by some extensive discussions on the challenges and future developments of PIF.

5.1 Basic Principles

The term luminescence is used to describe cold body photon radiation in the infrared/visible/ultraviolet region of the spectrum. As such, luminescence usually arises from excited electrons associated with the outer shells of atoms or from the band structure of solids. The study of luminescence excited by photon or electron irradiation has a long history. Techniques such as cathodoluminescence using electrons and photoluminescence using photons for luminescence excitation are well established. Similarly to cathodoluminescence and photoluminescence, ionoluminescence is the term used for light emission in the infrared/visible/ultraviolet region excited by energetic ions. The literature of ionoluminescence is however less extensive; the study of ionoluminescence has concentrated mainly on crystals or bulk

luminescent materials based on either broad ion beam or microbeam [37, 78].

The theory of ionoluminescence and many pioneer materials studies were systematically covered in reference [78]. The ionoluminescence properties of many materials, including quartz, spinel, sapphire and diamond etc, were studied using microbeam. Ionoluminescence, in combination with other ion beam analysis techniques such as RBS or PIXE, has been used for material characterization [79-82].

5.1.1 Optical fluorescence

With reference to biological applications, fluorescence is typically used to describe light emission from those nanomaterials and molecules that are suitable for biological labeling. Biological optical fluorescence is an important technique in current bio-medical research. It mainly focuses on visible light emission from organic molecules, quantum dots and other types of fluorescent nano-materials. Here, we take the widely used organic molecules (fluorophores) as example to briefly discuss the basics of optical fluorescence. Fluorescence is the result of a three-stage process during light interaction with fluorescent materials. These three-stage processes are shown in Figure 5.1 as excitation, vibrational relaxation and internal conversion, and emission. When the light interacts with molecules, incident photons with specific wavelengths can be absorbed, resulting in the electrons transiting to a higher energy level, typically excited singlet states. Once excited, these electrons will undergo vibrational relaxation to the lowest energy level. The final process, which occurs over a relatively long time period of nanoseconds, is the emission of a longer wavelength photon, and return of the molecule to ground state. Due to the internal process like vibrational relaxation and internal conversion, the

emission wavelength is slightly longer than the excitation wavelength, which is the well-known stokes shift. This shift in wavelength is useful in fluorescence microscopy as it enables the separation of the excitation and emission light [83].

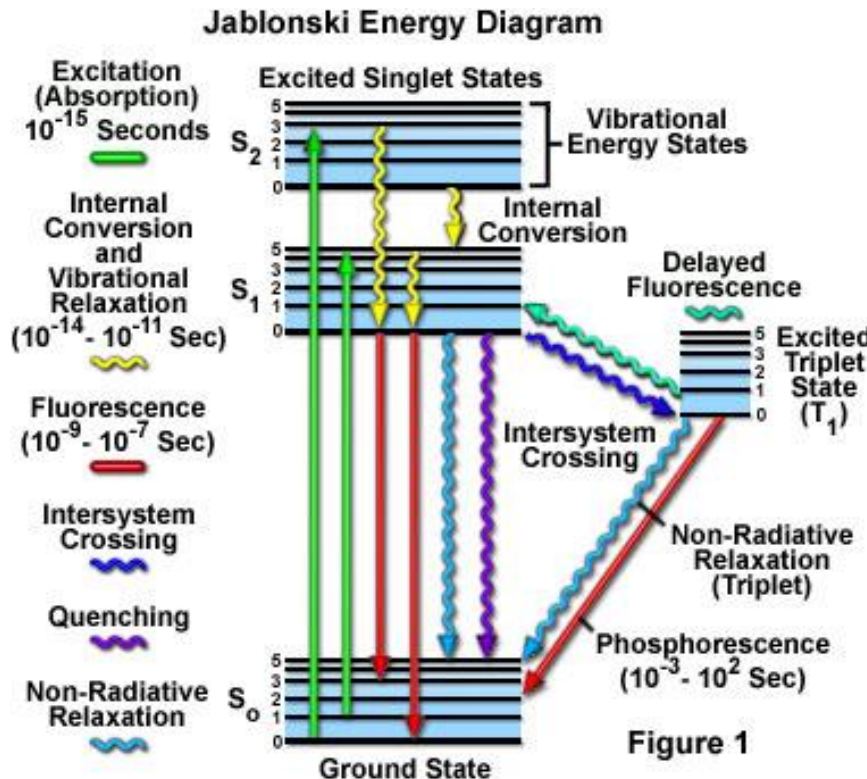


Figure 1

Figure 5.1 Fluorescence mechanism based on Jablonski energy diagram. Reproduced from ref [83].

5.1.2 Electron beam induced fluorescence - Cathodoluminescence

Cathodoluminescence (CL) is light emission resulting from irradiation of luminescent material by an electron beam. It has been widely explored and studied in many materials. Among all the types of Cathodoluminescence, luminescence from fluorophores or fluorescent nanomaterials, which can be used for biological labeling, is the least studied. Only several probes have been investigated using CL imaging of biological tissue and cells, these are green fluorescent protein and QDs [84], and organic molecules [85] and rare earth

doped nanophosphors [86]. In reference [85], cathodoluminescence from various organic materials have been studied using a scanning point electron beam. However, the final results showed most of the organic molecules (including several bio-used fluorophores) are unsuitable for the bio-cathodoluminescence application due to weak CL intensity and severe electron beam damage. Scientists in Mayo Clinical Cancer Center, Rochester, USA have tried CL from green fluorescence protein (powder), quantum dots, and FITC/Alexa. CL images on cells labeled with anti-human CD14-FITC/Alexa 656 have been captured with relatively good statistics [84]. Compared to organic molecules, rare-earth-doped nanophosphors showed a stronger CL signal, which might be useful for bio-application [86].

E-beam damage is a serious limitation for bio-applications of CL-EM. For biological samples which are electrically insulating, one of the most serious causes of e-beam damage is from sample charging effects [85]. The strong electric field induced by charging enhances ionization and therefore facilitates the destruction of molecules. Although metallic coatings can help in charge dissipation, the coating itself can cause a loss of fluorescence due to quenching. The other critical limitation is scattering of electron beam. As a result of large scattering, the high resolution of electron microscopy is only applicable to surface imaging or ultrathin slice. Since fluorescence labeling is mainly used for internal cellular structures deeply buried inside the cell, CL-EM has limited use in these applications.

5.1.3 Proton induced fluorescence

It has been shown that the luminescence properties of macromolecules are independent of the type of exciting radiation [87]. Similar to UV and electron

beams, proton beams have also been demonstrated to be able to excite luminescence from many types of materials. Proton induced fluorescence (PIF) from fluorescent molecules or nanomaterials has potential applications in bio-labeling imaging. As discussed in chapter 2, due to the mass mismatch between protons and electrons, interactions with material electrons does not cause significant deflection of primary protons. Compared to electron beams, MeV protons can have a deeper penetration while maintaining its resolution along the trajectory. Furthermore, charging effects are not a significant issue for MeV proton microscopy since the primary beam is transmitted through the sample.

The mechanism for light emission using PIF is that a proton beam, through interaction with the atomic electrons, can create atomic and molecular vacancies that are subsequently filled by electrons thereby releasing photons of a fixed wavelength. Apart from the primary proton beam, X-rays and δ -rays (secondary electrons) induced by primary beam can also excite fluorescence. Figure 5.2 shows possible energy transitions involved in the emission of fluorescence. X-rays produced as a result of electron transitions in the inner energy levels can also excite fluorescence. X-rays can propagate in a long way in a material, thus seriously effecting the final resolution. However, since the cross section for X-ray yield is negligible and the beam current used for PIF is small (less than 1 PA), the induced X-rays are extremely low for the beam current used in a typical PIF experiment. Therefore, compared to the primary beam and secondary electrons, fluorescence induced by X-rays is negligible.

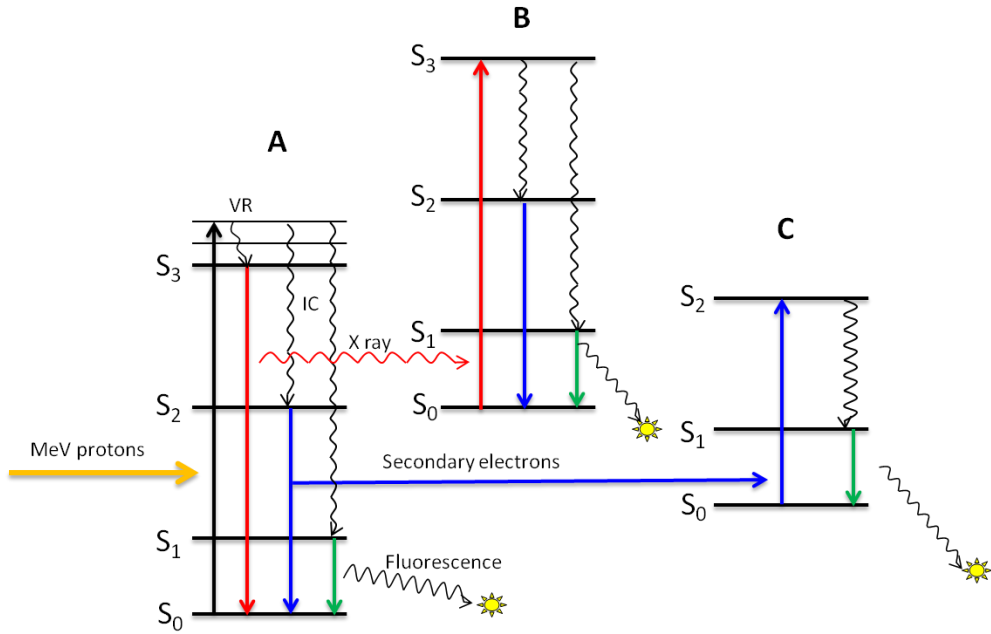


Figure 5.2 Schematic diagram of the possible energy transitions occurring from the excitation of a fluorophore by MeV protons. S-singlet states; VR-vibrational relaxations; IC-internal conversion.

The secondary electrons induced by the proton beam can play important role due to thier large yield. Monte Carlo calculations (see Figure 5.3) indicate that the primary delta-ray distribution profiles from the proton beam trajectory over the first 2 μm penetration into a material is essentially confined to the primary beam within a 10 nm diameter [43]. Thus, a focused MeV proton beam will pass through a biological cell with a straight trajectory retaining its original resolution. The PIF signal therefore is emitted from a cylindrical volume with the diameter only marginally greater than the size of the proton beam. At present MeV proton beams can be focused to a spot size of 30 nm, which indicates the resolution of current proton fluorescence could be sub-50 nm.

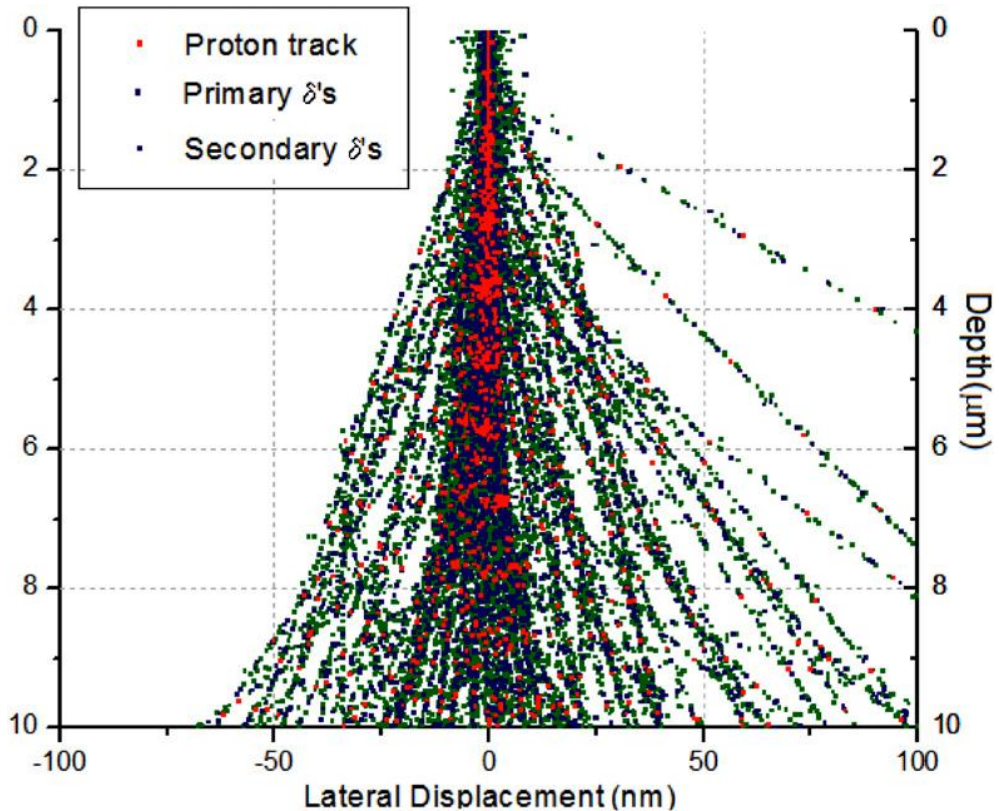


Figure 5.3 Simulation of δ -rays generated when 1000, 2 MeV protons impinge on 10 μm thick PMMA. Reproduced from ref [43].

5.2 Experimental explorations of PIF using in vacuum PMT

5.2.1 Experimental Setup

Just like confocal microscopy, fluorescence excited by a point proton beam is also very dim, requiring an optical system that utilizes highly sensitive photon detectors. For optical fluorescence microscopy, fluorescence detection normally employs a well designed microscopic system to guide the emission light to a high sensitive camera; while confocal like microscopes typically employ either photomultiplier tube (PMT) or avalanche photodiodes (APD) which are the most sensitive photon detectors at present. The PIF technique has many similarities to a confocal microscope system. In PIF a scanned focused proton beam is used instead of a laser to excite fluorescence. Our implementation of a PIF system utilized a PMT and APD for detection. One

additional requirement for PIF is that the end stage of proton microscope should be in a vacuum chamber. This requirement increases the complexity of optical system used for PIF.

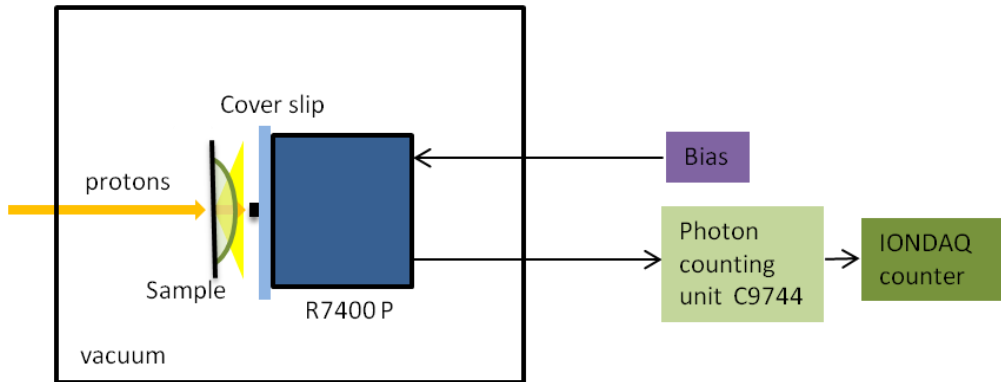


Figure 5.4 Schematic setup for R7400P used in a counting mode for proton fluorescence experiment.

The simplest approach to implement PIF imaging is to use a compact vacuum compatible PMT. A bare PMT “Hamamatsu R7400” is used in high speed single photon counting mode. The R7400P has a gain of 10^7 and a transit time of 5.4 ns when operating at a bias of 900 volts, which makes it quite suitable for multiscaler photon counting applications [88, 89]. It also has an integrated lens which can increase the light collection by two times over a bare tube. The R7400P was mounted on a three dimensional stage with a small (1mm square) silicon piece centered in front of the lens to stop the proton beam from hitting the lens. During the PIF experiments, the R7400P is moved to the center of the beam axis 3mm away from the sample surface, as shown in Figure 5.4. As the focused proton beam is scanning over the sample, the beam transmitted through the sample is blocked by the small silicon piece, while most of the emitted fluorescence light is collected by PMT. The output of PMT is connected to the photon counting unit C9744, which contains an amplifier and

discriminator to convert the single photoelectric pulses from the photomultiplier tube into a 5V TTL digital signal. Finally the signal is acquired by the IONDAQ data aquisition system [49]. The position of PMT can be adjusted in three dimensionals to maximize the light collection.

5.2.2 Proton fluorescence from fluorosphere

Several fluorescent materials which have an emission spectrum in the detection range have been tested with the R7400P PMT. Figure 5.5 shows proton fluorescence images from $1\text{ }\mu\text{m}$ fluorospheres, which is obtained at a proton current of around 50 K ions/s. For this beam setting, the protons can be focused to a sub-50 nm beam spot.

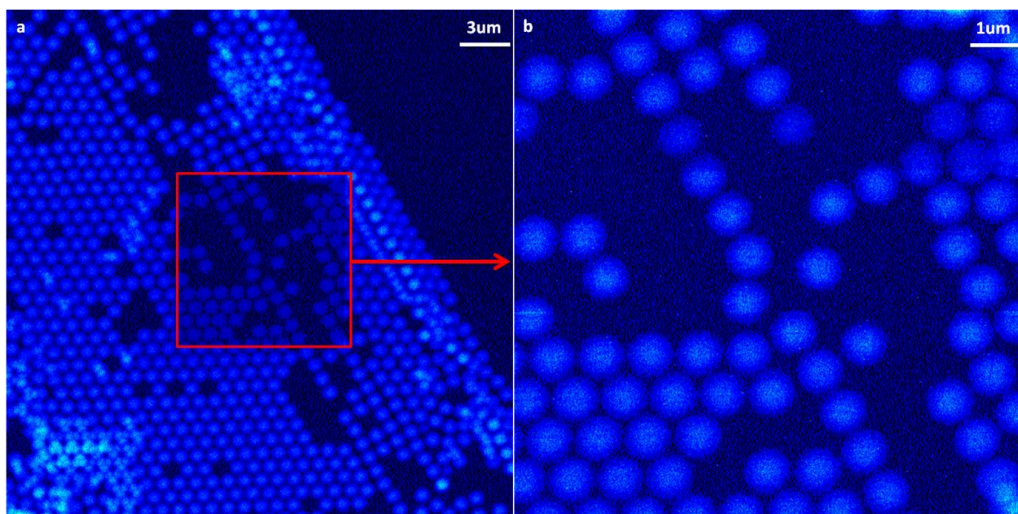


Figure 5.5 Proton induced fluorescence images of $1\text{ }\mu\text{m}$ fluorospheres. 2 MeV protons at a current of 30 K protons/s.

5.2.3 A Dapi-stained cell study

Several commonly used organic fluorophores have also been studied using the new cell imaging facility. Fluorophores are sometimes used alone, but generally they display their best performance when covalently bonded to a macromolecule, serving as a marker (or dye, or tag, or reporter) for affine or bioactive reagents (antibodies, peptides, nucleic acids). Fluorophores are

notably used to stain cells and tissues. Here we show an experimental study on a DAPI-stained cell using PIF and STIM.

The blue-fluorescent DAPI nucleic acid stain preferentially stains DNA. It appears to associate with AT clusters (Adenine and Thymine rich region inside DNA) in the Minor Groove (the narrow spaces between DNA twin helical strands). Binding of DAPI to DNA produces a ~20-fold fluorescence enhancement, apparently due to the displacement of water molecules from both DAPI and the Minor Groove. DAPI also binds to RNA, however in a different binding mode. The DAPI/RNA complex exhibits a longer-wavelength fluorescence emission maximum than the DAPI/DNA complex (~500 nm versus ~460 nm) and a quantum yield that is only about 20% as high DAPI/DNA complex[90].

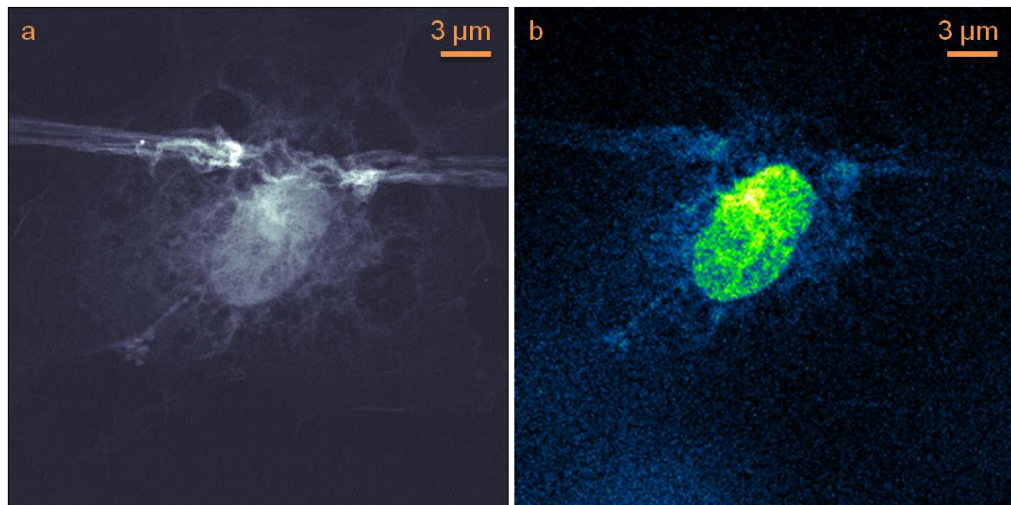


Figure 5.6 STIM and proton fluorescence images of the same cell stained with DAPI. a) 1.5 MeV direct helium ions STIM; b) 1.5 MeV proton fluorescence.

MRC5 cells stained with DAPI were firstly imaged using 1.5 MeV protons with a beam spot size of ~ 40 nm. Figure 5.6b shows the PIF image, which shows clear structures inside nucleus. In the experiment, the top cell surface is

facing the PMT. Since proton beams maintain a straight path as it penetrates into the cell, protons are able to excite fluorescence all along its trajectory. Although fluorescence emitted from structures deep inside the cell may be detected with a lower efficiency due to light scattering and absorption in the sample, the fluorescence image is still a map of the emission at all depths. Figure 5.6a displays the density map of the same cell obtained using 1.5 MeV helium ions. Most of the bright parts outside nucleus in fluorescence image actually correspond to the dense parts in STIM map. For regions inside the nucleus, the STIM map only shows a dense structure which could be the nucleolus or structure inside the nucleolus, while all other areas have a similar density. The PIF image reveals a lot small structures with various levels of brightness, which may be strongly related with DNA structures and distribution.

Through comparison with the STIM image, PIF imaging has a unique advantage and great potential for biomedical imaging. The STIM image can provide a high resolution structural view of the whole cell without staining; while, through labelling specific structures or organelles, PIF images are capable of providing images which highlight the specific labelled structures with superior contrast. For STIM, specific structures may be barely distinguishable due to either the detector resolution limit or the similar density properties of the structure with its surroundings. PIF imaging when used with STIM imaging is useful for identifying structures that do not show contrast in STIM images. In most cases, biologists not only want to know information of the specifically labelled structures, but also require a good image showing surrounding cell structure. Therefore, the combination of STIM and PIF is a

promising and powerful imaging tool for the investigation of biological problems.

5.2.4 Alexa 488 stained cell study

Non-enveloped human pathogens, enteroviruses are implicated in a range of diseases. But it is still unknown about the structures involved in the infectious entry pathway of these viruses. According to the previous studies from our collaborators, after its triggered internalization, echovirus 1 (EV1) follows a similar pathway with epidermal growth factor receptor (EGFR), which is a cell surface growth factor receptor. It has been showed that EV1 uses multivesicular endosomes (MVBs) for cell entry. However, the structural function of these MVBs remains to be unknown. The multivesicular endosomes have the size of around 200 nm to 500 nm, which is close to the diffraction limit of optical imaging. It is difficult to use conventional microscope to study it. Here a preliminary study was carried out using proton fluorescence to study the labelled endosomes in CIBA.

Cells in this study are from A549 lung carcinoma cell line, stained with endosomal markers and labeled with Alexa 488. The cells were scanned using a 2 MeV proton beam to collect PIF signals in the setup as shown in Figure 5.4. Figure 5.7 a and d show optical fluorescence images of the test cell, in which some dot like structures are observed with a poor resolution. Figure 5.7 b and e are proton induced fluorescence images from the same cell. Compared with Figure 5.7 a and d, all the dots like structures are clearly resolved with a much better resolution in the PIF images. Figure 5.7 c and e show high resolution alpha STIM images, which map the density of the cell. Many detailed structures can be resolved in the STIM images. Some dense structures

correlate with the dots in the size range of 200 nm and 500 nm highlighted in PIF images, which are probably the endosomes. The beam spot used in STIM imaging is around 30 nm and around 150 nm in proton fluorescence imaging, both of which are below optical diffraction limit.

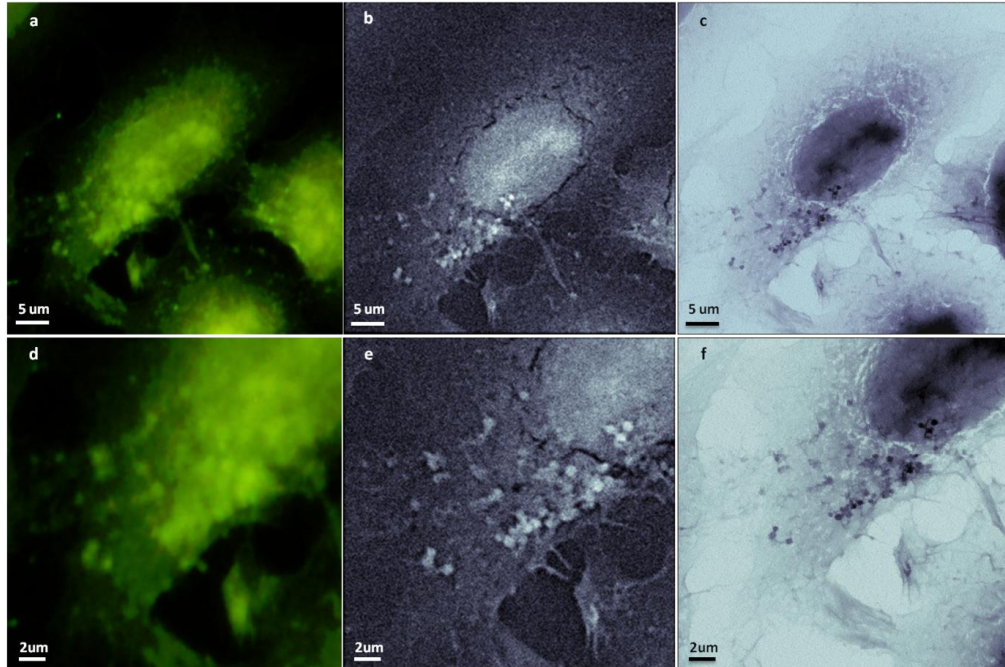


Figure 5.7 a) and d) are optical fluorescence images; b) and e) are proton induced fluorescence images; c) and f) are helium ions STIM images. Cells are from A549 lung carcinoma cell line, stained with endosomal markers, labeled with Alexa 488.

A lot of work needs to be done to optimize and improve these studies. For example, the fluorescence background is very high for this sample probably due to some remaining chemicals, which causes us to open the beam to get sufficient contrast but lower resolution. Further work will be carried out to improve sample preparation and remove these background contaminations. Besides, the optical fluorescence does not show very good specificity of fluorescence labelling, which probably is due to the drying process. However, the preliminary results of this study successfully show the potentials of using PIF to study the labelled endosomes. With achieved resolution well below

diffraction limit, PIF is able to resolve endosomes. By correlation with STIM image, the surrounding structures around endosomes can be showed clearly. All these information, which is extremely difficult to obtain using current optical microscopy and electron microscopy, is probably helpful to study the structures, distributions and intra-cellular interaction of endosomes.

5.4 Discussions, Challenges and future studies

5.4.1 Challenges in sample preparation

Sample preparation is always an important step which greatly affects the experimental results. For PIF, it is critically important. There are several key challenges in the sample preparation process for PIF. The First challenge is how one maintains the emission efficiency of the fluorescent materials during sample preparation and therefore not effect the sensitivity of PIF. Most fluorescent probes used in biological studies are tested and optimized in the liquid state. When used for PIF, the stained biological specimen will have to be dried using some method to satisfy the requirement for observation in vacuum. During this drying process, the emission efficiency of many fluorescent probes can be reduced to some extent. Work has been carried out in CIBA to optimize the drying protocols to maintain the fluorescence output during the drying process. The second challenge is the preservation of specificity of fluorescence. Specificity is the greatest advantage of optical fluorescence microscopy. There are lots of fluorescent probes which can be linked or labelled to a specific cellular structure. However, the experiments in CIBA have showed that the binding of these probes can be damaged to some extent during the drying process, which will greatly reduce the specificity of the probe. Sample preparation tests are on going to optimize the sample

preparation procedures in order to maintain the specificity. Another challenge is contamination introduced during the sample preparation. Since a lot of crystals can emit fluorescence under MeV ion beam excitation, any contaminations remaining on the sample can increase the background noise or even completely ruin the signal to noise ratio. If the optical wavelength emitted by the contamination is different from the fluorescent signal from the probe, this problem can be avoided by differentiating them with optical filters placed before the detector.

5.4.2 Challenges due to the beam

PIF is an emerging technique in the broader field of ionoluminescence that has promising applications in cell and tissue imaging. However, compared to traditional research on ionoluminescence, it requires the study of nano-materials (sub 100 nm fluorescent materials or molecules) using a finely focused proton beam at a low beam current. The energy of MeV proton beam is much higher than that of all the chemical bonds. As protons penetrate samples, it is highly probable that many chemical bonds are damaged due to the interaction of material electrons with protons or secondary electrons. Here for biological cells, it is more complicated due to the complexity of various cells and dyes. Since the sample has already been dried before proton irradiation, breaking of the bonds should not affect the specificity. However, it may affect the intensity of the fluorescence emission due to the damage of dye-cell bonds or even dye's own bonds. This can be problematic for fluorophores like DAPI, which can only show strong fluorescence when bound to cell structures. Any damage to the bonding could cause the decrease of the emission signals (bleaching). Even for fluorophores that have a strong

fluorescence emission without bonding to any structure, the damage of dye's internal chemical bonds may also cause a serious reduction in the fluorescence signal.

5.4.2 Future work on proton fluorescence

Preliminary studies have shown that there is great potential for PIF to play a significant role in biological research. However, a lot of work is needed to further optimize this technique.

External PMT detection based on reflective objective lens

Another approach for performing PIF is based on an external PMT module and microscope optical system. The motivation for using an external PMT with an optical system is that a high sensitivity cooled PMT module can be used and different optical components (eg. Band-pass filters, spectrometer) can be inserted into optical path to further analyze the PIF. For our external PIF system we used a Hamamatsu H7422 module, which incorporates a GaAs or GaAsP cathode PMT, a thermoelectric cooler, and the high voltage power supply. Thermoelectric coolers improve the S/N (signal to noise ratio) of PMT measurements because of the reduction in thermal electrons, which are emitted from PMT photocathode, and minimization of external noise by a built-in electrostatic and magnetic shield.

One challenge with such a setup is that the transmitted beam will hit the objective lens in the chamber which not only damages the objective but also introduces background noise by ionoluminescence from lens. A special objective, called reflective microscope objective, is a good solution to solve this problem. Figure 5.8a shows, a typical optical setup, collimated light passes through the aperture hole in the primary mirror to the secondary mirror.

The second mirror reflects and diverges the beam to fill the primary mirror. The primary mirror focuses the beam to the focal point. In our case for fluorescence detection, when a focused proton beam is scanning over the sample, fluorescence light emitted from the focal point can be collected and collimated to the microscope system, as shown in Figure 5.8b. The H7422 is mounted on the microscope camera port to detect the collimated fluorescence light, and the transmitted beam is blocked by the back of secondary mirror which will not damage the objective.

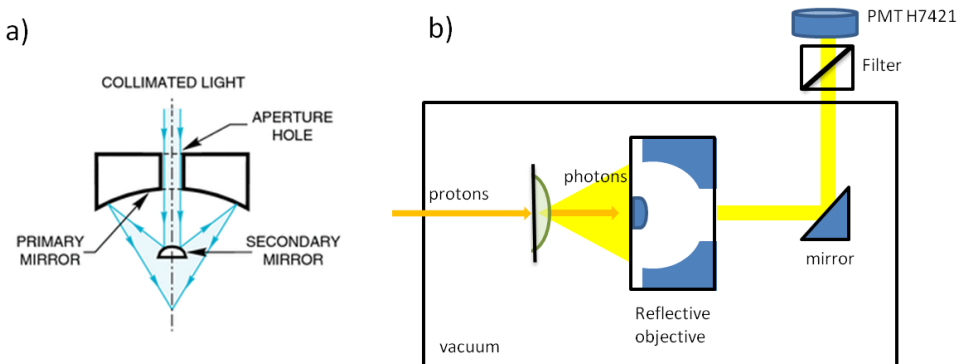


Figure 5.8 a) Schematic principle of reflective objective lens; b) Schematic setup for the fluorescence detection using external PMT and reflective objective.

The system showed in Figure 5.8b is similar with the fluorescence detection system employed in a Confocal microscope except a reflective objective is used instead of an oil immersion objective lens. Considering the similarity of scanning proton fluorescence and scanning confocal, this setup is quite promising. However, there are two limitations for this setup which currently makes it difficult to obtain a good fluorescence image. Firstly, unlike the confocal microscope, oil immersion can not be employed in the proton fluorescence detection due to the vacuum environment. Furthermore, the commercially available reflective objective lenses have long working distance,

especially for low magnification objectives, which results in a small solid angle (Numerical aperture). In our experiments, we tried two reflective objectives from Newport (50105-02, 15X, infinite BFL and 50102-02, 36X, infinite BFL), which have a working distance of 24 mm and 10.4 mm, NA of 0.4 and 0.52 respectively. Secondly, the special configuration of a reflective objective gives a much smaller depth of focus than normal objective. Although the datasheet does not provide detailed information on this, it is one of the critical specifications for a reflective objective. Such a small depth of focus requires more precise alignment and higher emission intensity in the thinner focal plane, which greatly increases the difficulty in obtaining a high quality image. Ideally what is required is a customized objective lens which has a relatively high NA, small working distance and large depth of focus with a small beam stopper in the centre to block the transmitted protons.

External PMT detection based on a curve mirror collection system

In order to overcome the previously mentioned problems and collect a sufficient amount of fluorescence light for an external PMT to form a relatively high S/N image, a curve mirror collection system was proposed. Instead of using a reflective objective, a mirror (spherical or parabolic) is mounted behind the sample as shown in Figure 5.9 to collect the PIF. The proton beam can go through the centre hole in the mirror, which not only helps to avoid the primary beam from hitting the mirror, but also enable a simultaneous STIM imaging when the beam current is very low. The curve mirror is designed to collect the fluorescence and focus the emitted light onto a light guide tube or a fiber coupler, which will help to guide the light out of

vacuum chamber via a vacuum optical feedthrough. Outside the vacuum, a cooled PMT with high quantum efficiency over a wide spectral range such as the H7421 can be directly connected or connected after an optical filter. A high sensitivity spectrometer could also be attached in the place of PMT to analyze the PIF spectrum. The advantage of this design over the current setup is that the curve mirror could be designed to cover most of the emitted fluorescence from the back with a solid angle approaching 2π . Compared to the 15x reflective objective which has a 24 mm working distance and mirror diameter, the solid angle can be improved by around 10 times (NA of 15x reflective is 0.4, which corresponds to a solid angle of 0.2π) .

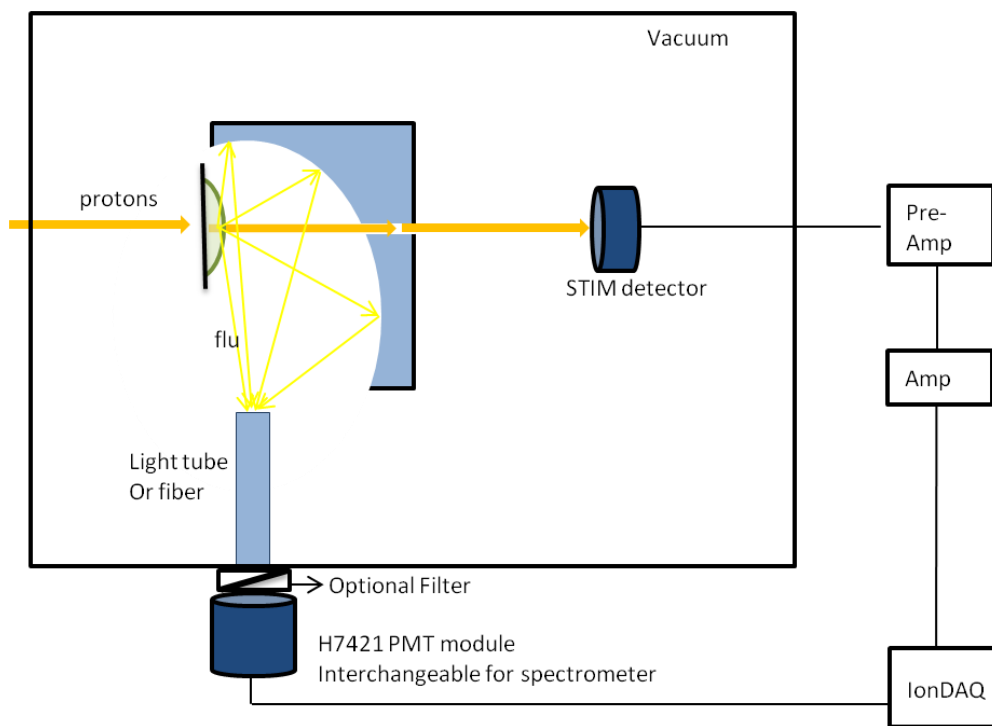


Figure 5.9 Possible setup for curve mirror based proton fluorescence detection system.

Apart from this, as an emerging technique, a lot of fundamental studies need to be carried out both theoretically and experimentally to provide systematic information. For example, the auto fluorescence under proton beam varies

greatly for different cell types, therefore, when using a specific cell line, the auto fluorescence needs to be detected and the spectrum needs to be analyzed as a reference. Some dyes behave better under proton beam irradiation, which possibly results from a higher proton irradiation resistance of their chemical properties. To further explore this, a systematic study of all the commonly used dyes under proton beam irradiation is required.

Up to now, most of the cell studies with PIF have been performed using organic dyes. However, due to recent developments in nanotechnology, a lot of fluorescent nano-nanomaterials, such as, quantum dots and fluorescent nano phosphors, have been developed and commercialized. With better stability under photons and electron beams, they most likely will also behave better under proton beam irradiation. Chapter 4 has showed that helium ions STIM has high contrast for density imaging. When used for fluorescence, helium ions seem to quench many organic dyes very fast in our current experiment results. This is understandable because helium ions have much higher rate of energy deposition. However, some fluorescent materials, especially the above-mentioned fluorescent nanoparticles, may possibly exhibit less response to the energy deposition. In that case, high resolution helium ions STIM and helium ions fluorescence can be obtained in one single experiment, which will be much more convenient. The quenching properties of these materials under both protons and helium ions need to be further investigated.

A finely focused beam with high beam current is quite important for PIF experiments. The resolution of PIF image is determined by the primary beam spot and surrounding secondary electrons. Therefore, better focusing of the beam will give a better resolution. The beam brightness is a very important

parameter that relates to the ultimate beam spot that can be achieved. At present, there is a project to improve the brightness of current RF ion source used in our accelerator.

5.5 Summary

In Summary, PIF is an emerging technique that has been discussed in detail in this chapter. Compared to optical fluorescence and electron fluorescence, PIF is superior for high resolution imaging on relatively thick biological specimens. Several PIF imaging results based on the current experimental setup were shown to demonstrate the capabilities of PIF. At present, PIF is still under development. Several challenges, improvements and some future work were also discussed.

Chapter 6 Conclusion

Currently there is no well developed imaging technique that can achieve nanometre resolution for thick samples such as whole cells. Nuclear microscopy using MeV protons and helium ions has demonstrated some unique advantages for imaging thick samples mainly due to the property that MeV ions are able to maintain their straight trajectory and resolution during penetration through a thick biological specimen.

The theory, techniques and capabilities of nuclear microscopy using MeV protons and helium ions are presented in this thesis. A dedicated bio-imaging beam line was built up in CIBA specifically for cell and tissue imaging using MeV protons and helium ions, and the design and construction of this beam line is discussed in detail in chapter 3. The performance of the system was demonstrated and some further improvements to the system are also proposed.

To summarize, the specifications of the new bio-imaging system are:

1. To test the focusing capabilities of the Oxford Triplet configuration, with different spacings between the first lens and the doublet, and the high excitation double cross-over Russian quadruplet.
2. The ability to focus MeV protons and helium ions to 25 nm spot size.
3. The integration of sub-50 nm STIM imaging and FSTIM imaging, sub-100 nm PIF imaging, secondary electron imaging, and sub 500 nm RBS imaging.
4. The integration of optical fluorescence microscopy.
5. The implementation of the data acquisition system IONDAQ, supporting PHA, TTL and AI imaging modes and includes Pixel Normalization function.

In this thesis we have presented high resolution STIM, FSTIM and PIF imaging techniques in detail including their physical principles, experimental implementations, imaging applications and some challenges. STIM and FSTIM imaging has been optimized with the capability of imaging buried structures in a whole cell at a spatial resolution of sub-50 nm. When STIM is utilized in conjunction with low energy Helium Ion Microscopy, both sub surface structures and surface structures can be imaged at nanometre resolutions with high contrast using helium ions. The thesis also describes a relevant biological application where STIM, FSTIM and RBS are used together to image AuNPs internalized into a Hela cell. Using these techniques, the AuNPs distribution was visualized three dimensionally and the number of nanoparticles calculated. The development of high resolution PIF imaging is also presented in the thesis in chapter 5. The results show the great potential of using PIF to image specifically labeled structures at a sub-100 nm resolution. Many projects are still ongoing or planned in CIBA to further develop these imaging techniques so that they can be applied to biomedical research. These projects include:

1. Improvement of ion source brightness. Once the brightness is improved 10 times or more than the current value, it is feasible to focus the beam down to 10 nm or even lower.
2. Three dimensional STIM tomography. By tilting the sample and collecting the image projections from continuous angles, three dimensional structural images can be reconstructed from all the image projections.

3. Curved mirror proton fluorescence detection system. A curved mirror system can increase the solid angle for photon detection and allow for the use of an external high sensitivity PMT outside the vacuum chamber.
4. In vacuum preamplifier or cooling integrated preamplifier for STIM to reduce noise and improve the energy resolution.
5. Proton induced fluorescence from fluorescent nanomaterials such as quantum dots or fluorescent nanophosphor. Many of these nanomaterials (mostly inorganic materials) show higher brightness and photostability under optical excitation.

Although nuclear microscopy using MeV protons and helium ions has a shorter history compared with optical and electron microscopies, this thesis has indicated that it has unique advantages over these commonly used microscopy techniques. The widespread applications and commercialization of microscopy using MeV protons or helium ions might still require a lot of technical advancements and may take a long time. However, I do believe that MeV proton and helium ion microscopy is an important branch of the field of microscopy. It is anticipated that it will cause a paradigm shift in high resolution whole cell imaging. I hope the work in this thesis can pave the way for these future developments.

Bibliography

1. Neice, A., *Chapter 3 - Methods and Limitations of Subwavelength Imaging*, in *Advances in Imaging and Electron Physics*, W.H. Peter, Editor 2010, Elsevier. p. 117-140.
2. Oshikane, Y., et al., *Observation of nanostructure by scanning near-field optical microscope with small sphere probe*. Science and Technology of Advanced Materials, 2007. **8**(3): p. 181.
3. Cummings JR, F.T., Davidson MW, *Specialized Microscopy Techniques - Near Field Scanning Optical Microscopy*. Olympus Microscopy Resource Center, 2007.
4. Lewis, A., et al., *Near-field scanning optical microscopy in cell biology*. Trends in Cell Biology, 1999. **9**(2): p. 70-73.
5. Hartschuh, A., *Tip-Enhanced Near-Field Optical Microscopy*. Angewandte Chemie International Edition, 2008. **47**(43): p. 8178-8191.
6. Hell, S.W., *Far-Field Optical Nanoscopy*. Science, 2007. **316**(5828): p. 1153-1158.
7. Hell, S.W., *Microscopy and its focal switch*. Nat Meth, 2009. **6**(1): p. 24-32.
8. Langhorst, M.F., J. Schaffer, and B. Goetze, *Structure brings clarity: Structured illumination microscopy in cell biology*. Biotechnology Journal, 2009. **4**(6): p. 858-865.
9. Gustafsson, M.G.L., *Nonlinear structured-illumination microscopy: Wide-field fluorescence imaging with theoretically unlimited resolution*. Proceedings of the National Academy of Sciences of the United States of America, 2005. **102**(37): p. 13081-13086.
10. Huang, B., M. Bates, and X. Zhuang, *Super-Resolution Fluorescence Microscopy*. Annual Review of Biochemistry, 2009. **78**(1): p. 993-1016.
11. Betzig, E., et al., *Imaging Intracellular Fluorescent Proteins at Nanometer Resolution*. Science, 2006. **313**(5793): p. 1642-1645.
12. Rust, M.J., M. Bates, and X. Zhuang, *Sub-diffraction-limit imaging by stochastic optical reconstruction microscopy (STORM)*. Nat Meth, 2006. **3**(10): p. 793-796.
13. Ji, N., et al., *Advances in the speed and resolution of light microscopy*. Current Opinion in Neurobiology, 2008. **18**(6): p. 605-616.
14. Koster, A.J. and J. Klumperman, *Electron microscopy in cell biology: integrating structure and function*. Nature Cell Biology, 2003: p. SS6-SS10.
15. Lucic, V., F. Forster, and W. Baumeister, *Structural studies by electron tomography: From cells to molecules*. Annual Review of Biochemistry, 2005. **74**: p. 833-865.
16. Barcena, M. and A.J. Koster, *Electron tomography in life science*. Seminars in Cell & Developmental Biology, 2009. **20**(8): p. 920-930.
17. Höög, J.L., et al., *Organization of Interphase Microtubules in Fission Yeast Analyzed by Electron Tomography*. Developmental Cell, 2007. **12**(3): p. 349-361.
18. Brandt, F., et al., *The Native 3D Organization of Bacterial Polysomes*. Cell, 2009. **136**(2): p. 261-271.

19. Schmid, M.F., et al., *Structure of Halothiobacillus neapolitanus Carboxysomes by Cryo-electron Tomography*. Journal of Molecular Biology, 2006. **364**(3): p. 526-535.
20. Iancu, C.V., et al., *The Structure of Isolated Synechococcus Strain WH8102 Carboxysomes as Revealed by Electron Cryotomography*. Journal of Molecular Biology, 2007. **372**(3): p. 764-773.
21. Nicastro, D., et al., *Cryo-electron Tomography of Neurospora Mitochondria*. Journal of Structural Biology, 2000. **129**(1): p. 48-56.
22. Strauss, M., et al., *Dimer ribbons of ATP synthase shape the inner mitochondrial membrane*. EMBO J, 2008. **27**(7): p. 1154-1160.
23. Peckys, D.B. and N. de Jonge, *Visualizing Gold Nanoparticle Uptake in Live Cells with Liquid Scanning Transmission Electron Microscopy*. Nano Letters, 2011. **11**(4): p. 1733-1738.
24. de Jonge, N., et al., *Electron microscopy of whole cells in liquid with nanometer resolution*. Proceedings of the National Academy of Sciences, 2009.
25. Peckys, D.B., et al., *Nanoscale Imaging of Whole Cells Using a Liquid Enclosure and a Scanning Transmission Electron Microscope*. PLoS ONE, 2009. **4**(12): p. e8214.
26. Henderson, R., *The potential and limitations of neutrons, electrons and X-rays for atomic resolution microscopy of unstained biological molecules*. Quarterly Reviews of Biophysics, 1995. **28**(02): p. 171-193.
27. Le Gros, M.A., G. McDermott, and C.A. Larabell, *X-ray tomography of whole cells*. Current Opinion in Structural Biology, 2005. **15**(5): p. 593-600.
28. Jiang, H., et al., *Quantitative 3D imaging of whole, unstained cells by using X-ray diffraction microscopy*. Proceedings of the National Academy of Sciences, 2010. **107**(25): p. 11234-11239.
29. Larabell, C.A. and M.A. Le Gros, *X-ray Tomography Generates 3-D Reconstructions of the Yeast, Saccharomyces cerevisiae, at 60-nm Resolution*. Molecular Biology of the Cell, 2004. **15**(3): p. 957-962.
30. Huang, X., et al., *Soft X-Ray Diffraction Microscopy of a Frozen Hydrated Yeast Cell*. Physical Review Letters, 2009. **103**(19): p. 198101.
31. Cormack, A.M. and A.M. Koehler, *Quantitative proton tomography: preliminary experiments*. Physics in Medicine and Biology, 1976. **21**(4): p. 560.
32. Russell, P.E. and F.A. Stevie, *Focused Ion Beam (FIB) Microscopy and Technology*. Microscopy and Microanalysis, 2002. **8**(SupplementS02): p. 558-559.
33. Company, F., *Focused ion beam technology, capabilities and applications*. 2006.
34. Scipioni, L., et al., *Helium ion microscope*. Advanced Materials & Processes, 2008. **166**(6): p. 27-30.
35. Thompson, W.B., et al., *The helium ion microscope for high resolution imaging, materials analysis and FA applications*. Ipfa 2008: Proceedings of the 15th International Symposium on the Physical & Failure Analysis of Integrated Circuits, ed. C.L. Gan, et al.2008. 36-41.

36. Cohen-Tanugi, D. and N. Yao, *Superior imaging resolution in scanning helium-ion microscopy: A look at beam-sample interactions*. Journal of Applied Physics, 2008. **104**(6).
37. Mark B.H. Breese, D.N.J., Philip J.C. King, *Materials analysis using a nuclear microprobe* 1996, New York: John Wiley and Sons.
38. Michelet-Habchi, C., et al., *3D imaging of microscopic structures using a proton beam*. Nuclear Science, IEEE Transactions on, 2005. **52**(3): p. 612-617.
39. Schwertner, M., et al., *Scanning transmission ion micro-tomography (STIM-T) of biological specimens*. Ultramicroscopy, 2006. **106**(7): p. 574-581.
40. Watt, F., et al., *The National University of Singapore high energy ion nano-probe facility: Performance tests*. Nuclear Instruments and Methods in Physics Research Section B: Beam Interactions with Materials and Atoms, 2003. **210**: p. 14-20.
41. Minqin, R., et al., *Nano-imaging of single cells using STIM*. Nuclear Instruments and Methods in Physics Research Section B: Beam Interactions with Materials and Atoms, 2007. **260**(1): p. 124-129.
42. Watt, F., et al., *Imaging of single cells and tissue using MeV ions*. Nuclear Instruments and Methods in Physics Research Section B: Beam Interactions with Materials and Atoms, 2009. **267**(12-13): p. 2113-2116.
43. Udalagama, C.N.B., A.A. Bettoli, and F. Watt. *A Monte Carlo study of the extent of proximity effects in e-beam and p-beam writing of PMMA*. in *10th International Conference on Nuclear Microprobe Technology and Applications held in Conjunction with the 2nd International Workshop on Proton Beam Writing*. 2006. Singapore, SINGAPORE.
44. Ziegler, J.F. SRIM. <http://www.srim.org/>; Available from: <http://www.srim.org/>.
45. Udalagama, C., A.A. Bettoli, and F. Watt, *Stochastic spatial energy deposition profiles for MeV protons and keV electrons*. Physical Review B, 2009. **80**(22): p. 224107.
46. Watt, F. and G.W. Grime, *Principles and Applications of High-energy Ion Microbeams* 1987: Adam Hilger, Bristol.
47. Grime, G.W. and F. Watt, *Beam Optics of Quadrupole Probe-forming Systems* 1984: Adam Hilger Ltd, Bristol.
48. *Particle Beam Optics lab 2.0*, 2007, AccelSoft Inc.
49. Bettoli, A.A., C. Udalagama, and F. Watt, *A new data acquisition and imaging system for nuclear microscopy based on a Field Programmable Gate Array card*. Nuclear Instruments and Methods in Physics Research Section B: Beam Interactions with Materials and Atoms, 2009. **267**(12-13): p. 2069-2072.
50. Watt, F., et al., *The Singapore high resolution single cell imaging facility*. Nuclear Instruments and Methods in Physics Research Section B: Beam Interactions with Materials and Atoms, 2011. **269**(20): p. 2168-2174.
51. Udalagama, C.N.B., et al., *An automatic beam focusing system for MeV protons*. Nuclear Instruments and Methods in Physics Research Section B: Beam Interactions with Materials and Atoms, 2005. **231**(1-4): p. 389-393.

52. Chu, W.-K., *Backscattering Spectrometry* 1978, New York: Acamedic Press, Inc
53. Messenger, G.C., *A summary review of displacement damage from high energy radiation in silicon semiconductors and semiconductor devices*. Nuclear Science, IEEE Transactions on, 1992. **39**(3): p. 468-473.
54. Ortec *Introduction to charged particle detectors*. 2010.
55. Postek, M.T., et al., *Helium ion microscopy: a new technique for semiconductor metrology and Nanotechnology*, in *Frontiers of Characterization and Metrology for Nanoelectronics: 2007*, D.G. Seiler, et al., Editors. 2007. p. 161-167.
56. Biersack, J.F.Z.a.J.P., *The Monte Carle program TRIM*, in <http://www.srim.org>.
57. Tan, T.M.C., K.H. Sit, and K.P. Wong, *Kinetics of sulfate conjugation in extracts of human-fetal liver-cells in culture*. Biochemical Pharmacology, 1988. **37**(24): p. 4629-4633.
58. Physics reference data. Available from: <http://physics.nist.gov/PhysRefData/Star/Text/ASTAR.html>.
59. Petros, R.A. and J.M. DeSimone, *Strategies in the design of nanoparticles for therapeutic applications*. Nat Rev Drug Discov, 2010. **9**(8): p. 615-627.
60. Sperling, R.A., et al., *Biological applications of gold nanoparticles*. Chemical Society Reviews, 2008. **37**(9): p. 1896-1908.
61. Ghosh, P., et al., *Gold nanoparticles in delivery applications*. Advanced Drug Delivery Reviews, 2008. **60**(11): p. 1307-1315.
62. Weissleder, R. and M.J. Pittet, *Imaging in the era of molecular oncology*. Nature, 2008. **452**(7187): p. 580-589.
63. Lal, S., S.E. Clare, and N.J. Halas, *Nanoshell-Enabled Photothermal Cancer Therapy: Impending Clinical Impact*. Accounts of Chemical Research, 2008. **41**(12): p. 1842-1851.
64. Cho, K., et al., *Therapeutic Nanoparticles for Drug Delivery in Cancer*. Clinical Cancer Research, 2008. **14**(5): p. 1310-1316.
65. Farokhzad, O.C., et al., *Targeted nanoparticle-aptamer bioconjugates for cancer chemotherapy in vivo*. Proceedings of the National Academy of Sciences, 2006. **103**(16): p. 6315-6320.
66. Stone, V. and K. Donaldson, *Nanotoxicology: Signs of stress*. Nat Nano, 2006. **1**(1): p. 23-24.
67. Tetard, L., et al., *Imaging nanoparticles in cells by nanomechanical holography*. Nat Nano, 2008. **3**(8): p. 501-505.
68. Shekhawat, G.S. and V.P. Dravid, *Nanoscale Imaging of Buried Structures via Scanning Near-Field Ultrasound Holography*. Science, 2005. **310**(5745): p. 89-92.
69. Chen, X., et al., *Whole-Cell Imaging at Nanometer Resolutions Using Fast and Slow Focused Helium Ions*. Biophysical Journal, 2011. **101**(7): p. 1788-1793.
70. Iversen, T.-G., T. Skotland, and K. Sandvig, *Endocytosis and intracellular transport of nanoparticles: Present knowledge and need for future studies*. Nano Today, 2011. **6**(2): p. 176-185.
71. Lévy, R., et al., *Gold nanoparticles delivery in mammalian live cells: a critical review*. 20102010.

72. Hao, X., et al., *Caveolae-mediated endocytosis of biocompatible gold nanoparticles in living Hela cells*. Journal of Physics: Condensed Matter, 2012. **24**(16): p. 164207.
73. Khlebtsov, N. and L. Dykman, *Biodistribution and toxicity of engineered gold nanoparticles: a review of in vitro and in vivo studies*. Chemical Society Reviews, 2011. **40**(3): p. 1647-1671.
74. Lundqvist, M., et al., *Nanoparticle size and surface properties determine the protein corona with possible implications for biological impacts*. Proceedings of the National Academy of Sciences, 2008. **105**(38): p. 14265-14270.
75. Chithrani, B.D., A.A. Ghazani, and W.C.W. Chan, *Determining the Size and Shape Dependence of Gold Nanoparticle Uptake into Mammalian Cells*. Nano Letters, 2006. **6**(4): p. 662-668.
76. Kim, J.A., et al., *Role of cell cycle on the cellular uptake and dilution of nanoparticles in a cell population*. Nat Nano, 2012. **7**(1): p. 62-68.
77. Ortec. *Preamplifiers*. Available from: www.ortec-online.com.
78. Bettoli, A.A., *Ionoluminescence (IL) with a nuclear microprobe*, in *School of Physics 1999*, University of Melbourne.
79. Bettoli, A.A., et al., *Ion beam induced luminescence from diamond and other crystals from a nuclear microbeam*. Nuclear Instruments and Methods in Physics Research Section B: Beam Interactions with Materials and Atoms, 1994. **85**(1-4): p. 775-779.
80. Bettoli, A.A., et al., *Imaging Ni segregation in synthetic diamond using ionoluminescence (IL) and particle induced X-ray emission (PIXE)*. Nuclear Instruments and Methods in Physics Research Section B: Beam Interactions with Materials and Atoms, 2001. **181**(1-4): p. 225-230.
81. Teo, E.J., et al., *Depth-resolved luminescence imaging of epitaxial lateral overgrown GaN using ionoluminescence*. Journal of Crystal Growth, 2004. **268**(3-4): p. 494-498.
82. Bettoli, A.A., K.W. Nugent, and D.N. Jamieson, *The characterisation of high-grade synthetic quartz, corundum and spinel using ionoluminescence (IL)*. Nuclear Instruments and Methods in Physics Research Section B: Beam Interactions with Materials and Atoms, 1997. **130**(1-4): p. 734-739.
83. Olympus. *Olympus Microscopy Resource Center*. Available from: <http://www.olympusmicro.com/primer/techniques/fluorescence/fluorescenceintro.html>.
84. Fisher, P.J., et al., *Enhanced biological cathodoluminescence*. Optics Communications, 2008. **281**(7): p. 1901-1908.
85. Niitsuma, J.-i., et al., *Cathodoluminescence investigation of organic materials*. Journal of Electron Microscopy, 2005. **54**(4): p. 325-330.
86. Niioka, H., et al., *Multicolor Cathodoluminescence Microscopy for Biological Imaging with Nanophosphors*. Appl. Phys. Express, 2011. **4**(11).
87. Barnett, W.A., M.L.H. Wise, and E.C. Jones, *Cathodoluminescence of biological molecules, macromolecules and cells*. Journal of Microscopy, 1975. **105**(3): p. 299-303.
88. Wolfgang Becker and A. Bergmann *Detectors for high speed photon counting*.

89. *Photomultiplier tubes*, in *Hamamatsu photonics* 1994.
90. Invitrogen. *DAPI Protocols*. 2012; Available from: <http://www.invitrogen.com/site/us/en/home/References/protocols/cell-and-tissue-analysis/dapi-protocol/dapi-nucleic-acid-stain.html>.
91. Niu, J., T. Zhu, and Z. Liu, *One-step seed-mediated growth of 30-150 nm quasispherical gold nanoparticles with 2-mercaptosuccinic acid as a new reducing agent*. Nanotechnology, 2007. **18**(32).

Appendices

Appendix A. Sample Preparation for cells internalized with 100nm AuNPs

Synthesis and characterization of 100 nm AuNPs

The conventional Frens method to synthesize large size noble metal nanocrystals generally produces gold nanoparticles with wide size distribution. Therefore, in this work, in order to obtain gold nanoparticles with better shape uniformity, gold seeds were first prepared by wet chemistry reduction, and the desired gold nanoparticles were then acquired by a seed-mediated growth approach.

10 nm gold seeds were prepared by reducing 0.01% of gold salt solution with 0.04% of citrate & 0.001% of tannic acid in total volume of 20 mL at 70 °C. When the reacting solution turned into clear crimson, the temperature was brought to 110 °C, boiled for 5 min, and then cooled slowly in air to room temperature. These seeds were used to prepare 100 nm gold nanoparticles in a seeding-growth method adapted from Niu et al[91] at room temperature. Briefly, a 50 mL reaction mixture containing 0.5 mM of HAuCl₄ and 98.4 µL of the as-synthesized 10 nm gold seeds was prepared in a conical flask so that the gold molar ratio in solution to that in 10 nm gold seeds was fixed at 1000:1. After five minutes of vigorous stirring, 1.9 mL of 10 mM MSA, pH 7 was added quickly (gold solution to MSA at molar ratio of 1:0.76). The reaction was allowed to proceed for 40 minutes under vigorous stirring. The solution turned gradually from faint yellow to reddish purple, indicating the formation of large-size gold nanoparticles. Subsequently, the product was filtered and stored at 4 °C until further use. TEM analysis showed that mean particle

diameters for the gold seeds and the gold nanoparticles were 10.03 ± 1.0 nm and 97.02 ± 5.1 nm respectively. Both displayed size distributions within 10% of their respective mean diameters.

Coating of AuNPs

100 nm AuNPs were passivated by incubation in fetal bovine serum (FBS) at 37 °C for 4 hours. Following removal of unbound FBS with phosphate buffered saline (PBS) washes, FBS-coated AuNPs were concentrated by low-speed centrifugation (200 xg) to discourage aggregation. Concentration of the coated AuNPs was determined by spectrophotometric measurement and calculated using a molar extinction coefficient of $1.08 \times 10^{11} \text{ M}^{-1}\text{cm}^{-1}$.

Cell sample preparation

HeLa cells were seeded on silicon nitride windows (100 nm thick) at a density of

6000 cells/cm² in Dulbecco's modified Eagle's medium (DMEM) supplemented with FBS (10%) and antibiotics penicillin (100 units/ml) and streptomycin (100 µg/ml). Following attachment, control cells were rinsed with PBS and incubated in supplemented DMEM. The NP cells were similarly incubated but also using FBS-coated 100 nm AuNPs (5 pM) for 24 hours. Both control and NP cells were washed three times with prewarmed PBS and fixed in gluteraldehyde (2.5 %) for 24 hours. Fixed cells were then dehydrated using an ethanol gradient before critical point drying.

Appendix B. Quantification procedures of NPs in a whole cell

Method 1: Quantification of number of nanoparticles from RBS spectra

Given a sample containing nanoparticles of element Au .

1. Collect an RBS spectrum of a region(s) without any nanoparticles
2. Collect another RBS spectrum of a region with one single whole cell with nanoparticles.
3. Compare the two RBS spectra to find out the backscattering signal (the channel range) on the spectrum from the element Au .
4. Fit the 2nd RBS (cell + nanoparticles) spectrum using SIMNRA to extract the incident charge Q over the entire region (whole map).
5. With the knowledge of Q and detector solid angle Ω , simulate using SIMNRA a theoretical back-scattering spectrum of a uniform film of element Au with a mean thickness t (t is calculated below).
6. Assuming that the nanoparticles are spherical with a diameter d , we calculate t by finding the average path length of an incident beam over the whole sphere volume. To do that, we assume that each nanoparticle now assumes a cylindrical shape of height t and diameter d , but with the volume unchanged. Hence,

$$\frac{4}{3}\pi\left(\frac{d}{2}\right)^3 = \pi\left(\frac{d}{2}\right)^2 t \quad \Rightarrow \quad t = \frac{2}{3}d$$

7. In our case, the AuNPs are 100nm in diameter, so the thickness t is about 67nm.
8. Input information of Q and thickness t into the simulated RBS spectrum of Au film, calculate the total integral A_0 under the backscattering signal of Au peak in the theoretical spectrum.
9. Check the RBS spectrum of single whole cell region to find out the channel region of Au signal, integrate the counts (A) from the backscattering signal of Au .

10. Calculate the ratio of A to A_0 , this can be considered the percentage of the mask area covered by Au nanoparticles over the entire region of the scan with one single cell.

Hence, $C = A/A_0$ So the area of $S_{Au} = C * \text{Scan area}$
AuNPs,

11. Finally, assume that each sphere takes up an area of $\pi(d/2)^2$ with respect to the incident beam, the number of nanoparticles N is given as: $N =$

$$\frac{S_{Au}}{\pi(\frac{d}{2})^2} = 4 \frac{S_{Au}}{\pi d^2}$$

Method 2: Quantification of number of NPs from FSTIM data:

Principle: FSTIM is capable of resolving single particle. With AuNPs size and pixel size known, single particles and clusters of particles can be analyzed in FSTIM image to determine the amount of scattered ions in each cluster spatially. The amount of scattered ions from single particle can be known based on those single resolvable AuNPs. Since FSTIM yield is only determined by number of atoms for specific element in a thin film, then we can determine the number of AuNPs in each cluster, therefore calculate total number of AuNPs

Procedures:

1. Import the raw FSTIM data into imageJ, since all the particles are apparently located outside nucleous, first select the following four areas: A, all cell region excluding nucleolus; B, all no cell covered SiN area; C, an area of blank SiN without AuNPs; D, several areas of blank cell region without AuNPs (non-nucleous area).

2. Each pixel records the scattered counts (Yield). By analyzing the mean counts in labelled area C and D, the average counts per pixel scattered by pure SiN and cell are obtained as Y_{SiN} and Y_{cell} .
3. By adjusting the threshold level and analyzing particles, all AuNPs can be extracted from area A and B. The threshold level and particle size level are determined on the basis of including all the resolved single particles. The mean counts for each cluster and all the cluster (or particle) size (S) can be measured in the extracted area A and B. The mean counts for a certain cluster are Y_{au-si} and $Y_{au-cell}$.
4. Then, the counts at each pixel scattered from Au on area A (Y_{au-A}) and B (Y_{au-B}) can be calculated as: $Y_{au-A} = Y_{au-cell} - Y_{cell}$; $Y_{au-B} = Y_{au-si} - Y_{si}$.
5. The total counts scattered from each cluster can be calculated as:

$$Y'_{au-A} = S \text{ (size of each cluster)} * Y_{au-A}; \quad Y'_{au-B} = S \text{ (size of each cluster)} * Y_{au-B};$$
6. First, sort all the clusters according to their spatial size. By assuming the smallest clusters are single particles, which can also be confirmed by SEM image, average total scattered counts from single particle can be calculated as:

$$Y'_{s-au-A} = ave \text{ (single particles on A)}; \quad Y'_{s-au-B} = ave \text{ (single particles on B)};$$
7. Calculate the no. of particles in each cluster:

$$N_{au-A} = Y'_{au-A} / Y'_{s-au-A}; \quad N_{au-B} = Y'_{au-B} / Y'_{s-au-B};$$
8. The total no. of AuNPs on cell region and SiN region:

$$N_A = sum(N_{au-A}); \quad N_B = sum(N_{au-B});$$